Organic Solar Cells: Degradation Processes and Approaches to Enhance Performance

By

Fadzai Fungura

A dissertation submitted to the graduate faculty in partial fulfillment of the requirements for the degree of

DOCTOR OF PHILOSOPHY

Major: Condensed Matter Physics

Program of Study Graduate Committee:

Ruth Shinar

Joseph Shinar

Rana Biswas

Thomas Koschny

Sanjeevi Sivasankar

Iowa State University

Ames, Iowa

2016

Table of Contents

Chapter 1: Introduction to Organic Solar Cells (OSCs)

1.1 History of OSCs

The beginning of the development of organic photovoltaics (OPV) was marked by the initial observation of photoconductivity in an organic compound, anthracene [1]. The first observation was by Pochettino in 1906 [2]. In the 1960s, it was discovered that many common dyes have semiconducting properties; such dyes were among the first organic compounds to demonstrate the photovoltaic (PV) effect [1]. In 1958 Kearns and Calvin fabricated solar cells out of magnesium phthalocyanines (MgPh), producing a photovoltage of 200 mV [3]. Polymer-based solar cells, investigated in the 1980s, showed initially low power conversion efficiencies (PCEs) on the order of ~0.1% [4-5]. The active layer was usually a single layer of either a dye or a polymer [4-5] until 1986 when Tang fabricated a donor-acceptor heterojunction (HJ) structure, which improved the device efficiency to ~ 1% [6]. HJ solar cells were intensively studied, including small molecule HJ solar cells [7] and the introduction of the first polymer:C_{60} bulk HJ (BHJ) photodetector in 1994 [8]. BHJ solar cells consist of a mixed donor/acceptor active layer with donor-rich and acceptor-rich domains on the order of 10 nm. Fullerenes have high electron affinity and electron mobility, favorable qualities for BHJ solar cells. The BHJ solar cells alleviated the limitations of low exciton diffusion lengths and charge separation found in polymer only and HJ solar cells. Following their introduction, extensive research has been conducted on polymer:fullerene BHJ solar cells. Significant enhancement in the PCE [9-21] up to ~11%, was achieved by e.g., using low bandgap polymers [9-18] and developing approaches aimed at controlling the morphology of the active layer utilizing thermal annealing [19], solvent annealing [20], mixed solvents [12-21], and additives [9-15]. Recently Heliatek has developed a 13.2% PCE multijunction OPV [22].

Since the sun is abundant and free, direct conversion of solar energy to electricity is very appealing. Hence, OSCs development continues due to their potential as a low cost, lightweight, flexible, clean and renewable energy source, despite some shortcomings, in particular, their long-term stability, whose understanding is an ongoing R&D effort.

1.2 Introduction to π conjugated materials

The organic molecules used as the active layer in OPVs are π-conjugated compounds. They have single and double, or single and triple bonds alternating throughout the molecule or polymer backbone. The main component in these organic π-conjugated compounds is carbon, and in its ground state it has the configuration $1s^2 2s^2 2p^2$. Carbon 2s and 2p orbitals hybridize to sp, sp^2 and sp^3 orbitals as in ethyne or acetylene (CHCH), ethene or ethylene (CH_2CH_2) and methane (CH_4), respectively, as shown in Fig. 1 [23].

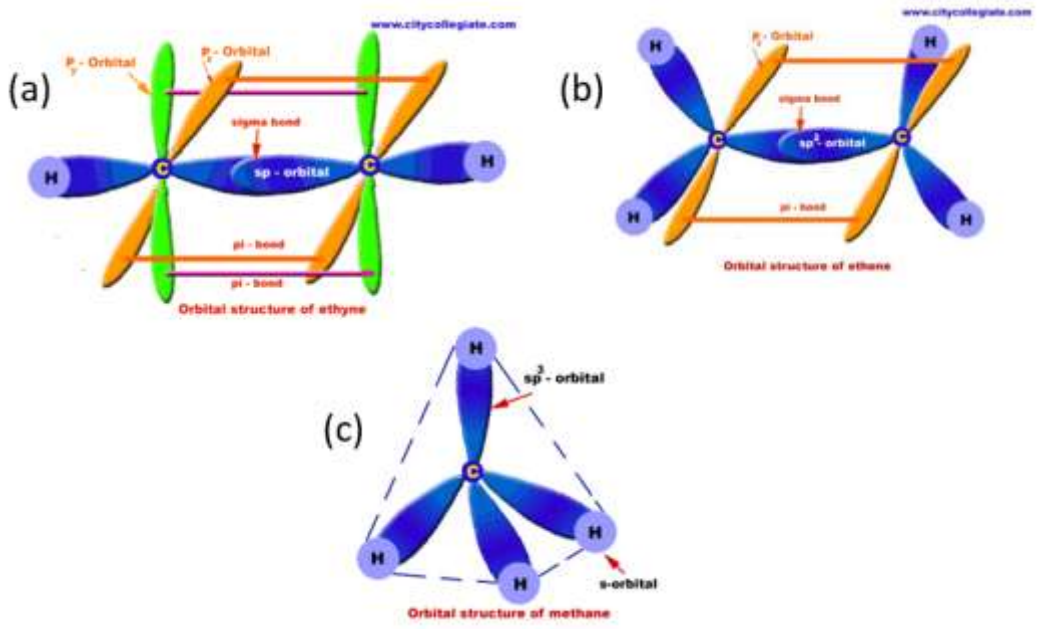

Fig. 1. *(a) sp hybridization in ethyne, (c) sp^2 hybridization in ethene and (c) sp^3 hybridization in methane.*

Looking at an ethyne molecule in detail (Fig. 1(a)), the carbon atoms are sp hybridized generating two sp orbitals 180º apart, and p_y and p_z orbitals perpendicular to the plane of the sp orbitals. For each carbon atom, one sp hybrid orbital overlaps with the neighboring one to produce one sigma (σ) bond and the remaining sp orbitals overlap with the 1s hydrogen atom orbitals to form a C-H σ bond. The p_y and p_z orbitals of the carbon atoms overlap to produce π bonds. In ethene, the carbon atoms are sp^2 hybridized and each carbon generates three sp^2 hybrid orbitals which are coplanar and 120º apart. For each carbon there is one remaining unhybridized p_z orbital, which is perpendicular to the plane of the sp^2 orbitals. The two p_z orbitals overlap to produce a π bond [23] as seen in Fig. 1(b). To form a sigma bond, for each carbon atom one sp^2 hybridized orbital overlaps with that of the second carbon atom. For methane, the carbon is sp^3 hybridized, producing four sp^3 hybrid orbitals 109.5º apart. Four σ bonds are produced from each of the carbon sp^3 hybrid orbital overlapping with 1s orbitals of the H-atoms [23]. π bonds allow delocalization of π electrons, which are responsible for the semiconducting properties of π-conjugated polymers and small molecules. As shown in Fig. 2, the combination of $2p_z$ orbitals results in formation of a two molecular orbitals, a bonding and an anti-bonding molecular π orbital [24]. Each energy level can only be occupied by two electrons according to the Pauli Exclusion Principle. Molecules containing more carbon atoms have more bonding and antibonding orbitals with different energies, and the energy levels broaden into quasi-continuous bands for carbon atoms going to infinity [24]. The highest occupied molecular orbital (HOMO) is the highest molecular orbital that contains electrons at 0K and the lowest unoccupied molecular orbital (LUMO) is the lowest molecular orbital containing no electrons at 0K.

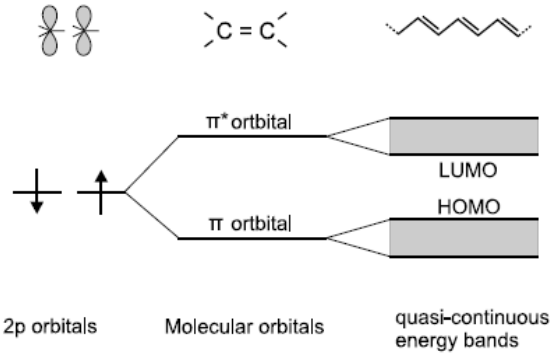

Fig. 2. *Schematic representation of molecular orbital splitting and formation of quasi continuous energy bands of occupied and unoccupied molecular orbital states [24].*

An excited state is formed by exciting an electron from the occupied molecular orbitals to the unoccupied molecular orbitals, which are analogous to the conduction and valence band, respectively, of a semiconductor. The least amount of energy needed to excite an electron is from the highest occupied molecular orbital (HOMO) to the lowest unoccupied molecular orbital (LUMO). The bandgap corresponds to the difference between the HOMO and LUMO, and it is the minimum photon energy in absorption and radiative emission optical transitions. The π conjugated materials used in OSCs should have strong absorption in the solar spectrum regime and materials whose absorption extends into the infrared region are preferred since ~ 52%-55% of solar radiation lies in the infrared region [25] as can be seen in Fig. 3 [25].

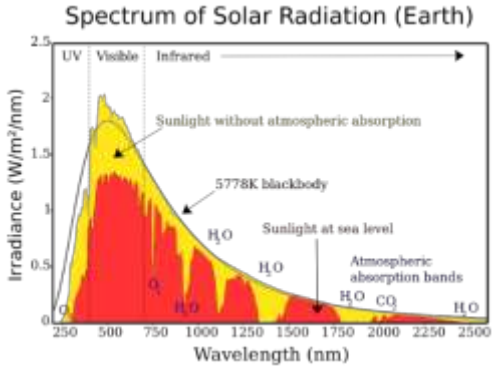

Fig. 3. *Solar irradiance spectrum above the atmosphere and at earth surface [25].*

Fig. 4 below shows examples of π conjugated polymers used in OSCs fabrication [26]; poly[N-9″-hepta-decanyl-2,7-carbazole-alt-5,5-(4′,7′-di-2-thienyl-2′,1′,3′-benzothiadiazole)] (PCDTBT), poly(4,4-dioctyldithieno(3,2-b:2',3'-d)silole)-2,6-diyl-alt-(2,1,3-benzothiadiazole)-4,7-diyl) (PSBTBT), poly[2,6-(4,4-bis-(2-ethylhexyl)-4H-cyclopenta[2,1-b;3,4-b′]-dithiophene)-alt-4,7-(2,1,3-benzothiadiazole)] (PCPDTBT), 2-methoxy-5-(2-ethylhexyloxy)-polyphenylenevinylene (MEH-PPV), poly(3-hexylthiophene) (P3HT), and poly((4,8-bis (octyloxy) benzo (1,2-b:4,5-b′) dithiophene-2,6-diyl) (2-((dodecyloxy) carbonyl) thieno(3,4-b) thiophenediyl)) (PTB1). [6,6]-phenyl-C-butyric acid methyl ester (PCBM) is a fullerene derivative that is commonly used as an acceptor in BHJ OSCs.

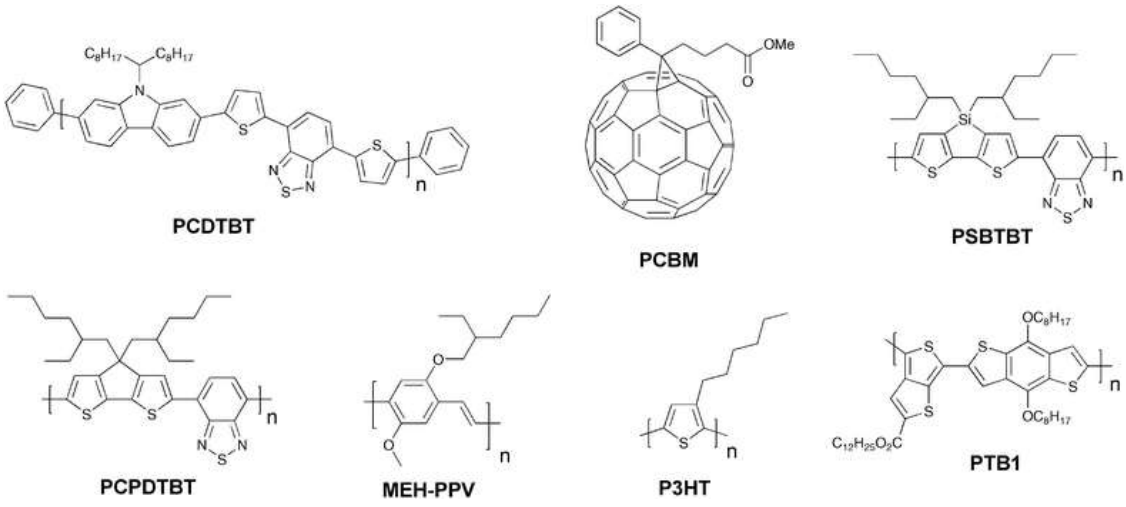

Fig. 4. *Examples of π conjugated polymers and PCBM, a fullerene derivative used in OSC fabrication. The polymers shown are: PCDTBT, PSBTBT), PCPDTBT, MEH-PPV, P3HT, and PTB1 [26].*

Significant work is ongoing to improve the electrical properties of π conjugated materials, such as higher hole and electron mobilities and close to ideal HOMO and LUMO levels for stronger solar spectrum absorption and consequently higher PCEs. Presently, fullerene derivatives such as $PC_{60}BM$ and $PC_{70}BM$ are the dominant acceptor materials used in BHJ solar cells due to their

very good electron transport properties and three-dimensional charge transport because of the spherical shape [27].

1.3 Structure and Working Principles of solar cells

1.3.1 OSCs structure and working principle

Fig. 5 shows different solar cell structures. Fig. 5(a) shows a single layer solar cell with an organic semiconductor between two electrodes. In converting solar energy into electricity, the first step is the absorption of light by the organic semiconductor, which results in the generation of bound electron-hole pairs called excitons. Typical organic semiconductors used in OSC fabrication have low dielectric constants ~ 3-4 [28], which results in high exciton binding energies $\geq$ 0.3 eV. Moreover, the exciton diffusion length is short ~ 10 nm. Thus, for a single layer OSC, exciton dissociation is very inefficient and low efficiencies typically less than 0.1% result [4,5,29]. To increase exciton dissociation, a planar heterojuction solar cell, shown in Fig. 5(b), can be used [6,29] with an acceptor material next to the donor material. When the donor absorbs light and an exciton is formed, it diffuses to the donor-acceptor (D-A) interface. The offset in energy at the D-A interface drives dissociation of excitons. Acceptors have a high electron affinity, thus when the exciton dissociates, the acceptor accepts the electrons and the holes remain on the donor as shown in Fig. 5(d). The electrons on the acceptor diffuse to the cathode and the holes diffuse to the anode where they are collected. Planar heterojunction solar cells have a higher efficiency than the single layer ones because of the increased dissociation of excitons and separation of holes and electrons, which reduces recombination. However, the small exciton diffusion length (~10nm) and small area of the D-A interface where exciton dissociation occurs, restricts the efficiency of the solar cells [29].

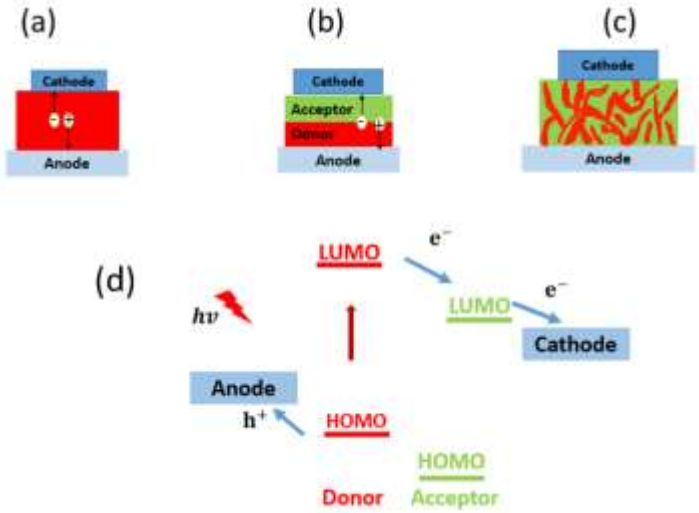

Fig. 5. *Schematic illustration of (a) single layered organic solar cell, (b) planar-heterojunction device (PHJ), (c) bulk heterojunction solar cell and (d) exciton dissociation at the donor–acceptor heterojunction.*

Following exciton formation in the donor of a BHJ solar cell, the exciton may relax (recombine) when it is unable to diffuse to the HJ interface and dissociate [30]. For excitons that make it to the HJ interface, geminate recombination may occur, which is the recombination of charge pairs shortly after exciton dissociation (within ~ 100 ns after dissociation) [28]. Geminate recombination involves a pair of charge carriers generated from the same exciton, which is a result of the difficulty to separate dissociated charges in organic materials [28]. Non-geminate (also referred to as bimolecular) recombination, which is the recombination of charge carriers dissociated from excitons generated by different absorption events, can also occur [28,30-32]. These limits are mitigated by mixing the donor and acceptor to make an active layer that has interpenetrating and bi-continuous networks of phase separated D-rich and A-rich domains, i.e., BHJ, as shown in Fig. 5(c). The BHJ structure provides a large interfacial area for charge separation and reduced exciton recombination due to the shorter distance that the electron

diffuses before reaching the D-A interface. Controlling the size of the D-rich and A-rich domains allows improvement of exciton dissociation, charge transport and charge collection efficiency. There are two main structures of BHJ solar cells: standard and inverted as shown in Fig. 6.

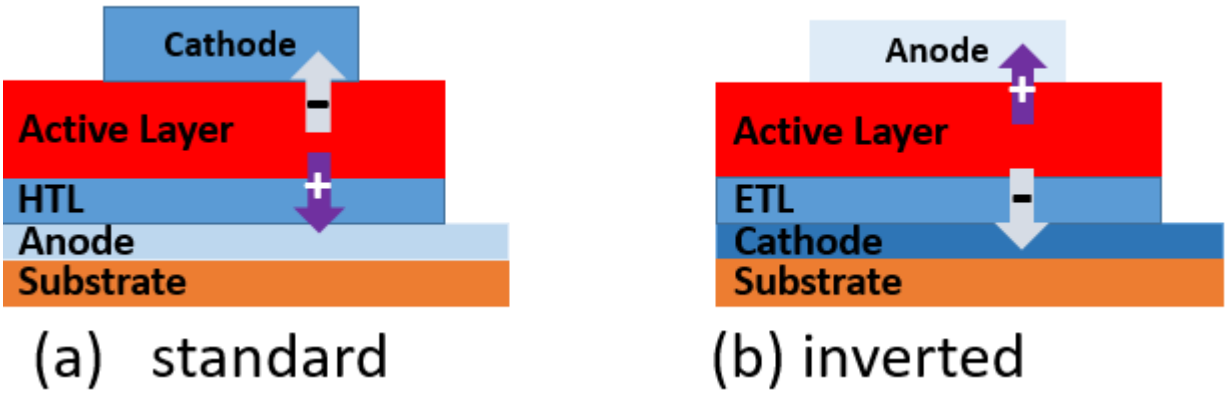

Fig. 6. *Comparison in direction of charge transport in (a) standard and (b) inverted solar cell structures.*

The standard structure of BHJ polymer solar cells typically consists of indium tin oxide (ITO) as the anode, PEDOT: PSS (poly(ethylenedioxythiophene) poly(styrene sulfonate)) on top as the hole transport layer followed by the polymer:fullerene blend, where the polymer is the donor and the fullerene is the acceptor, and calcium/aluminum as the cathode. When the polymer absorbs sunlight, excitons are generated. The polymer:fullerene mixture is made by dissolving both materials in a common solvent such as 1,2-dichlorobenzene (DCB) and spin-coating the mixture. Drying the active layer slowly results in small domains (~10 nm) of disordered mutually penetrating networks of the polymer-rich and fullerene-rich domains. When exposed to water and oxygen (as in ambient air), PSCs degrade rapidly due to oxidation of the polymer and fullerene, which may be accelerated in the presence of light, and results in a decrease in the

active layer conductance and reduced carrier mobility [33]. Furthermore, there is degradation of the PSCs that is attributed to PEDOT:PSS. PEDOT:PSS is hygroscopic and absorbs water from the ambient, which results in an increase in the sheet resistance of the solar cells [33]. One-way to avoid the use of PEDOT:PSS in order to increase the stability and efficiency of solar cells is by employing the inverted device structure. In inverted solar cells, the electric charges exit the device in an opposite direction compared to the standard device (Fig. 6(b)). As explained earlier, dissociated charges have to be collected by the electrodes to contribute to photocurrent. However, excitons near the organic/metal cathode interface in standard PSCs are quenched, and do not contribute to photocurrent [34]. To suppress exciton quenching, an electron-blocking layer (EBL) is introduced between the active layer and the metal contact. To block excitons, the material used should be a good electron transport layer (ETL) and have a high bandgap to prevent optical excitation. One such material is bathophenanthroline (BPhen) [34-36], which efficiently blocks excitons (and holes). BPhen has a high electron-mobility and long-term stability [37]. To further improve its transport properties BPhen can be n-doped by Cs_2CO_3, CsI, CsF, LiF or CsCl [38].

1.3.2 Solar Cell Parameters

Fig. 7 shows the equivalent circuit as well as the *J-V* characteristics of a solar cell [39]. I_L is the light generated current, the diode represents the bias dependent loss of current due to recombination, R_s is the series resistance, and R_{SH} is the shunt resistance [40].

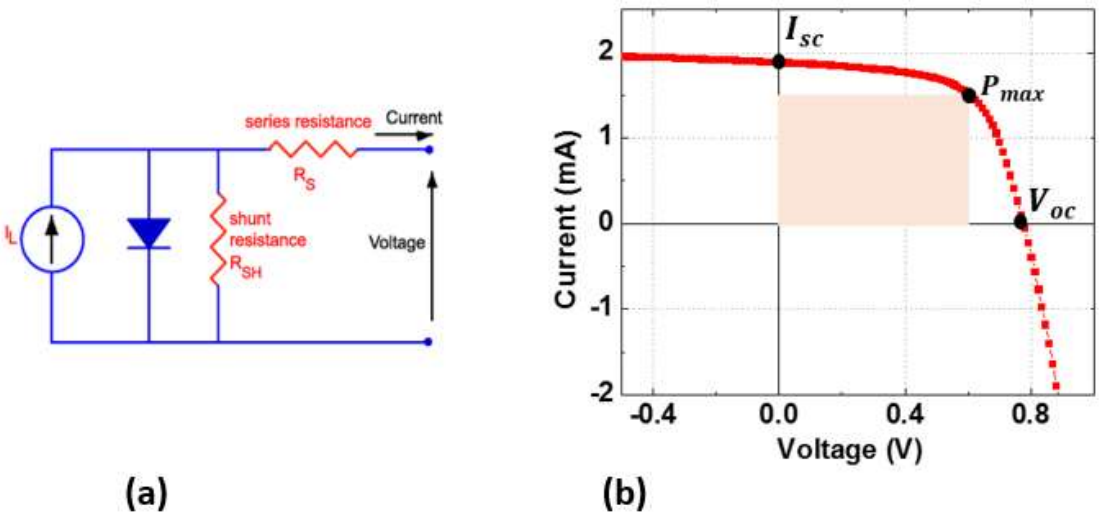

Fig. 7. *(a) Equivalent circuit [39] and (b) light I-V curve of a solar cell.*

In *I-V* measurements, voltage across a cell is varied over a desired range, and the corresponding collected current is given by

$$I = -I_L + I_0 exp\left[\frac{q(V+IR_S)}{nkT}\right] + \frac{V+IR_S}{R_{SH}} \qquad (1.1)$$

Where I_0 is the saturation current and n is the ideality factor (a number between 1 and 2).

Fig. 7(b) is the *I-V* curve of a solar cell. For an ideal solar cell, $R_s \sim 0$ and $R_{SH} \sim \infty$ and in the dark, $I_L = 0$, the dark *I-V* reflects the diode's characteristics (second term in Equation 1.1). In the presence of light, the curve shifts along the vertical y axis by an amount equal to the light generated current, $-I_L$. V_{oc}, the open circuit voltage, is the maximum voltage from an OSC, which occurs when the net current through it is zero. The short circuit current, I_{sc}, is the maximum current obtained when the voltage across the OSC is zero. At the point of maximum power, I_{mp} and V_{mp} are the corresponding voltage and current values. The fill factor (FF) is the ratio of the maximum power to the product of the V_{oc} and I_{sc}.

$$FF = \frac{I_{mp}V_{mp}}{I_{sc}V_{oc}} \qquad (1.2)$$

The power conversion efficiency (PCE) of a solar cell is given by,

$$PCE = \frac{V_{oc}I_{sc}FF}{P_{in}} \qquad (1.3)$$

Where P_{in} is the input power of the light incident on the solar cell. In this work P_{in} = 100 mW/cm^2 (~1X solar intensity).

The External Quantum Efficiency (EQE) of an OSC at a specific wavelength (λ) is the ratio of the number of collected charge carriers to the number of incident photons of a given wavelength:

$$EQE\ (\lambda) = \frac{\#\ of\ collected\ charge\ carriers\ (\lambda)}{\#\ of\ incident\ photons\ (\lambda)} \qquad (1.4)$$

The EQE provides a measure of how efficiently incident photons are converted to usable power output. Given the EQE and absorption spectra of a solar cell, the internal quantum efficiency (IQE) can be calculated. The IQE at a specific λ is the ratio of the number of collected charge carriers to the number of photons of a given λ absorbed by the OSC.

Several factors such as absorption, morphology, mobility, and recombination affect I_{sc}. The higher the absorption, the higher the I_{sc}. Generally absorption efficiency increases as the thickness of the active layer increases for thicknesses on the order of nanometers that are employed in OSCs. According to the Beer-Lambert Law

$$\eta = 1 - e^{-\alpha L} \qquad (1.5)$$

where η is the wavelength-dependent absorption efficiency, α is the absorption coefficient, and L is the optical path length [41]. The thicker the active layer the longer the optical path length and

the higher the absorption efficiency. However, there are challenges associated with the active layer's charge transport, such as dead ends in charge transport pathways and low hole mobilities in conjugated polymers [42], which lead to increased charge recombination and larger R_s as the thickness increases. Thus, optimization is necessary to reduce recombination and increase absorption of the active layer. Morphology control is very important for BHJ solar cells to get optimized interpenetrating networks of polymer and acceptor that enable exciton dissociation over a small diffusion length (~10 nm) and to optimize charge transport. Several approaches to optimize morphology have been utilized [9-20]. In P3HT, it has been shown that thermal annealing increases interchain interaction, increasing delocalization of π conjugated electrons, and thus lowering the bandgap [19]. This results in higher absorption and increased carrier mobility in the active layer, which enhances the performance of the solar cells. Solvent annealing was shown to increase the self-organization of polymers in BHJ structures, which leads to reduced R_s and increased FF, hence a higher PCE [20]. The use of additives has been shown to improve the miscibility of the polymer and the fullerene forming an active layer that has improved interpenetrating networks that enhance exciton dissociation and charge transport [16]. Low bandgap polymers improve the PCEs by absorbing more sunlight at longer wavelengths (infrared), which results in larger short circuit current densities (J_{sc}) [9-18] and V_{oc} by lowering the highest occupied molecular orbital (HOMO) of the polymer [10].

In OSCs, it has been reported that the V_{oc} is linearly related to the difference between the HOMO level of the donor and the LUMO level of the acceptor with an empirical formula:

$$V_{oc} = (1/q)(|E_{HOMO,donor}|-|E_{LUMO,acceptor}| - 0.3V) \qquad (1.6)$$

Where q is the elementary charge, $E_{HOMO,donor}$ is the HOMO level of the donor and $E_{LUMO,acceptor}$ is the LUMO level of the acceptor [43-46]. In general, V_{oc} stems from the splitting of electron and hole quasi-Fermi energy levels caused by illumination as shown in Fig.8 and given by:

$$V_{oc} = (\frac{1}{q})(E_{Fn} - E_{Fh}) \qquad (1.7)$$

Where E_{Fn} and E_{Fh} are the electron and hole quasi-Fermi levels in the acceptor and donor respectively.

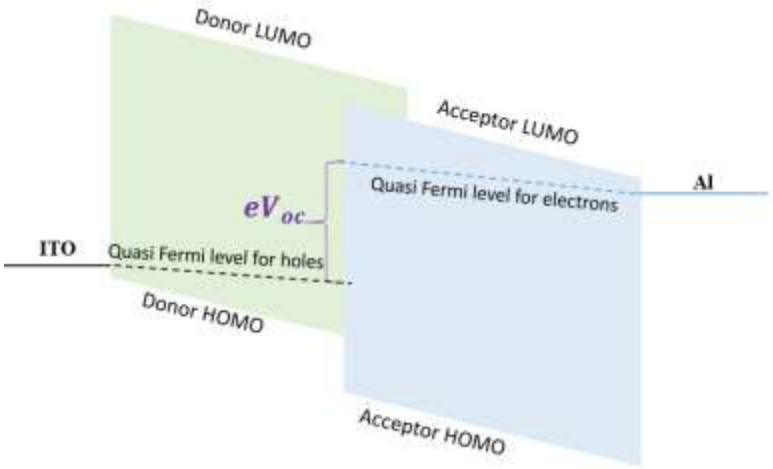

Fig. 8. *The difference in the quasi fermi levels of electrons in the acceptor and of holes in the donor gives the V_{oc}.*

As mentioned, the morphology, that is the packing of polymer domains, affects the bandgap of the polymer [19], which affects the V_{oc} of OSCs. Higher crystallinity and optimized packing of the polymer increases the V_{oc}. Saturation current density affects V_{oc} as given by equation 1.8

$$V_{oc} = \frac{nk_BT}{q}\ln(\frac{J_{ph}}{J_0} + 1) \qquad (1.8)$$

where k_B is the Boltzmann constant, T is the temperature, J_{ph} is the photo current density, and J_0 is the reverse saturation current density [44].

As seen from equation 1.8, the lower the reverse saturation current density, the higher the V_{oc}. For BHJ solar cells that utilize [6,6]-phenyl-C_{61}-butyric acid methyl ester ($PC_{61}BM$) (LUMO level of -4.2 eV) as the acceptor, and with an offset of at least 0.3 eV between the LUMO level of the donor and acceptor, a minimum polymer LUMO of -3.9 eV is required. A polymer with a deeper HOMO increases the V_{oc}, but the bandgap also increases, which decreases the amount of light absorbed. Since about 70% of the solar energy is in the 380 to 900 nm range, an ideal polymer that optimizes V_{oc} and J_{sc} would have a bandgap of ~1.4-1.5 eV [47],

with a HOMO level of -5.4 eV and LUMO level of -3.9 eV [47-48]. R_{SH} affects V_{oc}; when it is low, there are alternate low resistance paths for light-generated current, which lead to power losses and reduced V_{oc} [49].

The FF is mainly affected by charge mobility, collection, and resistances. A mismatch between hole and electron mobility can lead to charge accumulation either in the polymer or PCBM domain, which results in the lowering of the built-in electric field, reducing charge collection. Also charges trapped in the active layer lead to increased trap-assisted recombination leading to inefficient charge collection, reducing the FF. Optimized organic/electrode interfaces enhance charge collection and hence FF.

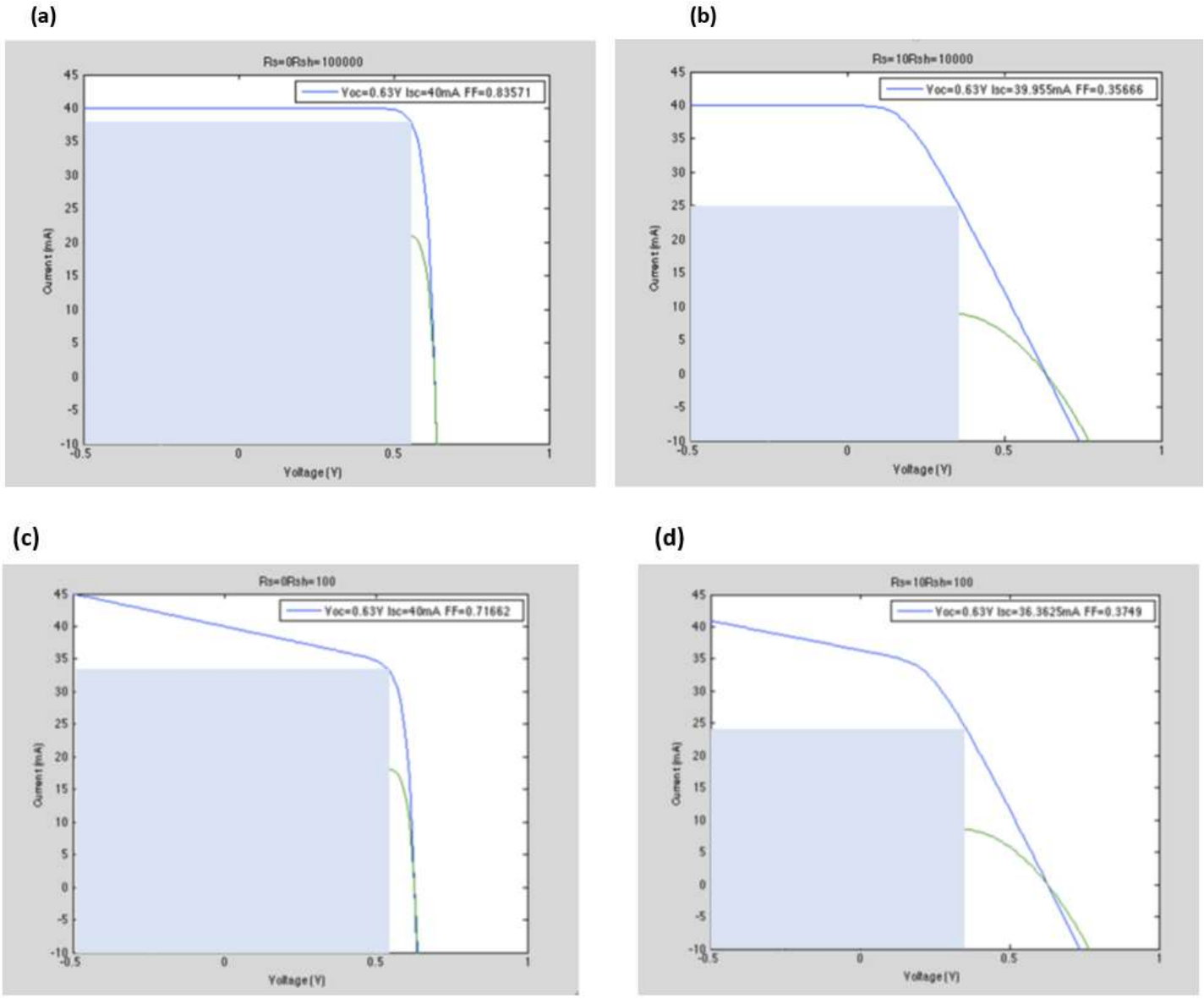

Fig. 9. *Effect of (a) 0Ω series and high shunt resistance and (b) high series resistance (c) low shunt resistance and (d) both high series and low shunt resistances on the FF a solar cell.*

Fig. 9 shows the effect of R_s and R_{SH} on the FF. The intersection of the squares and *I-V* curves show the maximum power point (P_{max}). According to equation 1.2, the ratio of P_{max} to the product of the V_{oc} and I_{sc} gives the *FF*. Increased series resistance and decreased shunt resistance reduce the FF. Optimizing the morphology and organic/electrode interface to reduce

resistance effects and improve charge transport and collection optimizes the FF for a given polymer:acceptor BHJ solar cell.

1.3.3 Additional approaches to enhance PCE

In addition to optimizing the processing conditions and morphology of OSCs for existing materials and utilizing novel device structures for PCE enhancement, significant efforts have been directed into developing new materials, particularly low bandgap polymers. An interesting class of low-bandgap polymers is a series composed of alternating benzo[1,2-b:4,5-b']dithiophene (BDT) and thieno[3,4-b]-thiophene (TT) units (denoted PBDTTTs) [9,11], which exhibit high PCEs (up to 9% for standard solar cells and 10% for inverted cells) for polymer:fullerene bulk heterojunction (BHJ) solar cells. These polymers have a high absorption in the long wavelength region up to ~ 740 nm and high charge carrier mobilities [50,51]. Research is ongoing to investigate the effects of different side chain groups, optimize their intermolecular interaction, molecular chain packing, and characterizing how they affect charge transport, V_{oc}, and J_{sc} for PCE enhancement [9]. Research for alternatives to fullerenes as electron acceptors is also ongoing. For example, polymer acceptors that lead to polymer/polymer BHJ solar cells may have a potential advantage since polymer acceptors can allow for fine tuning of morphological, electronic and optical properties and hence optimized performance of the solar cells [50]. The use of interlayers has been shown to enhance the PCE by improving charge collection [18,52-53]. For example, incorporating an alcohol/water-soluble conjugated polymer, poly [(9,9-bis(3′-(*N*,*N*-dimethylamino) propyl)-2,7-fluorene)-*alt*-2,7-(9,9–dioctylfluorene)] (PFN) as an interlayer between the active layer and the cathode leads to a simultaneous enhancement in J_{sc}, V_{oc} and FF in low bandgap thieno[3,4-b]thiophene/benzodithiophene (PTB7) solar cells [18]. The PFN interlayer was found to

enhance the built in field across the device and the electrical field at the interface between the active layer and cathode, resulting in both electron and hole charge transport and collection efficiency enhancement [18]. Also, PFN blocks holes from reaching the cathode reducing recombination [18].

Optical approaches have also been employed to enhance PCE. Optimized active layers for OSCs are very thin leading to high optical losses because of inadequate light trapping [54]. To further boost efficiency, approaches that enhance the optical path length by trapping light in the active layer are utilized. These approaches include using textured substrates [42], gold and silver nanoparticles in the hole transport layer (HTL) and/or active layer [55-58] and microlens on the light incident side of OSCs [41,59] as shown in Fig. 10.

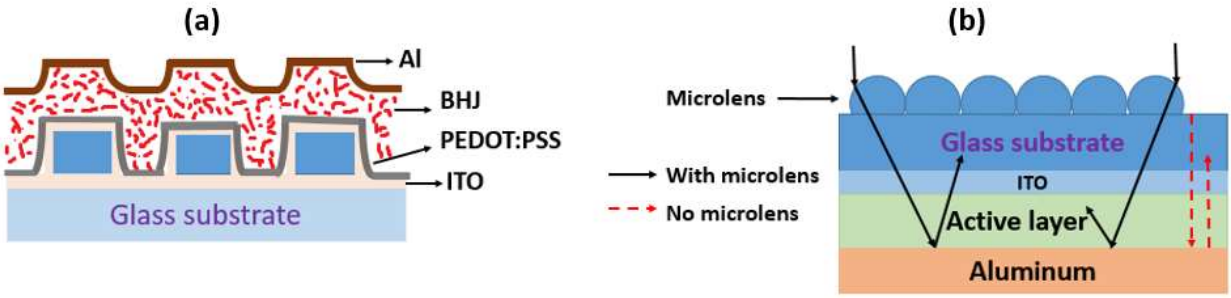

Fig. 10. *(a) Devices made on a textured substrate, (b) schematic illustration of light travelling in devices with microlens (solid black lines) and without microlens (dashed red line) in standard OSCs.*

Textured substrates with sub-micrometer feature heights and over 1 μm pitch have been shown to allow conformal spin-coating of the active layer [42]. K. S. Nalwa et al showed a 100% increase in light absorption near the band edge and a 20% increase in J_{sc}, which resulted in a 20% increase in the PCE, by employing textured substrates with a feature height of 300 nm and a pitch of 2 μm [42]. The absorption enhancement was due to trapping of light in the active layer.

Light that reaches the Al cathode in Fig. 10(a) is diffracted back into the active layer due to the periodic structure and the reflectance of the Al electrode. The diffracted light has a longer path length in the active layer and most of it undergoes total internal reflection at the ITO anode leading to trapping of light in the active layer. Use of microlens on the incident side has been shown to improve the PCE of OSCs [41,59]. Fig. 10(b) shows the schematic illustration of an OSC with a microlens array. Without a microlens array, light that is incident in the active layer perpendicular to the substrate and is reflected at the reflective electrode has a path length of $2t$, where t is the thickness of the active layer. Due to the curved surface of a microlens array, light incident will be at a non-normal angle and it will be refracted and enter the active layer at an angle θ to the normal resulting in a path length $2t/\cos(\theta)$, which is longer than $2t$. The microlens lead to reduced reflection due to the fact that light reflecting from one microlens can strike a neighboring microlens at an angle that allows it to be transmitted into the active layer [41]. The increase in absorption leads to higher J_{sc} and hence enhanced PCE. The main advantage of using microlens is that it does not affect active layer deposition techniques or environments since it is attached on the outer surface of the device and the efficiency enhancement is independent of the light incident angle [41].

1.4 Fabrication methods

OSCs are fabricated using solution processing and thermal evaporation. Solution processing involves casting, spin-coating, doctor blading, screen printing and ink-jet printing [60]. Spin-coating is mainly used in laboratories for fabricating polymer solar cells. The spin-coating process is shown in Fig. 11(a). The main disadvantage of the process is that it depends on many factors such as the solubility of the material and viscosity of the solution, as well as the drying rate, which depends on the solvent's volatility, and other parameters such as the temperature and

air flow that are not always easy to control, and hence affect reproducibility. The advantage is that for making solutions with a dopant, the constituent ratios are easy to control.

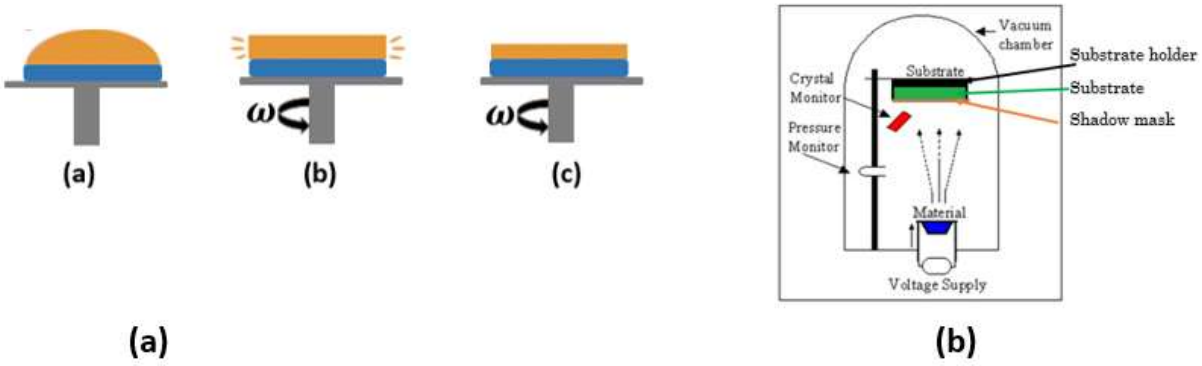

Fig. 11. *(a) Process of spin-coating (b) thermal evaporator system.*

Thermal evaporation as shown in Fig. 11 (b) is used mainly for fabricating small molecule solar cells, as well as for evaporating metals for contacts and metal oxides. Substrates are loaded into the chamber facing down and a patterned shadow mask is placed on the substrate. A voltage supply is connected to a source, on which a crucible with the material of interest is loaded. A high current passes through the source, heating it resistively. At a suitable temperature, the material in the crucible starts to evaporate, condensing on the substrate.

1.5 Application of OSCs

OSCs have many advantages over inorganic ones. OSCs are very thin (on the order of 500 nm for the whole device), and hence light-weight and can be fabricated on flexible substrates resulting in flexible devices that can be made transparent with the use of transparent electrodes. Resultantly, they can be used in numerous applications such as incorporation in flexible electronics, windows, roofs and walls [61]. They can be easily integrated with organic light emitting diodes (OLEDs) for analytical applications [62]. The absorption spectra can be tuned

and charge transport properties can be improved by synthesis of new materials. However, the major disadvantage of OSCs is their short operational lifetime. They degrade when exposed to air, moisture, and light.

1.6 Degradation of OSCs

Unencapsulated OSCs degrade in ambient air due to moisture and oxygen. Oxygen and water can diffuse into the device via pinholes in the top electrode [63] and via porous substrates; they can diffuse through all the OSC layers. Under illumination in air, UV light forms superoxides which aggressively attack the organic layers [33]. Different organic materials have different degrees of vulnerability to such degradation. Uptake of oxygen by the active layer causes it to expand, forming protrusions in the outer electrode further degrading the device [33]. Some polymers are susceptible to photo-oxidation leading to device degradation and other polymers such as P3HT form charge transfer complexes with oxygen [33]. In the presence of moisture and impurities, chemical/ electrochemical reactions take place at the ITO and Al electrodes corroding them and resulting in impurity diffusion into the active layer. Illumination of lights speeds up electrode corrosion [64]. This results in reduced charge collection efficiency and increased metal impurities in the active layer. For OSC structures that incorporate PEDOT:PSS as the HTL, due to the hygroscopic nature of PEDOT:PSS, water is absorbed, increasing the cell's R_s. Moreover, the PSS component has been shown to diffuse into the active layer where it probably reacts with the materials [33]. In the absence of oxygen and moisture, OSCs degrade under illumination. Recent theoretical calculations suggest that such photodegradation may be due to C-H [65-66], and/or C-O-C [67] bonds rearrangement/breaking, which result in a change of fundamental properties such as increase in midgap defects of the polymer, defects at the interface between the polymer and the fullerene, decreased hole mobility [63,64,68] and decreased charge collection

efficiency. Defects introduce recombination centers and sites where charge accumulate creating charged point sites. Traps enhance free carrier loss due to trap-assisted recombination [69]. Accumulated charge affects the electrostatic potential in the device, which can reduce the exciton diffusion length and hence exciton dissociation. It reduces also the carrier mobility and hinders charge transport. Each of these effects contributes to losses in J_{sc}, V_{oc}, FF and hence PCE [69].

References

[1] H. Spanggaard, F. C. Krebs, Sol. Energy Mater. Sol. Cells 83 (2004) 125.

[2] A. Pochettino, Acad. Lincei Rend. 15 (1906) 355.

[3] D. Kearns, M. J. Calvin, Chem. Phys. 29 (1958) 950.

[4] B. R. Weinberger, M. Akhtar, S. C. Gau, Synth. Met. 4 (1982) 187.

[5] S. Glenis, G. Tourillon, F. Garnier, Thin Solid Films. 139 (1986) 221.

[6] C. W. Tang, Appl. Phys. Lett. 48 (1986) 183.

[7] M. Hiramoto, H. Fukusumi, M. Yokoyama, Appl. Phys. Lett. 58 (1991) 1062.

[8] G. Yu, K. Pakbaz, A. J. Heeger, Appl. Phys. Lett. 64 (1994) 3422.

[9] Z. Shaoqing, Y. Long, Z. Wenchao, L. Delong, Y. Huifeng, H. Jianhui, Macromolecules 47 (2014) 4653.

[10] H.Y. Chen, J. Hou, S. Zhang, Y. Liang, G. Yang, Y. Yang, L. Yu, Y. Wu, G. Li, Nat. Photon. 3 (2009) 649.

[11] X. Fan, G. Fang, F. Cheng, P. Qin, H. Huang Y. Li, J. Phys. D: Appl. Phys. 46 (2013) 305106.

[12] D. Wang, F. Zhang, L. Li, J. Yu, J. Wang, Q. An, W. Tang, RSC Adv. 4 (2014) 48724.

[13] T.Y. Chu, J. Lu, S. Beaupré, Y. Zhang, J.R. Pouliot, S. Wakim, J. Zhou, M. Leclerc, Z. Li, J. Ding, Y. Tao, J. Am. Chem. Soc. 133 (2011) 4250.

[14] L. Dou, J. You, J. Yang, C.C. Chen, Y. He, S. Murase, T. Moriarty, K. Emery, G. Li, Y. Yang, Nat. Photon. 6 (2012) 180.

[15] J. Peet, J. Y. Kim, N. E. Coates, W. L. Ma, D. Moses, A. J. Heeger, G. C. Bazan, Nat. Mater. 6 (2007) 497.

[16] Y. Liang, Z. Xu, J. Xia, S.T. Tsai, Y. Wu, G. Li, C. Ray, L. Yu, Adv. Mater. 22 (2010) E135.

[17] Z. He, C. Zhong, S. Su, M. Xu, H. Wu, Y. Cao, Nat. Photon. 6 (2012) 591.

[18] Z. He, C. Zhong, X. Huang, W. Y. Wong, H. Wu, L. Chen, S. Su, Y. Cao, Adv. Mater. 23 (2011) 4636.

[19] G. Li, V. Shrotriya, Y. Yao, Y. Yang, J. Appl. Phys. 98 (2005) 043704.

[20] G. Li, V. Shrotriya, J. Huang, Y. Yao, T. Moriarty, K. Emery, Y. Yang, Nat. Mater. 4 (2005) 864.

[21] F. Zhang, K. G. Jespersen, C. Bjorstrom, M. Svensson, M. R. Andersson, V. Sundstrom, K. Magnusson, E. Moons, A. Yartsev, O. Inganas, Adv. Funct. Mater. 16 (2006) 667.

[22] http://www.pv-magazine.com/news/details/beitrag/heliatek-raises-bar-for-opv-efficiency-to-132_100023097/#axzz48it3ndw4

[23] http://www.citycollegiate.com/title_chemistryixl.htm

[24] S. Schols, *Device Architecture And Materials For Organic Light-Emitting Devices*, (Springer 2011).

[25] https://en.wikipedia.org/wiki/sunlight

[26] M. Helgesen, R. Søndergaard, F. C. Krebs, J. Mater. Chem. 20, (2010) 36.

[27] P. Hudhomme, EPJ Photovoltaics. 4 (2013) 40401.

[28] J. Nelson, MaterialsToday, 14 (2011) 462.

[29] A. F. Eftaiha, J-P Sun, I. G. Hill, G. C. Welch, J. Mater. Chem. A. 2 (2014) 1201.

[30] D. Credgington, F. C. Jamieson , B. Walker , T-Q. Nguyen , J. R. Durrant, Adv. Mater. 24 (2012) 2135.

[31] G. F. A. Dibb, F. C. Jamieson, A. Maurano, J. Nelson, J. R. Durrant, J. Phys. Chem. Lett. 4 (2013) 803.

[32] S. K. Pal, T. Kesti, M. Maiti, F. Zhang, O. Inganas, S. Hellstrom, M. R. Anderson, F. Oswald, F. Langa, T. Osterman, T. Pascher, A. Yartsev, V. Sundstrom, J. Am. Chem. Soc. 132 (2010) 12440.

[33] M. Jørgensen, K. Norrman, F.C. Krebs, Sol. Energy Mater. Sol. Cells 92 (2008) 686.

[34] P. Peumans, V. Bulovic, S.R. Forrest, Appl. Phys. Lett. 76 (2000) 2650.

[35] P. Peumans, S.R. Forrest, Appl. Phys. Lett. 79 (2001) 126.

[36] A. Opitz, J. Wagner, W. Brutting, I. Salzmann, N. Koch, J. Manara, J. Pflaum, A. Hinderhofer, F. Schreiber, IEEE J. Sel. Top. Quant. Electron. 16 (2010) 1707.

[37] S. Naka, H. Okada, H. Onnagawa, T. Tsutsui, Appl. Phys. Lett. 76 (2000) 197.

[38] Z. Xu, J. Yang, F. Sun, S.T. Lee, Y-Q. Li, J. Tang, Org. Electron. 13 (2012) 697.

[39] https://sharepoint.uvm.edu/sites/physx202/wiki%20pages/iv%20curves%20and%20how%20to%20make%20the%20fitting%20work.aspx

[40] PV Performance Modeling Collaborative (PVPMC), Sandia National Laboratories, Available at: https://pvpmc.sandia.gov/modeling-steps/2-dc-module-iv/diode-equivalent-circuit-models/

[41] J. D. Myers, W. Cao, V. Cassidy, S. H. Eom, R. Zhou, L. Yang, W. You, J. Xue, Energy Environ. Sci. 5 (2012) 6900.

[42] K. S. Nalwa, J-M. Park, K-M. Ho, S. Chaudhary, Adv. Mater. 23 (2011) 112.

[43] M. C. Scharber, D. Muhlbacher, M. Koppe, P. Denk, C. Waldauf, A. J. Heeger And C. J. Brabec, Adv. Mater., 18 (2006) 789.

[44] N. K. Elumalai, A. Uddin, Energy Environ. Sci. 9 (2016) 391.

[45] B. Qi, J. Wang, J. Mater. Chem. 22 (2012) 24315.

[46] M. C. Scharber, D. Muhlbacher, M. Koppe, P. Denk, C. Waldauf, A. J. Heeger, C. J. Brabec, Adv. Mater. 18 (2006) 789.

[47] H. Zhou, L. Yang, W. You, Macromolecules, 45 (2012) 607.

[48] T. Wang, A. J. Pearson, D. G. Lidzey, J. Mater. Chem. C 1 (2013) 7266.

[49] http://www.pveducation.org/pvcdrom/solar-cell-operation/shunt-resistance

[50] D. Mori, H. Benten, I. Okada, H. Ohkita, S. Ito, Energy Environ. Sci. **7** (2014) 2939.

[51] P. Adhikary, S. Venkatesan, N. Adhikari, P. P. Maharjan, O. Adebanjo, J. Chen, Q. Qiao Nanoscale 5 (2013) 10007.

[52] J. H. Seo, A. Gutacker, Y. Sun, H. Wu, F. Huang, Y. Cao, U. Scherf, A. J. Heeger, G. C. Bazan, J. Am. Chem. Soc., 133 (2011) 8416.

[53] Y. Zhao, Z. Xie , C. Qin, Y. Qu, Y. Geng, L. Wang, Sol. Energy Mater. Sol. Cells 93 (2009) 604.

[54] T. Kirchartz, K. Taretto, U. Rau, J. Phys. Chem. C 113 (2009) 17958.

[55] A. Ng, W. K. Yiu, Y. Foo, Q. Shen, A. Bejaoui, Y. Y. Zhao, H. C. Gokkaya, A. B. Djurisic, J. A. Zapien, W. K. Chan, C. Surya, ACS Appl. Mater. Interfaces 6 (2014) 20676.

[56] L. Lu, Z. Luo, T. Xu, L. Yu, Nano Lett. 13 (2013) 59.

[57] X. Xu, A. K. K. Kyaw, B. Peng, D. Zhao, T. K.S. Wonga, Q. Xiong, X. W. Sun, A. J. Heeger, Org. Electron. 14 (2013) 2360.

[58] H. Choi, J-P. Lee, S-J. Ko, J-W. Jung, H. Park, S. Yoo, O. Park, J-R. Jeong, S. Park, J. Y. Kim, Nano Lett. 13 (2013) 2204.

[59] Y. Chen, M. Elshobaki, Z. Ye, J-M. Park, M. A. Noack, K-M. Ho, S. Chaudhary, Phys. Chem. Chem. Phys. 15 (2013) 4297.

[60] F. C. Krebs, Sol. Energy Mater. Sol. Cells 93 (2009) 394.

[61] https://en.wikipedia.org/wiki/polymer_solar_cell

[62] E. Manna, F. Fungura, R. Biswas, J. Shinar, R. Shinar, Adv. Funct. Mater. 25 (2015) 1226.

[63] K. Norrman, N. B. Larsen, F.C. Krebs, Sol. Energy Mater. Sol. Cells 90 (2006) 2793.

[64] H. Aziz, G. Xu, Synthetic Metals 80 (1996) 7.

[65] R. A. Street, D. M. Davies, Appl. Phys. Lett. 102 (2013) 043305.

[66] R. A. Street, J. E. Northrup, B. S. Krusor, Phys. Rev. B 85 (2012) 205211.

[67] S. Shah, R. Biswas, J. Phys. Chem. C 119 (2015) 20265.

[68] J. Bhattacharya, R. W. Mayer, M. Samiee, V. L. Dalal, Appl. Phys. Lett. 100 (2012) 193501.

[69] J. A. Carr, S. Chaudhary, Energy Environ. Sci. 6 (2013) 3414.

Chapter 2: Experimental Setup and Characterization Techniques

2.1 Introduction

To characterize the performance of organic solar cells (OSCs), several measurements are performed, including current density-voltage (*J-V*) to analyze the short circuit current density (J_{sc}), the open circuit voltage (V_{oc}), the fill factor (*FF),* and the power conversion efficiency (PCE). External quantum efficiency (EQE) measurements provide information regarding the light absorption spectrum and charge collection. Subgap QE and density of states (DOS) measurements provide an analysis of midgap defects in the polymer and at or near the polymer:fullerene interface for bulk heterojunction (BHJ) solar cells. To analyze hole and electron mobility, space-charge limited current (SCLC) measurements are performed. Continuous wave (CW) dark and light-induced electron paramagnetic resonance (EPR) measurements in BHJ films enable analysis of defects at the atomic scale, charge generation, and trapping. Moreover, CW EPR allows the analysis of the role of the polymer, fullerene, and the donor/acceptor (D/A) interface in defect generation.

2.2 Light and Dark Current density Voltage (J-V) Measurements

The *J-V* curve exhibits the overall performance of a solar cell. For light *J-V* measurements, the device under test is irradiated with 1X sun intensity (100 $\mathrm{mW/cm^2}$) and the current is measured while sweeping the external voltage. An ELH bulb was used as the solar simulator in this work. The measurement setup, within and outside a N_2-filled glovebox, is shown in Fig. 2.1.

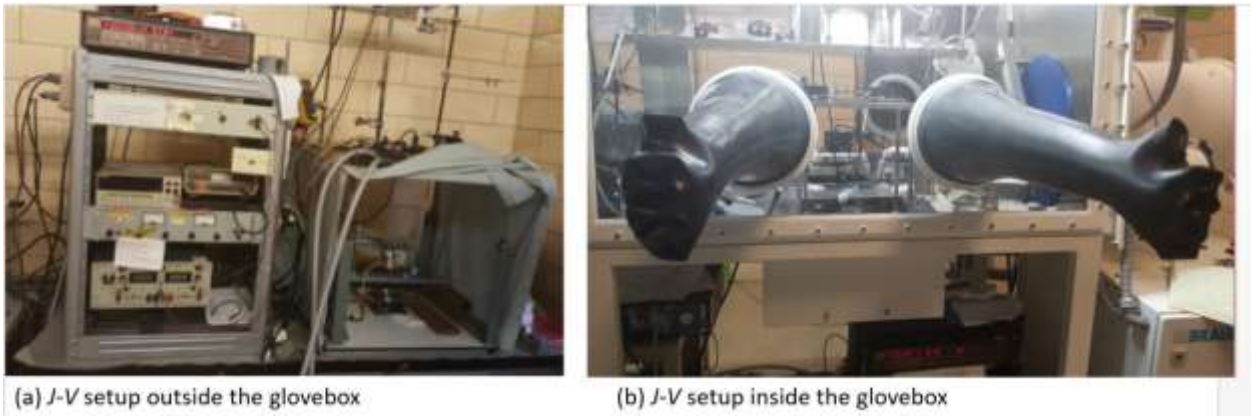

Fig. 2.1. *Setup for J-V measurements in (a) ambient atmosphere and (b) the glovebox.*

Both setups include a Keithely source meter for the *J-V* measurements and a power source for the ELH lamp, which was cooled by a fan. The light intensity was monitored with a calibrated Si photodiode. All OSCs studied in this work were bottom illuminated. For dark *J-V* measurements, the samples and probes were enclosed and the glovebox and room lights were turned off for measurements. Typical forward bias dark *J-V* curves are shown in Fig 2.2.

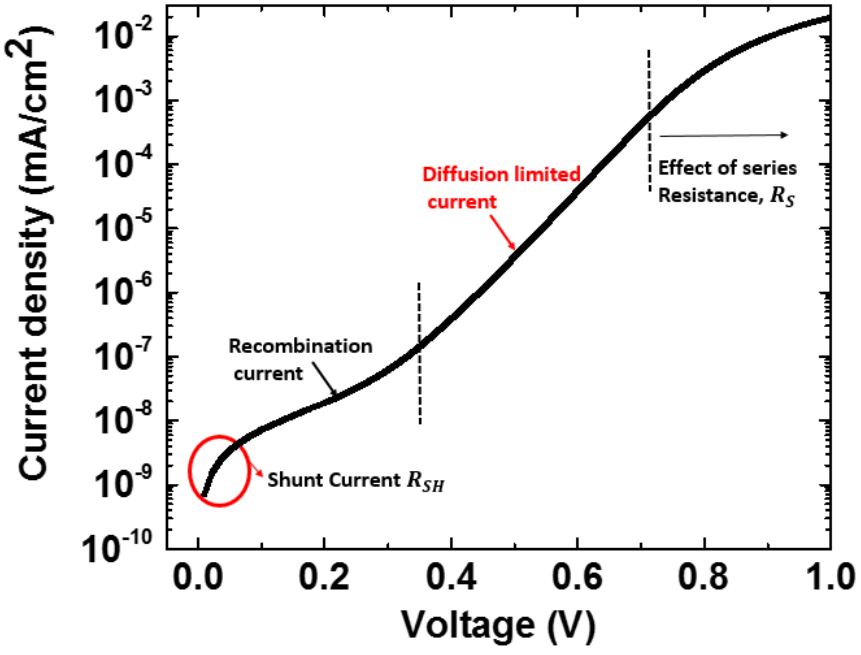

Fig 2.2. *Dark J-V characteristics of an OSC.*

The dark J-V relationship of an OSC follows the equation 2.1 [1]:

$$J = J_{01}\left[\exp\left(\frac{V-IR_S}{n_1 kT}\right)-1\right] + J_{02}[\exp\left(\frac{V-IR_S}{n_2 kT}\right)-1] + \frac{V+IR_S}{R_{SH}} \qquad (2.1)$$

Where J_{01} and J_{02} are saturation current densities, n_1 and n_2 are ideality factors, A is the pixel area, k is Boltzmann constant and T is the temperature in kelvin and V is the applied voltage. There are three main distinct regions of the dark *J-V* curve. For $V < 0.1$ V, R_{SH} is dominant. It is a result of pinholes and defects that create alternate current paths. The current in the exponential region $0.2 < V < 0.4$ is represented by the first part of equation (2.1). Ideally, $n_1 = 2$ and this region is dominated by generation-recombination current due to deep trap states at the donor-acceptor (D/A) interface in BHJ solar cells [2-4]. The region $0.4 < V < 0.6$ is the diffusion limited current region. Band to band recombination of electrons from the lowest unoccupied molecular orbital (LUMO) of the fullerene to the highest occupied molecular orbital (HOMO) of the polymer dominates and the ideal $n_2 = 1$ [2]. In the region $V > 0.8$ series resistance leads to the current saturation and deviation from exponential behavior and is represented by the last term in equation 2.1.

2.3 External Quantum Efficiency (EQE) Measurements

The EQE, which is the ratio of collected charge carriers to the number of incident photons gives a measure of how efficiently photons are harvested by the solar cell (SC). Fig. 2.3 shows the schematic of the QE measurement setup.

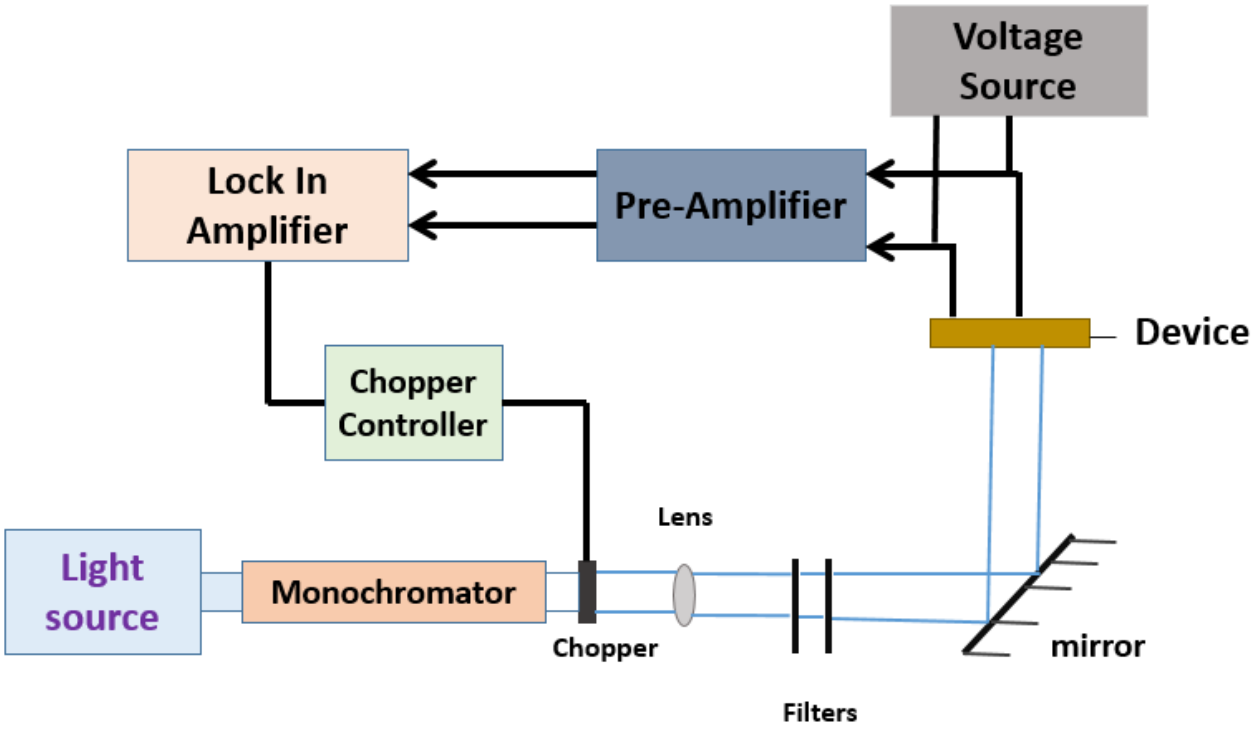

Fig. 2.3. *Schematic of the QE measurement setup.*

A beam of white light from a tungsten halogen lamp enters a monochromator exiting through a slit. The latter is translated to a 13 Hz alternating current (AC) by an optical chopper and then passes through a collimating lens and filters, which suppress noise from high order harmonics produced by the monochromator grating structure. A mirror redirects the beam to the device being tested. A pre-amplifier and lock-in amplifier collect the signal from the tested device. The pre-amplifier enhances the signal by ~6 orders of magnitude. The lock-in amplifier is synchronized with the chopper through a reference signal, which enables it to isolate the signal from the device from noise that may be caused by ambient light and electromagnetic interference. The reading from the lock-in amplifier gives the QE spectral response of the device. An external voltage source allows the measurement of EQE under DC bias to investigate issues of carrier collection at the electrodes. To calculate the absolute EQE of the OSC, a silicon

solar cell reference with a known device area and QE at corresponding wavelengths is used. The following equation is used to calculate the absolute EQE of the solar cell:

$$\text{Abs EQE}(\lambda) = \frac{Signal\ from\ sample\ (\lambda)}{Signal\ from\ reference\ (\lambda)} \times \frac{Area\ of\ reference\ cell}{Area\ of\ sample} \times \text{QE of reference}(\lambda) \qquad (2.2)$$

2.4 Subgap Quantum Efficiency

To investigate deep defects within the polymer and at the interface between the polymer and fullerene in BHJ organic solar cells (OSCs), subgap QE measurements are performed. Subgap QE provides very important information about the nature of traps within the bandgap and the corresponding energetic location. Fig. 2.4 shows the setup for subgap QE measurements.

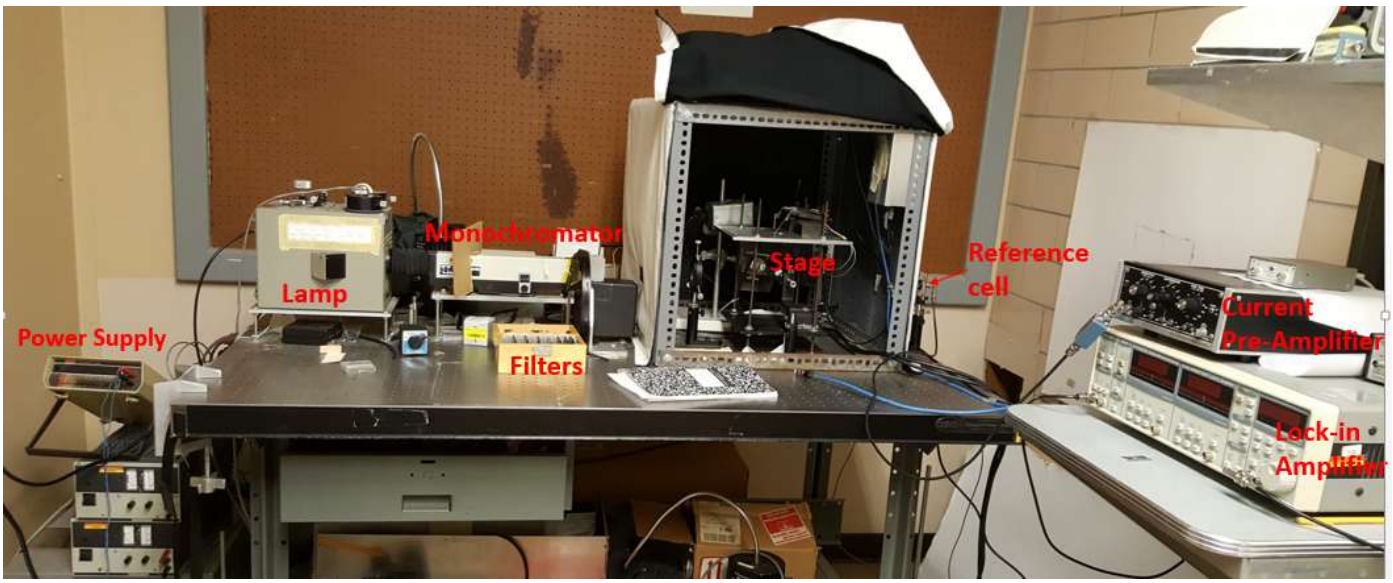

Fig. 2.4. *Schematic of the subgap QE measurement setup.*

A halogen tungsten lamp provides white light that passes through a manual monochromator, giving out narrow wavelengths of light. The monochromator outputs light energy as low as 0.8 eV. Mirrors below the stage redirect light onto the sample on the stage. Probes on the stage are

connected to the current preamplifier and lock-in amplifier. To calculate the absolute subgap QE of the OSC, silicon and germanium reference SCs with a known device area and QE at corresponding wavelengths were used. Equation 2.2 was used to calculate the absolute subgap QE.

2.5 Density of States (DOS)

Capacitance-Voltage (CV) measurements are used to estimate the flatband voltage (V_{FB}) and the width of the depletion layer within OSCs. The measurements are done at a fixed frequency of 1 kHz. These values, together with capacitance-frequency (CF) measurements, are used to calculate the DOS. The depletion width is given by [5]

$$w = \sqrt{\frac{2\varepsilon(V_{FB}-V)}{qN_A}} \qquad (2.3)$$

Where V_{FB} is the flat band voltage, V is the applied DC bias, N_A is the dopant density and ε is the permittivity of the material. The capacitance is given by:

$$C = \frac{\varepsilon A}{w} \qquad (2.4)$$

Where A is the pixel area. Combining equation 2.3 and 2.4 results in the following equation:

$$\left(\frac{A}{C}\right)^2 = \frac{2(V_{FB}-V)}{q\varepsilon N_A} \qquad (2.5)$$

Plotting $\left(\frac{A}{C}\right)^2$ vs V, the x-axis intercept gives V_{FB} and N_A can be derived from the slope of the line in forward bias. CF measurements are based on trapping and de-trapping of charges in

defect states inside the bandgap [6,7] and the emission speed depends on the energetic location of the traps. The rate of emission of electrons from states in the bandgap to the conduction band is given by

$$e_n = v_0 \exp\left(-\frac{E_C - E_T}{K_B T}\right) \qquad (2.6)$$

Where e_n is the emission rate, E_C is the conduction band, E_T is the energy level of a trap, K_B is the Boltzman constant, and T is temperature in Kelvin. v_0 is the attempt to escape frequency and some trap states (E_{T1}, E_{T2}, E_{T3}) are shown in Fig. 2.5.

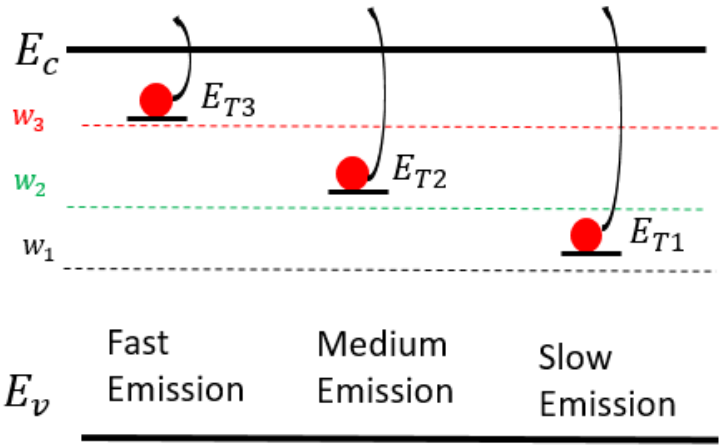

Fig. 2.5. *Trap response in CV measurements of electrons with* $w_3 > w_2 > w_1$.

w_1 represents the emission rates for deep traps, and for capacitance measured at frequencies lower than, w_1, all gap states, E_{T1}, E_{T2}, E_{T3} respond to the applied signal and contribute to capacitance. When the input frequency is increased (for instance to w_2), deeper traps (E_{T1}) do not respond since they have relatively lower emission rates and hence do not contribute to the measured capacitance resulting in lower capacitance values. Generally electron/hole traps closer to the conduction/valence band have high emission rates whereas those in the middle of the

bandgap have lower emission rates. If the frequency of perturbation is low enough that all trap states can re-emit trapped charges, the capacitance reflects the density of defect states (DOS) in the bandgap. The DOS is calculated by equation 2.7 which uses the derivative of the capacitance with respect to the frequency [6].

$$g(E_\omega) = -\frac{V_{FB}}{qwK_BT}\frac{dC(\omega)}{dln(\omega)} \qquad (2.7)$$

Where $g(E_\omega)$ is the density of states, C is the capacitance, ω is the angular frequency, V_{FB} is the flat-band voltage of the solar cell, w is the thickness of the depletion layer, K_B is the Boltzmann constant, T is the temperature in Kelvin, and E_ω is related to frequency by:

$$E_\omega = \frac{K_BT}{q} ln(\omega_0/\omega) \qquad (2.8)$$

where $\omega_0 = 2\pi v_0$ is the angular attempt to escape frequency and ω is the angular frequency of the input signal. DOS measurements were obtained by measuring the capacitance as a function of frequency (in the range 1 Hz to 200 kHz) $C(f)$ at 98 mV and as a function of voltage $C(V)$ at 1 kHz using a HIOKI LCR meter at room temperature in the dark.

2.6 Space Charge limited current (SCLC)

The SCLC method is one of the easy ways to measure mobility in semiconductors. The semiconductor whose charge mobility is to be measured should be sandwiched between two electrodes, at least one of which should form an ohmic contact [8]. Indium tin oxide (ITO), Aluminum (Al), and gold (Au) are commonly used as metal contacts in making OSCs and poly(3,4-ethylenedioxythiophene) (PEDOT:PSS) is a commonly used hole transport polymer. With the proper choice of electrodes, hole or electron mobilities can be measured. For instance, to measure hole and electron mobilities, the structures ITO/PEDOT:PSS/Polymer/Au (for

polymers such as P3HT (poly(3-hexylthiophene) [8] and PBDTTT-EF-T [9]) and Al/Acceptor/ (Cesium Carbonate)Cs_2CO_3/Al (for acceptors such as [6,6]-phenyl-C-butyric acid methyl ester (PCBM)), respectively, are used**.** Mobility measurements were performed in the glovebox with the sample connected to a Keithley source. During each measurement, the sample was kept in the dark and the current (using the current source) and corresponding voltage were recorded. In the low voltage region, the current increases linearly and traps are not filled by the injected charge. In the high applied voltage region, all traps get filled by the injected charges that move freely with a current density (*J*) to voltage (V) relationship given by [8]:

$$J = \frac{9}{8}\varepsilon_0\varepsilon_r\mu\frac{V^2}{t^3} \qquad (2.9)$$

Where ε_0 is the vacuum permittivity, ε_r is the dielectric constant of the film, *t* is the thickness of the active layer, μ is the mobility, *J* is the applied current density, and *V* is the measured voltage . From Eq. 2.9, the mobility can be calculated from the slope of a *J* vs V^2 plot [8].

2.7 Absorption

To measure absorption of thin films, transmittance measurements were obtained using a CARY 5000 spectrophotometer and reflection measurements were obtained using a HR4000 spectrometer. The relationship between % transmittance (T), % reflection (R), and % absorption (A) is A+T+R=100% so, A=100%-T-R. Fig. 2.6 shows a simplified schematic of the transmittance measurement by the carry [10]. The diffraction grating disperses light and the aperture selects a single wavelength based on the angle of incidence. The detector measures the amount of transmitted light.

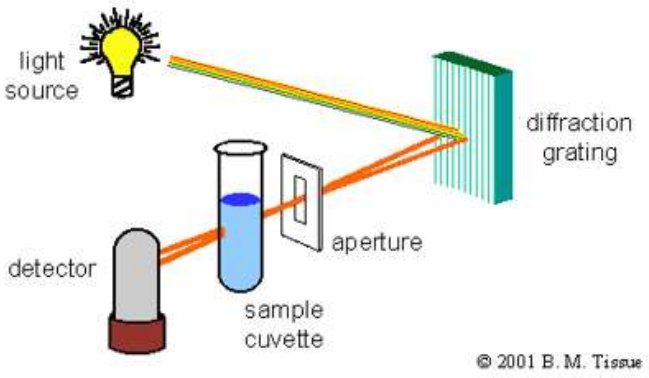

Fig. 2.6. *Simplified schematic of the transmittance measurement by the carry.*

2.8 Electron Paramagnetic Resonance (EPR)

The continuous wave (CW) EPR) spectrometer (Fig. 2.7) consists of a resonator that is designed to resonate at a specific microwave frequency, in our case at 9.8 GHz.

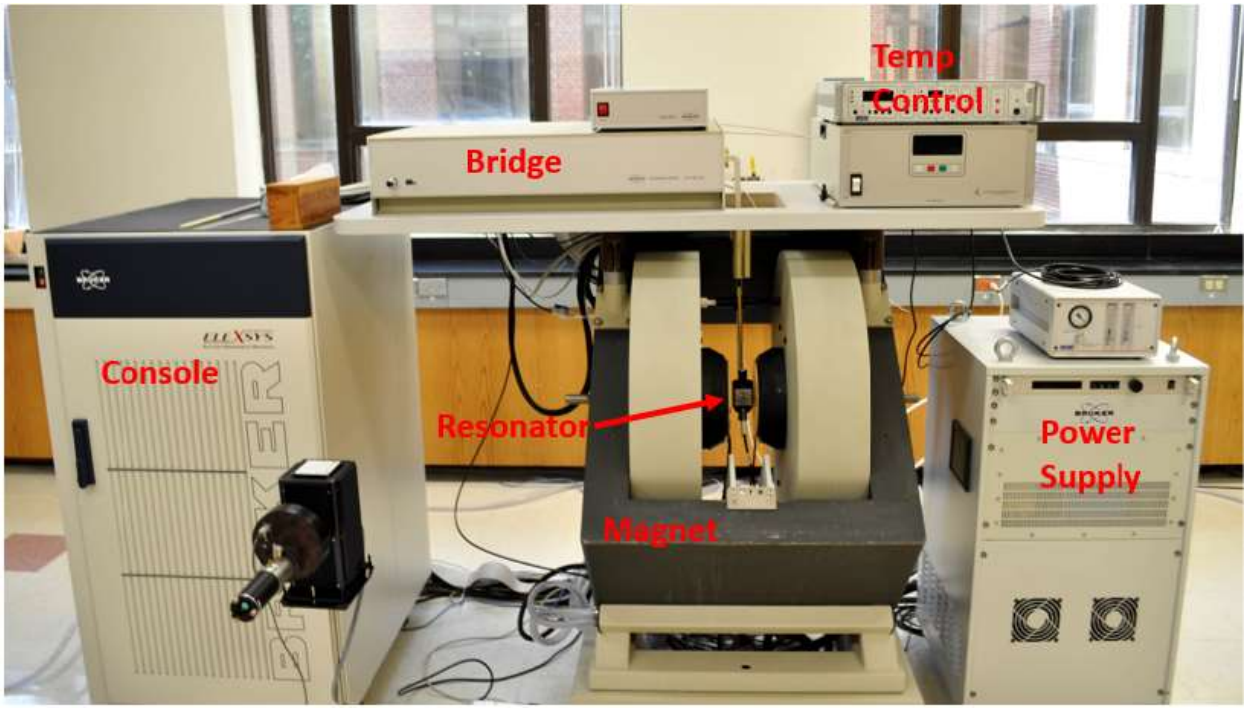

Fig 2.7. *Setup of an EPR spectrometer.*

A sample to be measured is placed in the resonator that is located between two electromagnets that vary the magnetic field depending on the amount of current running through them. As the strength of the magnetic field is varied, the resonance is detected by a decrease of the microwave energy reflected out of the resonator. Such energy change is due to the interaction of the magnetic field and unpaired charges in a sample as shown in Fig. 2.8.

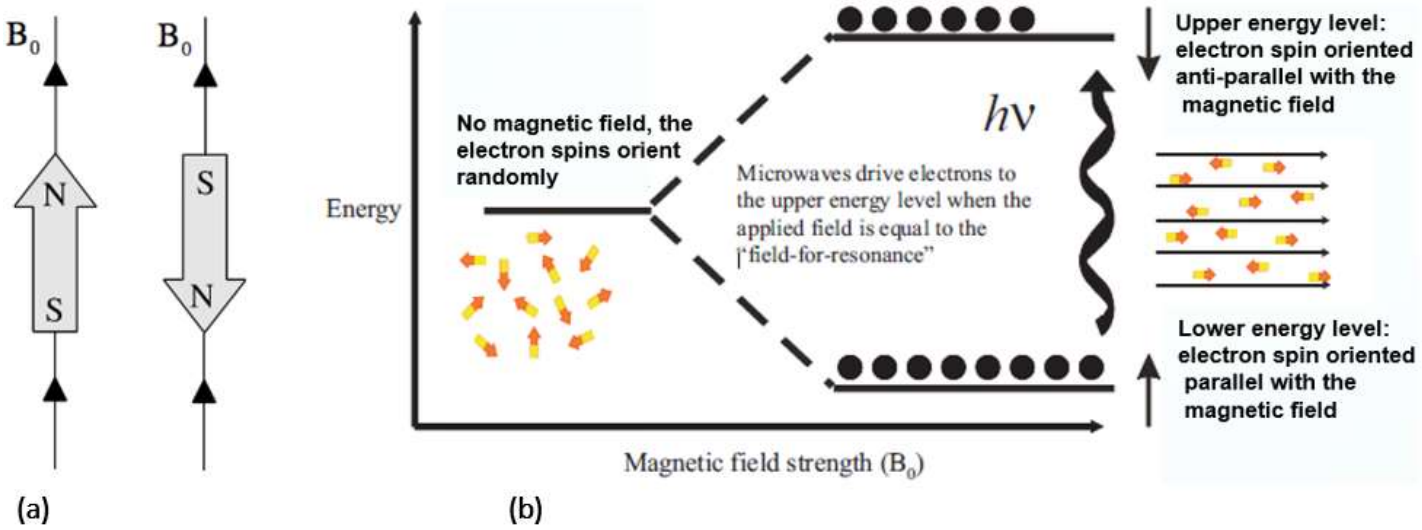

Fig 2.8. *(a) Minimum and maximum energy states of the electron spin with respect to the applied magnetic field (B_0) [11]. (b) Splitting of electron spins into two distinct energy states at the field of resonance [12].*

The energy differences studied in EPR spectroscopy are due to the Zeeman Effect. An electron has a magnetic moment and it acts like a bar magnet when placed in a magnetic field B_0. Its lowest energy state is when the moment of the electron, μ, is aligned with the magnetic field and the highest energy state is when the moment of the electron is aligned against the magnetic field as shown in Fig. 2.8 (a). The parallel and antiparallel states are designated as M_s = - ½ and M_s = + ½ respectively. The energy states are given by [13]:

$$E = g\mu_B B_0 M_s = \pm\frac{1}{2} g \mu_B B_0 \quad (2.10)$$

$$\Delta E = h\nu = g\,\mu_B B_0 \quad (2.11)$$

where g is the g-factor, a proportionality constant ≈ 2 for organics, but its exact value varies based on the electronic configuration of the particular radical. μ_B is the Bohr magneton, a natural unit of the electronic magnetic moment [14]. The g-factor, $g = \frac{h\,\nu}{\mu_B B_0}$ is independent of the microwave frequency and it can uniquely identify some compounds. Resonance occurs at the field strength that corresponds to the energy splitting of the spin states of an unpaired charge, as shown in Fig. 2.8(b). Every spectrum peak represents transitions between the spin states of unpaired charges.

Looking at the instrumentation in deeper detail, Fig. 2.9 shows the function of each part of the system.

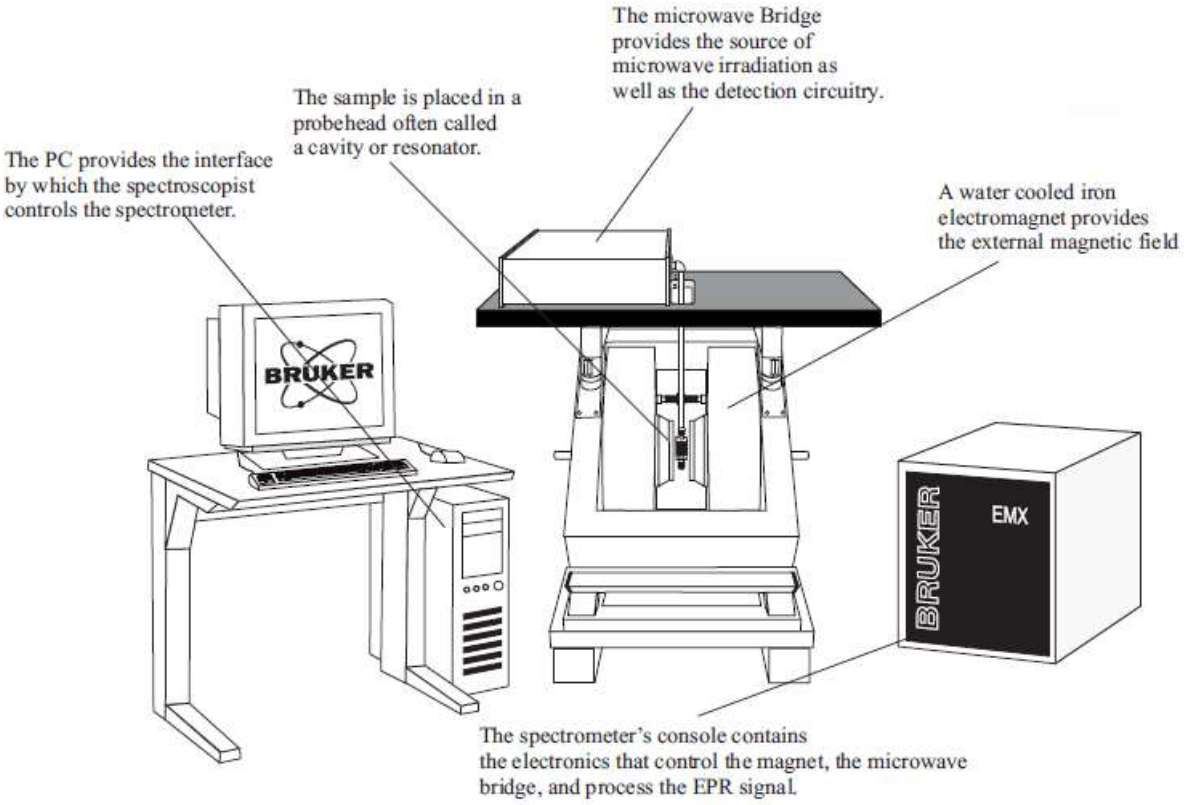

Fig 2.9. *Diagram of a typical CW EPR spectrometer [12].*

The microwave bridge contains the microwave irradiation source and the detector. The sample is placed in a resonator, which is a microwave cavity that amplifies the sample's weak signals. The console contains the electronics for signal processing, controlling the magnet, microwave bridge and computer. The computer is used to coordinate all the units for acquiring a spectrum and analyzing the data.

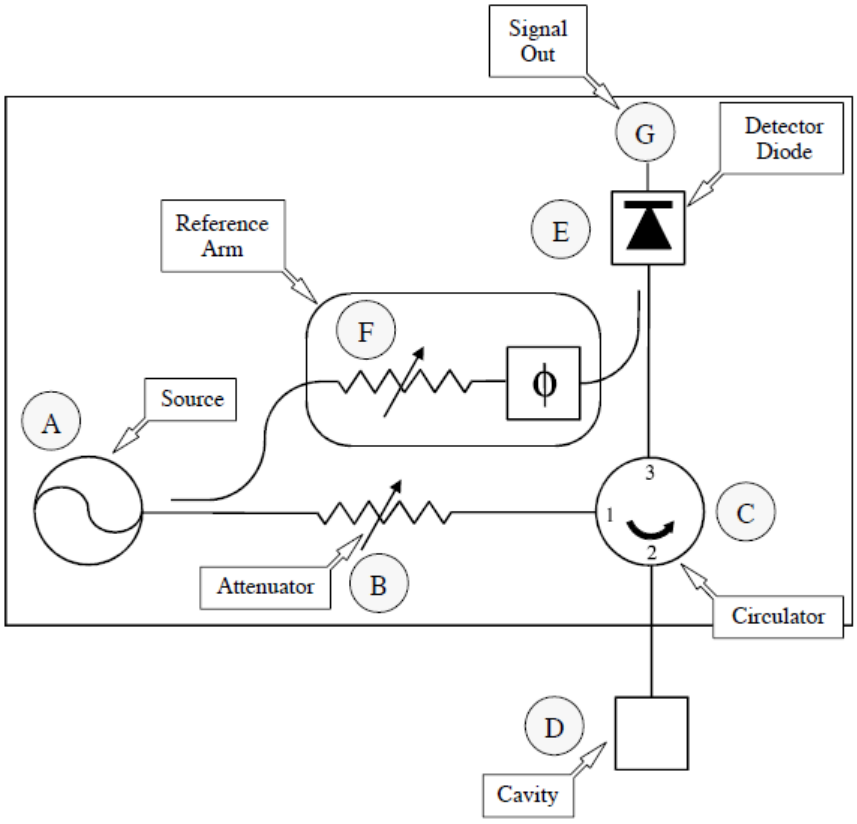

Fig 2.10. *Block diagram of a microvave bridge [11].*

Fig. 2.10 shows the block diagram of a microwave bridge; point A is the microwave source whose output power cannot be easily varied. Point B is the variable attenuator, which which blocks some of the microwave radiation allowing a precise and accurate control of the flow of microwave radiation. Point C is the circulator. Microwaves getting into the circulator via port 1 exclusively go to the cavity (Point D) via port 2. Reflected microwaves from the cavity are

directed to the detector through port 3. A diode (point E) detects the reflected microwaves and converts the microwave power to an electrical current. For optimal sensitivity, the diode should operate at high power levels (greater than 1 mW) where diode current has a linear relationship with square root of the microwave power. The reference arm (point F) insures that the detector is in that range by supplying some extra microwave power (bias) and there is a phase shifter to make sure that the bias microwave power is in phase with the reflected signal [11]. The microwave cavity is a rectangular or cylindrical shaped metal box, which resonates with microwaves and amplifies weak signals from the sample. At resonance, energy is stored in the in the cavity and no microwaves are reflected back. EPR has been used for microscopic characterizing of charge accumulation sites in polymer [15] and small molecule [16] solar cells. The advantage of this method is the ability to directly observe accumulated charge carriers [15].

References

[1] O. Breitenstein, J. Bauer, P. P. Altermatt, K. Ramspeck, *Solid State Phenomena* Vols. 156-158 (2010) 1.

[2] S. A. Hawks, G. Li, Y. Yang, R. A. Street, J. Appl. Phys. 116 (2014) 074503.

[3] R. A. Street, A. Krakaris, S. R. Cowan, Adv. Funct. Mater. 22 (2012) 4608.

[4] R. A. Street, J. E. Northrup, B. S. Krusor, Phys. Rev. B 85 (2012) 205211.

[5] B. G. Streetman, S. K. Banerjee, '*Solid State Electronic Devices*' Sixth Edition, Prentice Hall, (2013) page3 213-215.

[6] P. P. Boix, G. Garcia-Belmonte, U. Munecas, M. Neophytou, C. Waldauf, R. Pacios, Appl. Phys. Lett. 95 (2009) 233302.

[7]K. S. Nalwa, R. C. Mahadevapuram, S. Chaudhary, Applied Physics Letters, 98, 093306, 2011.

[8]T. Endale, E. Sovernigo, A. Radivo, S. D. Zilio, A. Pozzato, T. Yohannes, L. Vaccari, M. Tormen, Sol. Energy Mater. Sol. Cells 123 (2014) 150.

[9] D. Mori, H. Benten, I. Okada, H. Ohkita, S. Ito, Energy Environ. Sci. 7 (2014) 2939.

[10] B. M. Tissue, http://www.tissuegroup.chem.vt.edu/chem-ed/spec/uv-vis/singlebeam.html

[11] EMX User's Manual. Basic EPR Practice

[12] Bruker Biospin www.bruker-biospin.com

[13] W. A. John, J.R. Bolton, J. E. Wertz, *Electron Paramagnetic Resonance, Elementary Theory and Practical Applications:* Wiley-Interscience, New York, (1994).

[14] C. P. Jr. Poole, Electron Spin Resonance: A Comprehensive Treatise on Experimental Techniques, (John Wiley & Sons Inc., New York, 1983).

[15] T. Nagamori, K. Marumoto, Adv. Mater. 25 (2013) 2362.

[16] K. Marumoto, T. Fujimori, M. Ito, T. Mori, Adv. Energy Mater. 2 (2012) 591.

Chapter 3: Improved Efficiency and Stability of Inverted Polymer Solar Cells with a Solution-Processed BPhen Interlayer and Polystyrene Beads

A paper published in *Organic Electronics*

By **Fadzai Fungura**[#], Teng Xiao[#], James W. Anderegg, Min Cai, Joseph Shinar, and Ruth Shinar

# These authors contributed equally to the work.

Abstract

We demonstrate improved power conversion efficiency (PCE) and strongly enhanced stability of inverted organic solar cells (OSCs) with Cs halides by solution casting BPhen (4,7-di(phenyl)-1,10-phenanthroline) on the halide layer and ~100 nm polystyrene beads (PSB) on the blank side of the OSC. The PCE of ITO/CsCl/P3HT:PCBM/MoO_3/Al (where P3HT is poly 3-hexylthiophene and PCBM is [6,6]-phenyl-C_{60}-butyric acid methyl ester) improves by up to 46%, from 2.5% to ~3.7%, by adding a solution-processed BPhen layer between the CsCl and the active layer. For such cells with CsI (PCE ~ 3.3% - 3.4%) the increase was only 6% - 9%, to 3.5% - 3.7%. The PCE of cells devoid of the halides but with BPhen was ~3.3%. The cells were optimized by varying the BPhen concentration in a chlorobenzene solution. The results are consistent with reduced charge recombination at the ITO interface in the presence of the hole blocking BPhen interlayer. The use of hole blocking BCP (2,9-dimethyl-4,7-diphenyl-1,10-phenanthroline), as a substitute for BPhen, also showed an enhancement (though lower due to its lower electron mobility), verifying the effect of these materials as hole blocking interlayers. Interestingly, the stability of such non-encapsulated devices with CsCl/BPhen or CsI/BPhen improved significantly. For example, the PCE of unencapsulated cells with CsCl/BPhen kept in the dark under ambient conditions dropped by less than 2% after more than 3 weeks; the PCE of similar cells devoid of the BPhen layer dropped by ~60% during the same period. The PCE of

the cell with CsCl/BPhen dropped by ~16% after two months. High humidity, as expected, resulted in faster deterioration in cell performance. The PCE, however, was restored to within ~10% of the original value for two week old cells by solution-application of a PSB layer on the blank side of the cell's glass substrate. These beads direct and scatter the light to enhance absorption in the active layer. The results demonstrate that a simple approach such as casting a film of ~100 nm diameter PSB from an aqueous suspension on the blank side of the OSC substrate can improve long-term performance, and that spin coating BPhen is a low-cost and easy approach to reduce charge recombination at the cathode in inverted structures for increased PCE and stability.

3.1 Introduction

Organic solar cells (OSCs) have attracted extensive attention due to their potential as a flexible, lightweight, and low-cost renewable energy source. Significant achievements have been made in improving the devices' power conversion efficiency (PCE) [1-5], and considerable efforts are continuing in an attempt to understand degradation mechanisms and increase OSCs' lifetimes [6-11]. Recently, the application of exciton blocking layers (EBLs) in mostly standard OSCs has drawn increasing attention as EBLs were shown to improve both the PCE and stability [12,13]. As is well known, excitons generated under illumination in the OSC active layer must diffuse to the donor/acceptor (D-A) interface and dissociate. The dissociated charges should be collected by the electrodes to contribute to the photocurrent. However, excitons near the organic/metal cathode interface in standard OSCs are quenched, and hence do not contribute to the photocurrent [14]. To suppress this mechanism, an EBL is introduced between the active layer and the metal contact. To block excitons, the material used should possess, in addition to being a good electron transport layer (ETL), a high bandgap to prevent optical excitation. Examples of such materials are

bathocuproine (BCP) and bathophenanthroline (BPhen) [14-16], which efficiently block the excitons. However, the lifetime of a small-molecule solar cell with BCP was reported to be a few hours or even less without encapsulation [17], possibly due to the tendency of BCP to crystallize, especially in a moist environment, yielding micron size domains [18]. BPhen was proven to be superior to BCP in terms of electron-mobility and long-term stability [19,20], although the energy levels of the two materials are comparable. As is well established, the predominant degradation in OSCs is due to in-diffusion of moisture and oxygen [21-23]. The major in-diffusion path is through the top electrode rather than the edges of the device [24,25], so a thicker EBL adjacent to the top electrode is desired to block the penetration of ambient gas molecules to improve the device lifetime in addition to the PCE. However, the thickness of EBLs such as BPhen and BCP is limited by their high bandgap [14, 26], with thicker EBLs significantly increasing the series resistance, deteriorating device performance. One approach to overcome this issue is to n-dope the BPhen or BCP to assist in electron transport [27,28].

BPhen as an EBL has not been used often in inverted OSCs. It was recently co-evaporated with Cs_2CO_3 in inverted P3HT:PCBM-based OSCs, resulting in an improved PCE [29]. The PCE of such cells increased in optimized designs due to improved energy level alignment at the ITO/Cs_2CO_3:BPhen/PCBM interface, increased conductivity in the Cs_2CO_3:BPhen ETL, and hole blocking by BPhen. In contrast, a device with thermally evaporated BPhen only (without Cs_2CO_3) showed a significantly lower PCE [29].

In this study we explored the use of *solution-processed* BPhen and, for comparison, BCP in inverted OSCs of the structure: ITO/CsCl or CsI/BPhen/P3HT:PCBM/MoO_3/Al. For comparison, an OSC with no halide, but only a thin BPhen layer was also tested. The PCE of the OSCs with halide/BPhen reached ~3.5% - 3.7%, while that of the cell with only BPhen was up to

~3.3%, significantly higher than that of a cell with thermally evaporated BPhen [29]. The halide/BPhen cells generally showed a higher PCE. It is possible that by spin-coating BPhen on top of CsCl an effect equivalent to n-doping the EBL is achieved [30].

In a previous study, we showed that CsI spin cast from an aqueous solution can be used in such inverted OSCs as a cathode interlayer to yield a maximal PCE of ~3.4%, comparable to the PCE we obtained with the standard Cs_2CO_3 layer cast from an organic solution. The PCE for the inverted OSCs with CsCl typically reached only ~2.5% [31]. That is, we observed a significant improvement for the OSCs with only BPhen and more so for OSCs with CsCl/BPhen in comparison to the cell with only CsCl. For the OSCs with CsI, we observed a smaller enhancement of ~6-9% in the PCE. The results show that the solution-cast hole blocking BPhen layer in inverted OSCs at the ITO cathode enhances both the PCE and the stability, reducing charge recombination at the organic/cathode interface. When the inverted OSCs with CsI/BPhen were exposed to ambient conditions of high relative humidity (RH ~80%), the cells' attributes were, as expected, inferior and degradation was obviously faster. Interestingly, we show that a film made of ~100 nm diameter polystyrene beads (PSB), deposited on the blank side of the OSC's substrate, increases the short circuit current (J_{sc}) and PCE significantly due to redirection and scattering of the light to enhance absorption in the active layer. The use of the PSB film offers an easy approach to potentially improve devices in an analogous way to microlens arrays fabricated by photolithography [32,33].

3.2 Results and discussion

3.2.1 Effect of solution-processed BPhen interlayer

a. J-V characteristics

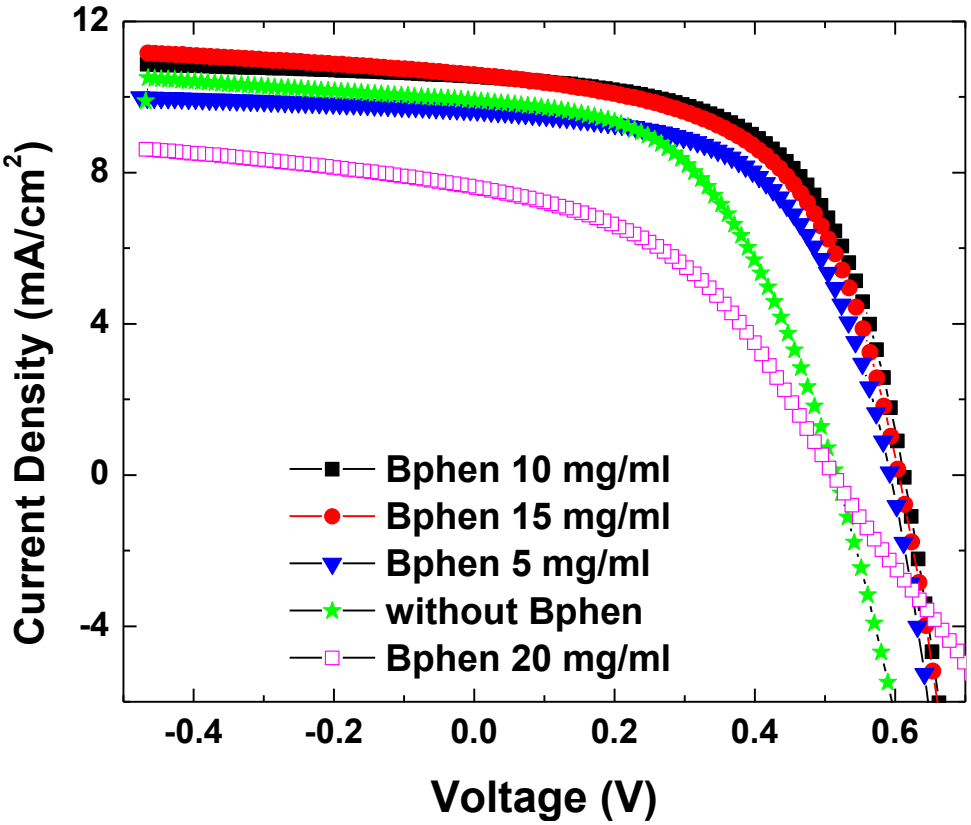

Fig.1. *The effect of the BPhen interlayer on the J-V characteristics of inverted OSCs with CsCl. The interlayers were fabricated from various solution concentrations: 5 mg/ml (solid triangles), 10 mg/ml (solid squares), 15 mg/ml (solid circles), and 20 mg/ml (open squares). The J-V in the absence of a BPhen layer (solid stars) is shown for comparison.*

The PCE of the inverted ITO/CsCl/P3HT:PCBM/MoO_3/Al OSCs was greatly improved by introducing a BPhen interlayer between the CsCl and the P3HT:PCBM active layer. These OSCs with BPhen interlayers were optimized in terms of their *J-V*, EQE, and PCE characteristics by monitoring the effect of the BPhen concentration and the annealing temperature of the BPhen layer. The annealing temperature in the range 40°C to 100°C had a minor effect on the PCE. By changing the BPhen concentration from 0 mg/ml to 20 mg/ml, the PCE improved by up to 46% with an optimal BPhen concentration of ~10 mg/ml compared to OSCs with only CsCl, as shown in Fig. 1 that shows the *J-V* curves for several BPhen concentrations. The open circuit voltage (V_{oc}) and J_{sc} reached maximal values of 0.61 V and 10.5 mA/cm^2, respectively, increases of

16.3% and 10.9%; the fill factor (FF) increased by 13.3%. Once the BPhen concentration exceeded 15 mg/ml, the OSCs' performance deteriorated with increased series resistance R_S (see Table 1) and reduced V_{oc}, J_{sc}, and FF. The improved OSC attributes with BPhen is due to the layer's hole-blocking effect and its higher electron mobility [19,29]. We speculate that the electron mobility may be enhanced further by doping of BPhen with Cs.

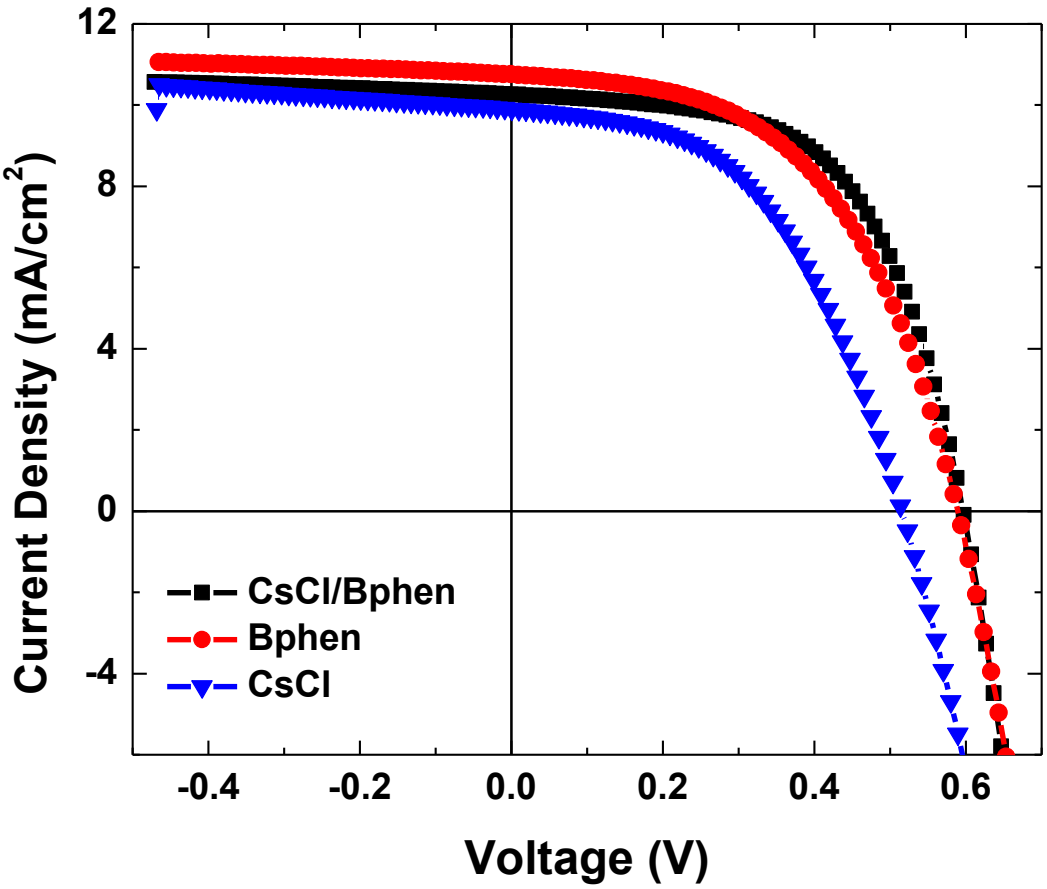

Fig. 2. *The J-V characteristics of inverted cells with CsCl/BPhen (solid squares), BPhen (solid circles) and CsCl (solid triangles) interlayers. The BPhen layer was spin-coated from a solution of 10 mg/ml BPhen in CB (see Fig. 1).*

Figure 2 compares the *J-V* characteristics of inverted cells with CsCl/BPhen, BPhen only, and CsCl only. The attributes of these cells, as well as those with CsI, are summarized in Table 1. By substituting CsCl with BPhen or CsCl/BPhen, the V_{oc} improved from ~0.53 V with CsCl

to ~0.59 V with BPhen and 0.61 V for the optimized CsCl/BPhen. J_{sc} improved from ~9.5 mA/cm^2 to 10.5-10.7 mA/cm^2 with the slightly higher current with the BPhen only layer. However, the FF (57.9%) of the inverted cell with CsCl/BPhen was repeatedly higher than the FF (52.7%) of cells with BPhen only, in accordance with the larger *Rs* in the latter. It is therefore possible that CsCl dopes the BPhen, reducing *Rs*. R_S is higher for the cell with only CsCl due to the formation of an almost stoichiometric insulating film (Cs:Cl ~1.4:1), unlike the situation with the CsI layer where the Cs:I ratio is ~8:1 [31].

Table 1. *Device characteristics of inverted OSCs with CsCl, CsI, BPhen, CsCl/BPhen and CsI/BPhen interlayers. The effect of different BPhen concentrations in CB is also shown. The active layers were dried under a Petri dish for 40 min followed by thermal annealing at ~140°C for ~10 min.*

Interlayer	**BPhen Concentration (mg/ml)**	V_{OC} **(V)**	J_{SC} **(mA/cm^2)**	**FF (%)**	R_S **(Ω)**	R_{SH} **(kΩ)**	**PCE (%)**
CsCl	0	0.53	9.47	51.1	107	5.07	2.55
(0.5 mg/ml)	5	0.59	9.63	57.0	73.0	8.97	3.26
	10	0.61	10.50	57.9	68.6	9.04	3.72
	15	0.61	10.60	56.1	74.6	5.73	3.61
	20	0.52	7.65	43.2	343	2.9	1.71
CsI	0	0.60	9.63	57.2	64.2	6.34	3.31
(0.6 mg/ml)	10	0.58	10.24	59.2	60.1	5.32	3.51
0	10 (BPhen only)	0.59	10.70	52.7	85.8	8.84	3.32

b. EQE

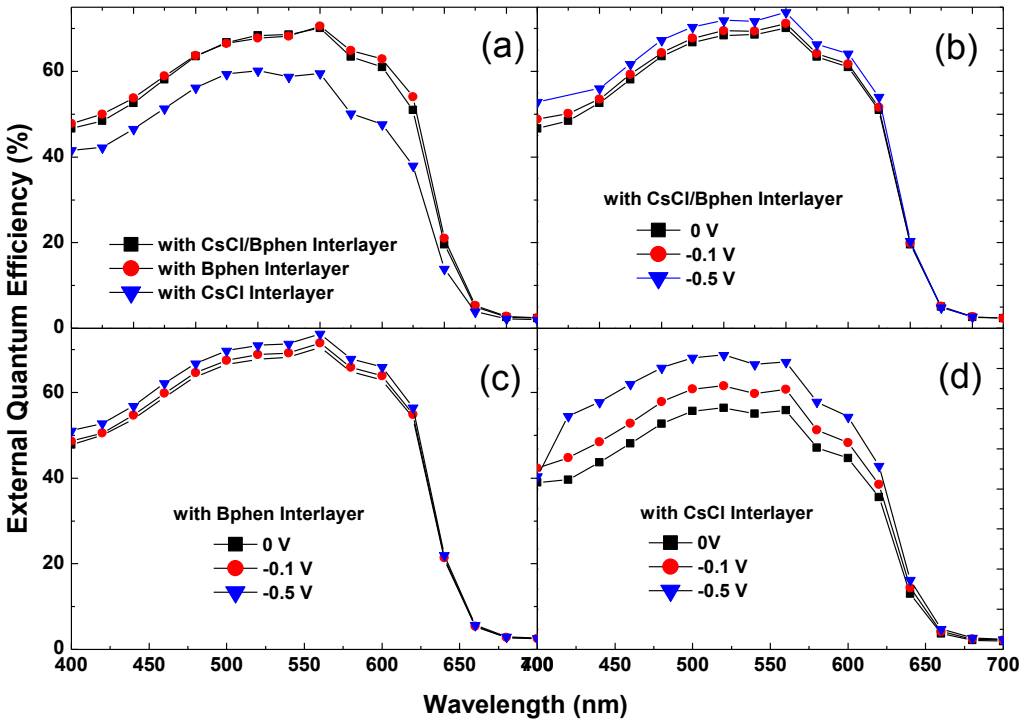

Fig. 3. *EQE of inverted cells with CsCl/BPhen, BPhen, or CsCl as interlayers at various bias voltages: (a) 0 V: CsCl/BPhen (solid squares), BPhen (solid circles) and CsCl (solid triangles);and (b) CsCl/BPhen, (c) BPhen and (d) CsCl at 0 V (squares), -0.1 V (circles) and -0.5 V (triangles).*

The EQE values of the inverted cells with CsCl, BPhen, or CsCl/BPhen interlayers are shown in Fig. 3(a). As expected from the J_{sc} values (see Table 1), the EQE of the cells with CsCl only was the lowest, with the EQE for cells with Bphen slightly higher than that of cells with CsCl/BPhen. Figs. 3(b)-(d) show the EQE of cells with and without a bias voltage. Under -0.1 V, the change in the EQE of cells with Bphen or CsCl/BPhen is minimal, while the EQE of cells with CsCl only changed significantly. Under -0.5 V, the EQE of cells with BPhen or CsCl/BPhen was slightly higher than without a bias, while the EQE of cells with CsCl only increased by ~30%. This behavior indicates that charge extraction is more efficient in cells with BPhen. It is illustrated in Fig. 4 that shows the EQE ratio of -0.1V or -0.5 V bias to 0 V. As clearly seen, the

presence of BPhen reduces charge recombination (by blocking holes) at the ITO electrode [34], while charge recombination is more apparent for the device with CsCl only.

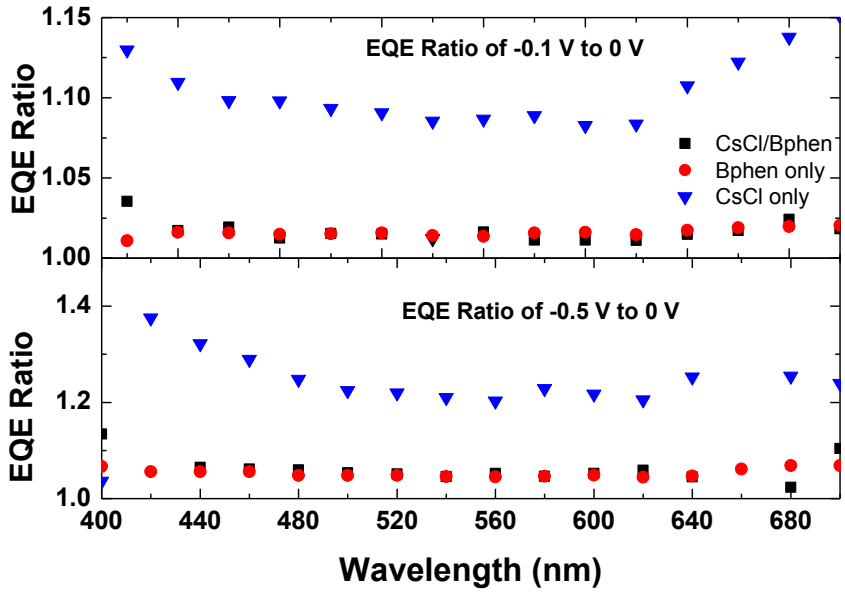

Fig. 4. *EQE ratios of inverted cells with CsCl/BPhen (squares), BPhen (circles), or CsCl (triangles) interlayers.*

c. AFM images of P3HT:PCBM

As seen in the results presented above, the best devices with only BPhen showed a slightly higher J_{SC} than that of devices with CsCl/BPhen though the latter showed consistently larger PCEs. As seen below, the surface morphology of the P3HT:PCBM layer does not appear to contribute significantly to this behavior. The active layer in ITO/CsCl/BPhen/P3HT:PCBM was rougher, with an average surface roughness R_{rms} of 25.4 nm, and the R_{rms} of the active layer in ITO/BPhen/P3HT:PCBM was 18.8 nm. The R_{rms} of P3HT:PCBM in ITO/CsCl/P3HT:PCBM was 25.3 nm, i.e., the BPhen layer did not show a smoothing effect when cast on CsCl. Fig. 5 shows the AFM images of the active layer in these three structures.

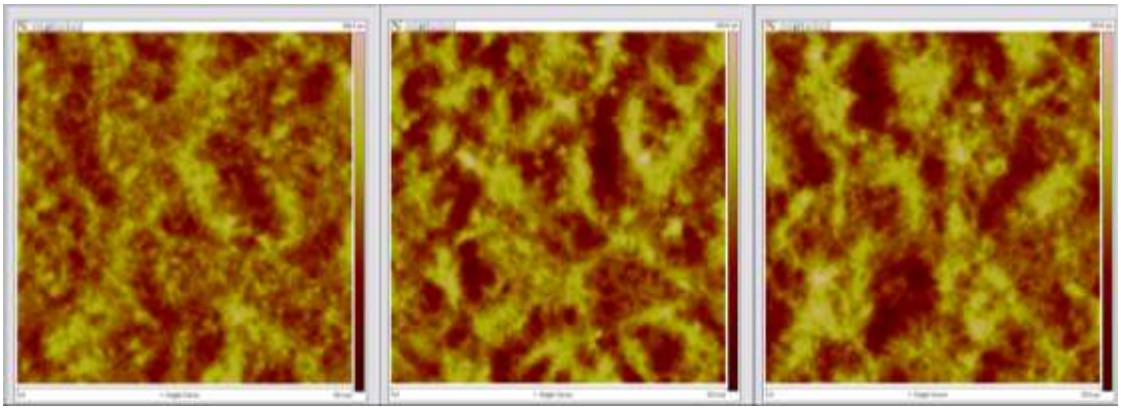

Fig. 5. *AFM images of P3HT:PCBM in: left- ITO/BPhen/P3HT:PCBM, center- ITO/CsCl/P3HT:PCBM, and right- ITO/CsCl/BPhen/P3HT:PCBM. The respective R_{rms} values are 18.8, 25.3, and 25.4 nm.*

In the case of small molecule OSCs, rougher layers were shown to improve performance [35]. However, the surface roughness of P3HT:PCBM in the current structures is much larger and hence variations in roughness from ~19 to ~25 nm do not appear to affect device performance. We note that based on our recent study [31], the top surface is believed to be P3HT-rich.

d. Comparison to BCP interlayer

BCP was chosen as an interlayer for comparison with BPhen, as both materials act as hole blocking layers due to their deep highest occupied molecular orbital (HOMO) levels (-6.6 eV and -6.4 eV for BPhen and BCP, respectively [36,37]).

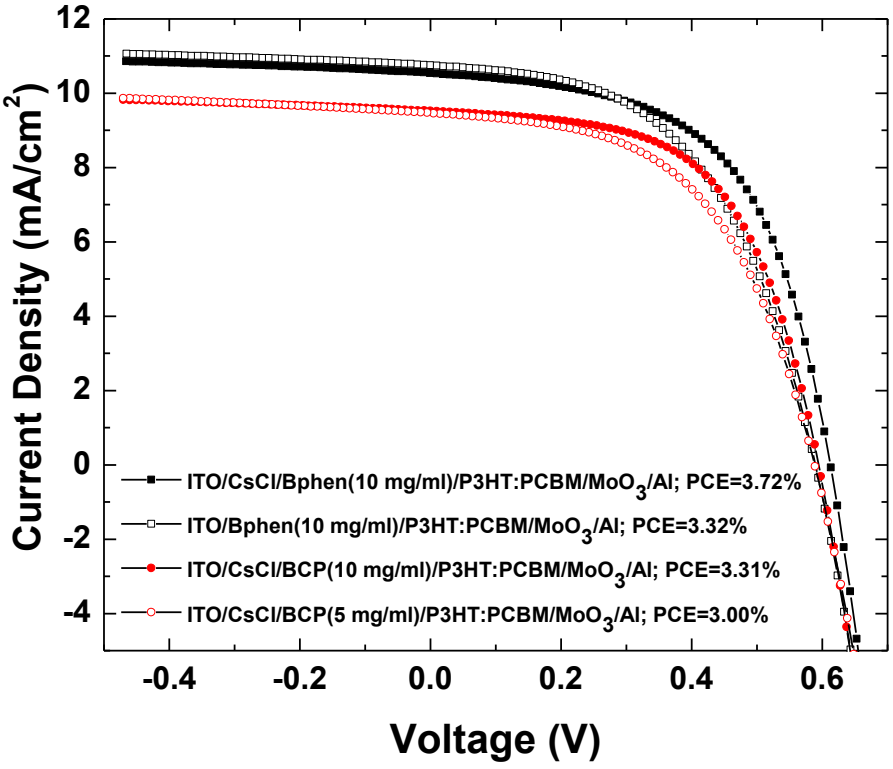

Fig. 6. *The J-V characteristics of inverted cells with CsCl/BPhen (10 mg/ml, solid squares), BPhen (10 mg/ml, open squares), CsCl/BCP (10 mg/ml, solid circles), and CsCl/BCP (5 mg/ml, open circles) as the interlayers.*

Figure 6 demonstrates that BPhen and BCP improve the OSCs' performance. The relatively lower current density of OSCs with BCP likely originates from the lower electron mobility of BCP compared to that of BPhen. The solubility of both BPhen and BCP in DCB is very low, and thus spin-coating the DCB solution of P3HT:PCBM on these layers was not expected to present a major issue, consistent with the XPS data shown next. Moreover the presence of both layers resulted in an improved FF. Table 2 summarizes the attributes of the devices with CBP in comparison to Bphen.

Table 2. *Device characteristics of inverted cells with CsCl/BPhen (10 mg/ml), BPhen (10 mg/ml), CsCl/BCP (10 mg/ml), and CsCl/BCP (5 mg/ml) as the interlayers.*

Interlayer (mg/ml)	V_{OC} **(V)**	J_{SC} **(mA/cm^2)**	***FF*** **(%)**	R_S **(Ω)**	R_{SH} **(kΩ)**	**PCE (%)**
0.5 (CsCl)/10 (BPhen)	0.61	10.50	57.9	68.6	9.04	3.72
10 (BPhen)	0.59	10.70	52.7	85.8	8.84	3.32
0.5 (CsCl)/5 (BCP)	0.59	9.43	54.1	95.3	8.29	3.00
0.5 (CsCl)/10 (BCP)	0.60	9.49	58.6	77.5	11.0	3.31
10 (BCP)	0.53	9.24	50.1	101.0	5.85	2.50

e. XPS analysis of the interlayers

XPS analysis was conducted to verify the presence of BPhen following application of the active layer by spin-coating it from a DCB solution and annealing. To that end, we monitored the C:N ratio of a BPhen layer, and of BPhen or CsCl/BPhen layers on which a solution of DCB was spun. In pristine BPhen, the C:N ratio is 12:1. In all films, i.e., Bphen and CsCl/BPhen unannealed or annealed at 40-80^{o}C, the measured C:N ratio was in the range 11.4 to 18.3. In the unannealed, untreated BPhen film this ratio was 15.1, likely due to C contaminants. In CsCl/BPhen annealed at 80^{o}C followed by spinning on it the DCB solution, the ratio increased up to 18.3. A concentration of 1.5% Cs was also detected and ITO was also seen in this case. This behavior indicates increased C contamination and possibly a slight dissolution of the BPhen layer by DCB with a <10 nm BPhen layer (depth resolution of the XPS) through which the Cs and ITO are partially seen. We note that even though the glass transition temperature of BPhen is 62^{o}C [38], annealing in the 40-80^{o}C range did not have a major effect on cell performance, with annealing at 80^{o}C resulting in a somewhat improved performance.

f. Stability

Importantly, not only was the PCE of the OSCs improved by introducing a BPhen interlayer, but also the stability of unencapsulated cells kept in the dark under ambient conditions was prolonged. The PCE of unencapsulated OSCs with CsCl/BPhen decreased by < 2% three weeks after the cells' fabrication; it decreased by ~15.6% in two months, possibly also due to a significant increase in the relative humidity in the laboratory. A similar behavior was observed for OSCs with CsI/BPhen, where the PCE decreased by 10%, from 3.51% to 3.16%, after 24 days. Upon light soaking for 28 min the PCE increased to 3.55%. The PCE subsequently decreased by 35% to 2.25% after 60 days, but then increased to 2.96% after 15 min of light soaking. These cells were kept at the laboratory's relative humidity of ~30%. Four cells with only BPhen showed an average reduction of ~20% in the PCE two weeks after fabrication. This deterioration is stronger than for the cells with the halide/BPhen, but weaker than that for cells with CsCl only that showed a reduction of over 50% after ~2 weeks when unencapsulated and placed outside the glovebox. The reason for the increased stability, observed for both OSCs with CsCl/BPhen or CsI/BPhen, is currently not clear but may be associated with separating the P3HT:PCBM from the oxygen shown to be present in such inverted cells at the Cs halide layer [31]. Another possibility is reducing degradation induced by the energy released by electron-hole recombination. We are currently conducting a more systematic study to better understand the behavior of the different devices.

3.2.2 Effect of a polystyrene beads layer

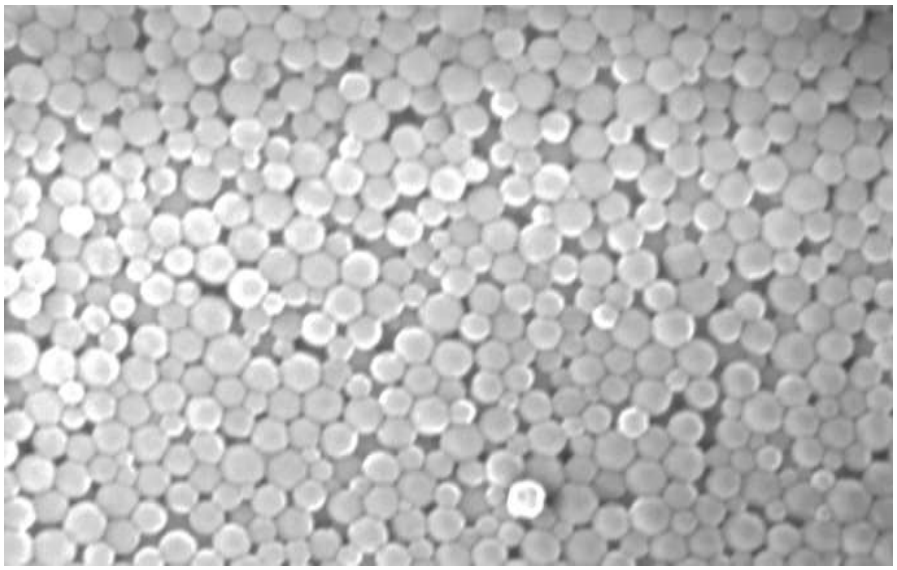

Fig. 7. *SEM image of a PSB film on the glass substrate opposite to the inverted OSC.*

OSCs exposed to ambient conditions with a high relative humidity (RH ~80%) deteriorated, as expected, faster than OSCs kept under dryer (RH ~ 30%) ambient conditions. Table 3 summarizes average OSC attributes of nine cells of the structure ITO/CsI/BPhen/P3HT:PCBM/MoO_3/Al: as-prepared devices (but exposed to ~80% RH for several hours, which typically results in inferior devices), the same OSCs that were kept in the dark at ~80% RH for eight days or fifteen days, and these same cells with an added PSB film, whose SEM image is shown in Fig. 7. We note that the performance of the cells after 8 and 15 days were comparable, hence we present averaged attributes. Fig. 8 shows the *J-V* characteristics of such a typical cell.

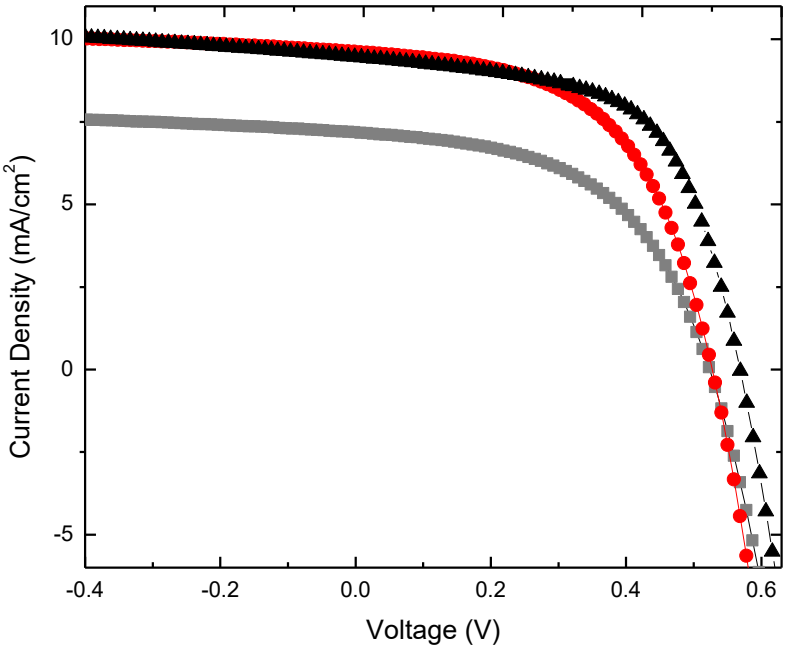

Fig. 8. *J-V characteristics of an as-prepared (triangles) and eight days old cell exposed to ~80% RH before (squares) and after (circles) application of a PSB film.*

***Table. 3**. Attributes (averaged) of nine as-prepared inverted OSCs, the same devices following 8 or 15 days in the dark at ~80% RH, and the same cells with an added PSB film. The cells structure was ITO/CsI/BPhen/P3HT:PCBM/MoO_3/Al.*

As prepared cells				**8 or 15 day old cells**				**8 or 15 day old cells+PSB film**			
Voc (V)	*Isc* (mA)	*FF*	PCE (%)	*Voc* (V)	*Isc* (mA)	*FF*	PCE (%)	*Voc* (V)	*Isc* (mA)	*FF*	PCE (%)
0.57	1.03	59.6	3.18	0.53	0.77	54.0	2.01	0.55	1.02	56.3	2.87
±0.01	±0.03	±2.2	±0.12	±0.01	±0.02	±2.0	±0.09	±0.01	±0.04	±1.5	±0.12

As seen, after 8 to 15 days the V_{oc}, I_{sc}, FF, and PCE decreased significantly. These values, mostly *Isc* and PCE, improved following application of a PSB film. Note that the nine cells were of two batches, which increases the variations in the attributes.

The increase in the V_{OC} upon addition of the PSB film to the nine cells was on average 4.2±1.4 %, the increase in J_{SC} was 31.7±4.0 %, in the FF 4.2±1.4%, and in the PCE 43.2±5.4%. The decrease in the PCE relative to the initial value was 36.8±3.7% without the PSB and only 9.6±5.0% with the PSB film.

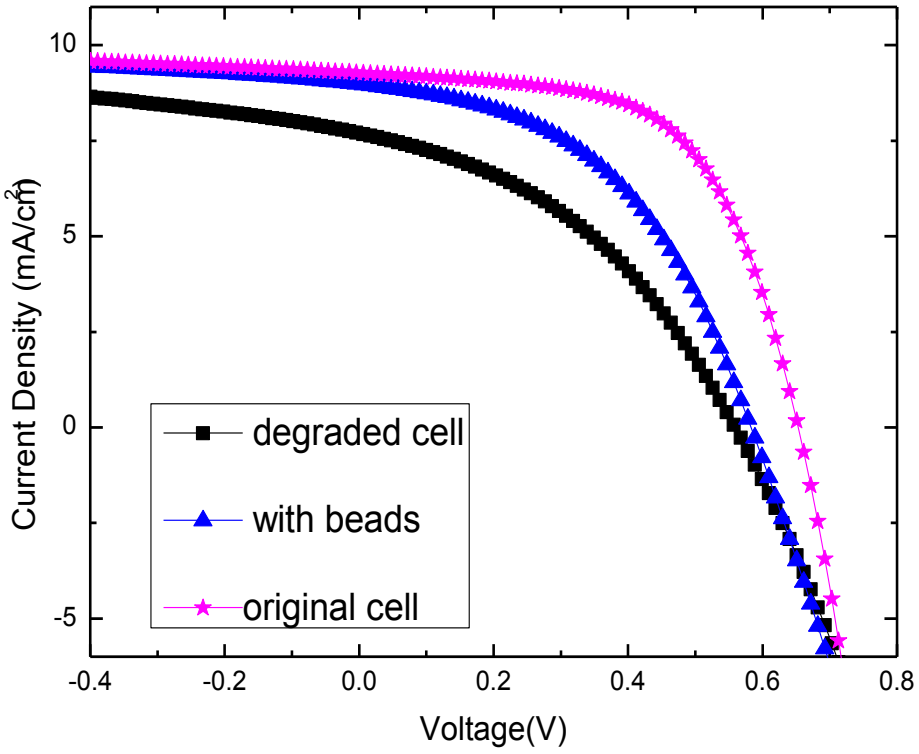

Fig. 9. *J-V characteristics of an as-prepared, intentionally deteriorated (see text), and improved cell with a PSB film. The cell structure was ITO/CsCl/BPhen/P3HT:PCBM/MoO_3/Al cell.*

To further verify the-above described behavior we compared the *J-V* characteristics (Fig. 9) of nominally identical cells of the structure glass/ITO/CsCl/BPhen/P3HT:PCBM/MoO_3/Al with and without the PSB film after intentionally deteriorating the devices' performance by placing them in a closed plastic chamber containing a beaker with water heated to ~90^{o}C for over 3 days. This experiment was performed on several cells with all exhibiting similar results. We note, however, that though the qualitative behavior was reproducible, absolute values varied among cells of different batches.

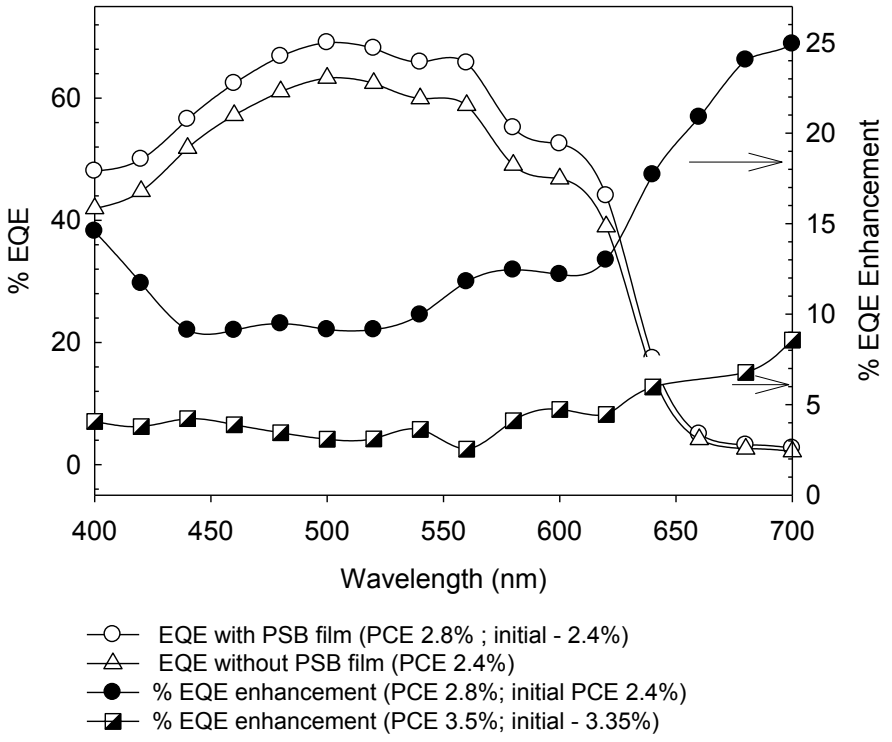

Fig. 10. *EQE spectra of an ITO/CsCl/BPhen/P3HT:PCBM/MoO_3/Al cell with an initial PCE of 2.4% before and after application of a PSB film. The % EQE enhancement is also shown, including for a cell with an initial PCE of ~3.35%.*

We tested also the effect of the PSB film when applied to cells with higher initial PCE values (i.e., PCE values at which the PSB film was applied) in comparison to the deteriorated cells with PCE ~2% described in Fig. 8 and Table 3. Figure 10 shows the increase in the EQE vs wavelength for cells with initial PCEs of 2.4 and 3.35%. The figure shows also the EQE of the former cell before and after application of the PSB film. As seen, the enhancement is smaller for the cell with the higher initial PCE, however, even for the as-prepared cell the EQE increased by ~4% at wavelengths up to ~550 nm and by ~10% at 650 nm.

As the application of the PSB film is not optimized and additional studies are needed to determine the best film application approach (whether spin coated or drop cast) and thickness, it is possible that better enhancements will be achieved with an optimized PSB film.

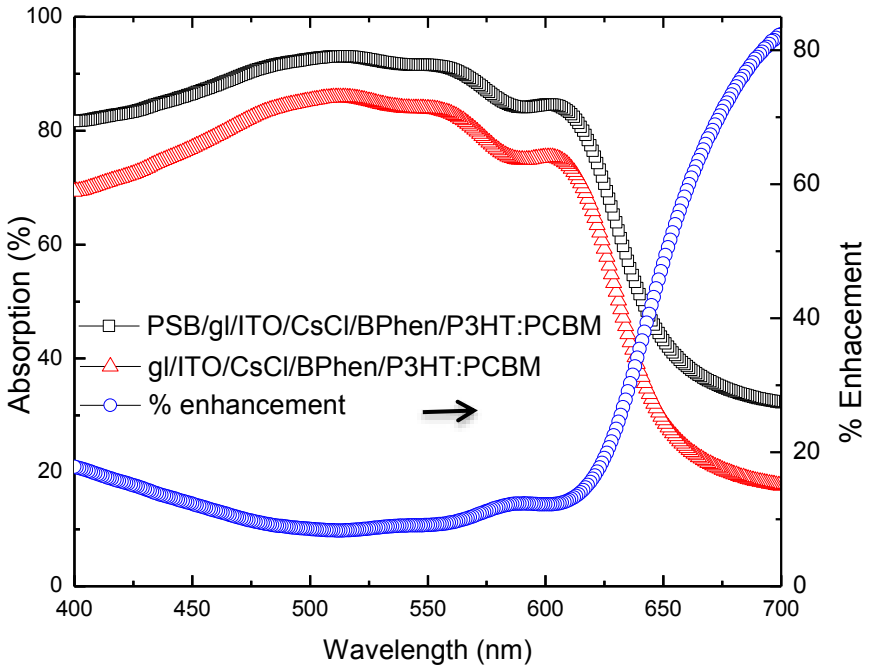

Fig. 11. *Absorption and its relative increase for an ITO/CsCl/BPhen/P3HT:PCBM structure with and without a PSB film. The absorption spectra of glass/ITO and PSB/glass/ITO are also shown.*

To demonstrate the effect of the PSB film we compared the absorption of as-prepared ITO/CsCl/BPhen/P3HT:PCBM structures with and without a PSB film. Fig. 11 shows the results, which indicate increased absorption in the presence of the PSB film. This enhanced light absorption results in enhancement in J_{SC} and PCE. As seen, the addition of the PSB film enhances the absorption over the entire wavelength range, with the strongest increase at longer wavelengths, as expected. We note that, consistent with the EQE behavior (Fig. 10), the enhancement in the absorption was much stronger (> 20% at ~500 nm and > 60% at 625 nm) in films degraded by exposure to ~90% RH atmosphere, where degradation decreases the absorption [39].

In inverted cells, where light is reflected toward the absorbing layer from the metal anode, absorption likely increases so that the effect of the PSB film on the EQE may be lower than that observed for the absorption of ITO/CsCl/BPhen/P3HT:PCBM structures. Moreover, the EQE reflects also charge collection, which may be responsible for the relatively reduced PSB effect on it.

Overall, the results indicate that in addition to improving device efficiency and stability by using a solution-processed BPhen interlayer, a PSB film can further assist in improving devices, and importantly, their long-term performance. This behavior is associated with light direction and scattering by the beads that enhance the absorption in the active OSC layer, possibly similarly to the effect of microlens fabricated using soft photolithography techniques [32], but with a very economic approach.

3.3 Conclusions

The PCE of inverted solar cells with the structure ITO/CsCl/P3HT:PCBM/MoO_3/Al improved by up to 46% (from ~2.5% to ~3.7%) by adding a solution-processed BPhen layer between the CsCl (spin-coated from aqueous solution) and the active layer. The results indicate that the BPhen interlayer blocks holes from reaching the cathode and hence diminishes charge recombination at the ITO interface. Interestingly, the degradation of such non-encapsulated devices with Cs halide/BPhen (kept outside the glovebox) was significantly lower than that of cells without the Bphen layer. The PCE of cells with CsCl/BPhen kept in dark at ambient environment decreased by only 2% in ~3 weeks in comparison to ~60% for cells devoid of the BPhen layer. The PCE of unencapsulated cells with BPhen only kept under ambient conditions decreased by 15.6% after two months. The as-prepared cells with the CsI interlayer showed a smaller increase of only ~6-9% in the PCE upon addition of BPhen, which was expected as the recombination is already lower in ITO/CsI/P3HT:PCBM/MoO_3/Al cells. Similarly to the CsCl/BPhen cells, those with CsI/BPhen showed a significantly improved stability in comparison to cells devoid of the BPhen layer. This effect of BPhen could be due to two mechanisms: (i) suppression of electron-hole recombination that eliminates degradation induced by the energy released by such recombination, and (ii) formation of a barrier for oxygen diffusion from the ITO to the active layer. We also note that solution-processed BPhen resulted in better cells than those with an evaporated layer. Cells with solution-processed BCP were also fabricated to compare different hole-blocking layers. Of the two, BPhen offers the best performance, possibly due to its higher electron mobility. Comparing EQE spectra obtained at different voltages for cells with CsCl and CsCl/BPhen confirmed that the BPhen layer reduces recombination at the ITO cathode. The results indicate that spin coating solutions of BPhen is a low-cost and easy approach to

introduce a hole-blocking layer in inverted structures, in particular with a Cs halide interlayer, alluding to Cs doping, for increased PCE and stability.

Application of a PSB film to the blank side of the glass substrate of the OSC with CsI/BPhen restored J_{sc} and increased the PCE to within an average of ~10% of the original values for 8-15 days old cells exposed to a relative humidity of ~80%. Improved long-term performance was similarly observed for cells with CsCl/BPhen with an added PSB film. This approach presents a simple route for enhancing absorption in degraded cells via directing and scattering the light to enhance the optical path within the active layer, and thus increase J_{sc} and PCE. As-prepared cells also exhibited an enhanced performance but to a lesser degree. Comparing the enhancement in the absorption and EQE spectra by the PSB film indicates that charge collection may hinder cell performance, as the enhancement in EQE was relatively lower. Additional studies are under way to better control the PSB film thickness and morphology and apply it to other cell types.

3.4 Experimental

3.4.1 Materials

P3HT was obtained from Rieke Metals and PCBM from nano-C; both materials were used without further purification. A solution of 1:1 weight ratio of P3HT:PCBM in 1,2-dichlorobenzene (DCB), with a concentration of 34 mg/mL was used. The P3HT solution was filtered using a 0.22 μm Millex PTFE filter before it was mixed with PCBM. The mixture was then stirred for 24 h before spin-coating. BPhen, BCP, CsCl, and CsI were purchased from Sigma Aldrich. BPhen was dissolved in chlorobenzene (CB) (purchased from Sigma Aldrich). An aqueous suspension of 10% solid PSB with a mean particle size of ~100 nm was purchased from Sigma Aldrich. The devices' area was 0.11 cm^2.

3.4.2 Procedures

Various inverted cells with the structure ITO/CsCl or CsI/BPhen/P3HT:PCBM/MoO_3/Al were fabricated for studying the effect of BPhen as a hole-blocking layer. CB solutions of BPhen with concentrations ranging from 1 mg/mL to 20 mg/mL were used in cell fabrication. The concentrations of CsI and CsCl were 0.6 mg/ml and 0.5 mg/ml, respectively, as these are the optimized value obtained in our previous work [31]. The CsCl or CsI layers were prepared by spin-coating at 4000 rpm for 60 s and then baking at 150°C for ~20 min. The following P3HT:PCBM active layer was spun using a 34 mg/mL DCB solution with a 1:1 weight ratio of the components. Prior to spin-coating the solution was stirred on a hot plate at 45°C for over 24 h. The active layers in the different cells were dried under a petri-dish and annealed at 150°C for 12 min. Next, a 9 nm MoO_3 layer was thermally evaporated on top of the organic layer followed by the 120 nm Al electrode.

For one of the experiments we conducted, we intentionally degraded a cell in a high RH environment. The high RH was achieved by placing the cell in an enclosed chamber that contained a beaker full of water at a temperature just below boiling. This high RH was necessary to observe degradation in ~3-4 days.

3.4.3 Measurements

J-V characteristics of the OSCs were obtained using a 100 mW/cm^2 ELH bulb for illumination. The light intensity was monitored with a calibrated Si-photodiode, and the current density was matched to the value obtained from the external quantum efficiency (EQE) measurement. The EQE was measured with and without a voltage bias. XPS data were obtained using a Physical Electronics 5500 multi-technique system, and atomic force microscopy (AFM) images were acquired with a Digital Instruments system. Absorption measurements of various structures were obtained using a CARY 5000 spectrophotometer for monitoring the

transmittance and reflection. We note that all experiments were performed multiple times to ensure the validity of the conclusions. Low-level Si contaminant was seen in all devices independent of treatment or interlayers. This may be related to the lubricant present in plastic syringes used in device fabrication and hence unintentional Si incorporation [40]. We also note that the OSCs attributes vary quantitatively from batch to batch, including for materials from various sources.

Acknowledgments

RS acknowledges partial support by the Iowa Energy Center and an EAGER NSF grant. Ames Laboratory is operated by Iowa State University for the US Department of Energy (USDOE) under Contract No. DE-AC 02-07CH11358. TX, FF, MC, and JWA were partially supported by Basic Energy Sciences, Division of Materials Science and Engineering, USDOE.

References

[1] L. Dou, J. You, J. Yang, C. C. Chen, Y. He, S. Murase, T. Moriarty, K. Emery, G. Li, Y. Yang, Nature Photon. 6 (2012) 180.

[2] H. Y. Chen, J. Hou, S. Zhang, Y. Liang, G. Yang, Y. Yang, L. Yu, Y. Wu, G. Li, Nature Photon. 3 (2009) 649.

[3] Y. Liang, Z. Xu, J. Xia, S. T. Tsai, Y. Wu, G. Li, C. Ray, L. Yu, Adv. Mater. 22 (2010) E135.

[4] T. Y. Chu, J. Lu, S. Beaupré, Y. Zhang, J.R. Pouliot, S. Wakim, J. Zhou, M. Leclerc, Z. Li, J. Ding, Y. Tao, J Am Chem Soc. 133 (2011**)** 4250.

[5] M. A. Green, K. Emery , Y. Hishikawa , W. Warta , Prog. Photovolt: Res. Appl. 19 (2010**)** 84.

[6] H. Neugebauer, C. Brabec, J. C. Hummelen, N. S. Sariciftci, Sol. Energy Mater. Sol. Cells 61 (2000) 35.

[7] T. Jeranko, H. Tributsch, N. S. Sariciftci, J. C. Hummelen, Sol. Energy Mater. Sol. Cells 83 (2004) 247.

[8] S. Bertho, I. Haeldermans, A. Swinnen, W. Moons, T. Martens, L. Lutsen, D. Vanderzande, J. Manca, A. Senes, A. Bonfiglio, Sol. Energy Mater. Sol. Cells 91 (2007) 385.

[9] J. A. Hauch, P. Schilinsky, S. A. Choulis, R. Childers, M. Biele, C. J. Brabec, Sol. Energy Mater. Sol. Cells 92 (2008) 727.

[10] F.C. Krebs, T. Tromholt, M. Jorgensen, Nanoscale 2 (2010) 873.

[11] C.H. Peters, I.T. Sachs-Quitana, J.P. Kastrop, S. Beaupré, M. Leclerc, M.D. McGehee, Adv. Energy Mater. 1 (2011) 491.

[12] Y. Lare, B. Kouskoussa, K. Benchouk, S. OuroDjobo, L. Cattin, M. Morsli, F.R. Diaz, M. Gacitua, T. Abachi, M.A. delValle, F. Armijo, Gaston A. East, J.C. Bernède, J. Phys. Chem. Solids 72 (2011**)** 97.

[13] T. Zhuang, Z. Su, Y. Liu, B. Chu, W. Li, J. Wang, F. Jin, X. Yan, B. Zhao, F. Zhang, D. Fan, Appl. Phys. Lett. 100 (2012) 243902.

[14] P. Peumans, V. Bulovic, S. R. Forrest, Appl. Phys. Lett. 76 (2000) 2650.

[15] P. Peumans, S.R. Forrest, Appl. Phys. Lett. 79 (2001) 126.

[16] A. Opitz, J. Wagner, W. Br€utting, I. Salzmann, N. Koch, J. Manara, J. Pflaum, A. Hinderhofer, F. Schreiber, IEEE J. Sel. Top. Quantum Electron. 16 (2010) 1707.

[17] S. Heutz, P. Sullivan, B.M. Sanderson, S.M. Schultes, T.S. Jones, Sol. Energ. Mater. Sol. Cells, 83 (2004) 229.

[18] P. Peumans, A. Yakimov, S.R. Forrest, J. Appl. Phys. 93 (2003) 3693.

[19] S. Naka, H. Okada, H. Onnagawa, T. Tsutsui, Appl. Phys. Lett. 76 (2000) 197.

[20] T. Zhuang, Z Su,Y. Liu, B. Chu, W. Li, J. Wang, F. Jin, X. Yan, B. Zhao, F. Zhang, D. Fan, Appl. Phys. Lett. 100 (2012) 243902.

[21] H. Neugebauer, C. Brabec, J. C. Hummelen, N. S. Sariciftci, Sol. Energy Mater. Sol. Cells 61 (2000) 35.

[22] K. Kawano, R. Pacios, D. Poplavskyy, J. Nelson, D. D. C. Bradle, J. R. Durrant, Sol. Energy Mater. Sol. Cells 90 (2006) 3520.

[23] M. Jørgensen, K. Norrman, F. C. Krebs, Sol. Energy Mater. Sol. Cells 92 (2008) 686.

[24] K. Norrman, N. B. Larsen, F. C. Krebs, Sol. Energy Mater. Sol. Cells 90 (2006) 2793.

[25] F. C. Krebs, K. Norrman, Prog. Photovolt. 15 (2007) 697.

[26] B. P. Rand, J. Li, J. Xue, R. J. Holmes, M. E. Thompson, S. R. Forrest, Adv. Mater. (Weinheim, Ger.) 17 (2005) 2714.

[27] D. Gebeyehu, M. Pfeiffer, B. Maennig, J. Drechsel, A. Werner, K. Leo, "Thin Solid Films," 29 (2004) 451.

[28] M. Y. Chan, S. L. Lai, K. M. Lau, C. S. Lee, S. T. Lee, Appl. Phys. Lett. 89 (2006) 163515.

[29] Z. Xu, J. Yang, F. Sun, S.T. Lee, Y-Q. Li, and J. Tang, Org. Electron. 13 (2012) 697.

[30] T. D. Pawlik, D. Y. Kondakov, W. J. Begley, R. H. Young, J. SID 18/4 (2010) 277.

[31] T. Xiao, W. Cui, M. Cai, J. W. Anderegg, J. Shinar, R. Shinar, Org. Electron. 14 (2013) 267.

[32] J.-M. Park, Z. Gan, W. Y. Leung, Z. Ye, K. Constant, J. Shinar, R. Shinar, K.-M. Ho, Opt. Exp. 19 (2011**)** A786.

[33] J. D. Myers, W. Cao, V. Cassidy, S.-H. Eom, R. Zhou, L. Yang, W. You, J. Xue, Energy & Environmental Science 5 (2012**)** 6900.

[34] V. Dalal, M. Leonard, J. Booker, A. Vaseashta, "Quantum efficiency of amorphous alloy solar cells*",* Proc. of the 18th IEEE Photovoltaic Spec. Conf. (1985) 837.

[35] T. Xiao, W. Cui, M. Cai, R. Liu, J. W. Anderegg, J. Shinar, R. Shinar, J Photon Energy 2 (2012) 021006-1.

[36] M.-H. Chen, Y.-H. Chen, C.-T. Lin,G.-R. Lee, C.-I Wu, D.-S. Leem, J.-J. Kim, and T.-W. Pi, J. Appl. Phys. 105 (2009) 113714.

[37] M. Ichikawa, J. Amagai, Y. Horiba, T. Koyama, Y. Taniguchi, J. Appl. Phys. 94 (2003) 7796.

[38] B. W. D'Andrade, S. R. Forrest, A. B. Chwang, Appl. Phys. Lett. 83 (2003) 3858.

[39] M. O. Reese, A. M. Nardes, B. L. Rupert, R. E. Larsen, D. C. Olson, M. T. Lloyd, S. E. Shaheen, D. S. Ginley, G. Rumbles, N. Kopidakis, Adv. Func. Mater. 20 (2010) 3476.

[40] K. R. Graham, J. Mei, R. Stalder, J.W. Shim, H. Cheun, F. Steffy, F. So, B. Kippelen, J. R. Reynolds, Appl. Mater. Interfaces 3 (2011) 1210.

Chapter 4: Electronic measurements of defects in photodegraded polymer:fullerene solar cells

Fadzai Fungura, William R. Lindemann, Joseph Shinar*, and Ruth Shinar*

Abstract

Photodegradation of organic solar cells remains a key challenge impeding this green technology. This work presents electronic measurement results that show the creation of defects by light soaking in a pure nitrogen atmosphere of a low (1.58 eV) bandgap polymer:fullerene bulk heterojunction (BHJ) solar cell. Importantly, such light soaking of polymer-only and PCBM-only devices did not generate an observable increase in density of defect states at molecular interfaces whereas in BHJ solar cells, there were increased defects at the donor-acceptor (D/A) interface. Electronic monitoring of fundamental properties of the BHJ solar cells revealed increased deep defect density at the D/A interface and in the polymer, charge recombination, as well as decreased external quantum efficiency, charge collection, short circuit current, open circuit voltage, and hole mobility following exposure of the cells to solar irradiation without exposure to ambient air. The data demonstrate that UV and blue light are largely responsible for this short-term photodegradation; filtering the UV light during irradiation reduces the short-term photodegradation drastically.

4.1 Introduction

Polymer solar cells (PSCs) have been studied extensively because of their potential as a lightweight, flexible, and low-cost renewable energy source. Significant enhancement in the power conversion efficiency (PCE) [1-13] to ~11%, was achieved by e.g., using low bandgap polymers [1-10] and developing approaches aimed at controlling the morphology of the active layer utilizing thermal annealing [11], solvent annealing [12], mixed solvents [4-13], or additives [1-7].

Low bandgap polymers improve the PCE by absorbing more sunlight, which results in a larger short circuit current density J_{sc}. A larger open circuit voltage V_{oc} is achieved by lowering the energy level of the highest occupied molecular orbital (HOMO) of the polymer (i.e., making it more negative relative to the vacuum level) [1-6]. Extensive efforts are directed at understanding degradation mechanisms in order to increase the PSCs' lifetimes [14-25]. PSCs degrade rapidly when exposed to moisture and oxygen [14-17] as well as light [18-22]. For example, light exposure at wavelengths of 350 to 1100 nm of poly-3-hexylthiophene (P3HT):[6,6]-phenyl-C_{60}-butyric acid methyl ester (PCBM) solar cells resulted in an increase in defect states in P3HT and defects assigned to the P3HT/PCBM interface [20], although to date the microscopic nature of this light-induced effect has not been revealed.

An interesting class of low-bandgap polymers is a series composed of alternating benzo[1,2-b:4,5-b']dithiophene (BDT) and thieno[3,4-b]-thiophene (TT) units (denoted PBDTTTs) [23], which exhibit high PCEs (up to 9% for standard solar cells and 10% for inverted cells) for polymer:fullerene bulk heterojunction (BHJ) solar cells. These polymers have a high absorption in the long wavelength region up to 720 nm and high carrier mobilities [23,24]. Poly[4,8-bis(5-(2-ethylhexyl)thiophen-2-yl)benzo[1,2-b;4,5-b']dithiophene-2,6-diyl-alt-(4-(2-ethylhexyl)-3-fluorothieno[3,4-b]thiophene-)-2-carboxylate-2-6-diyl)], PBDTTT-EFT (Fig. 1) has a HOMO level of -5.24 eV, a LUMO level of -3.66 eV, and consequently a bandgap E_g = 1.58 eV. BHJ solar cells based on the closely related poly[(4,8-bis-(2-ethylhexyloxy)-benzo[1,2-b;4,5-b]dithiophene)-2,6-diyl-alt-(4-(2-ethyl-hexanoyl)-thieno[3,4-b]thiopene)-2,6-diyl] (PBDTTT-C):PCBM have been shown to be unstable with respect to heat [25]. To improve the stability and long-term performance of PSCs, understanding defect states, their source, and how they act as trapping and recombination centers is important. Hence, in this paper the effect of light-induced

degradation on the fundamental material and device properties of PBDTTT-EFT:$PC_{70}BM$ was broadly investigated.

Several techniques were used to examine how the PSCs' properties change due to light-induced degradation and to identify the source of this change. Current density-voltage (*J-V*) characteristics were monitored over time to analyze the changes in J_{sc}, V_{oc}, the fill factor *FF*, and PCE. The external quantum efficiency (EQE) of the PSCs before and after degradation was measured to investigate the change in the light absorption spectrum and charge collection. For analysis of midgap defects at or near the PBDTTT-EFT:PCBM interface and in the polymer, density of states (DOS) and subgap quantum efficiency (QE) measurements were performed. Space-charge limited current (SCLC) hole mobility measurements were performed to monitor the change in hole mobility of irradiated PBDTTT-EFT films.

4.2. Experimental

4.2.1. Materials and solutions

PBDTTT-EFT was obtained from Solarmer Materials (Beijing) Inc. and $PC_{70}BM$ from Solaris Chem Inc. Both materials were used with no further purification. A solution of 1:1.5 weight ratio of PBDTTT-EFT:$PC_{70}BM$ in 1,2- dichlorobenzene (DCB) purchased from Sigma Aldrich, with a concentration ratio of 10:15 mg/mL was used. The PBDTTT-EFT solution was filtered using a 0.22 μm Millex PTFE filter before mixing with $PC_{70}BM$. The mixture was stirred for 24 h on a hot plate at a temperature of 70°C before spin-coating. Clevios™ HTL Solar poly (3, 4-ethylenedioxythiophene) polystyrene sulfonate (PEDOT:PSS) was purchased from Heraeus Precious Metals, and was filtered using a 0.45 μm PVDF filter prior to spin-coating. 1,8 diiodooctane (DIO) additive was purchased from sigma Aldrich.

4.2.2. Device fabrication

PSCs with the structure ITO/PEDOT:PSS/PBDTTT-EFT:$PC_{70}BM$/Ca/Al were fabricated for studying photodegradation. Similarly, prepared polymer and $PC_{70}BM$ only devices, i.e., ITO/PEDOT:PSS/PBDTTT-EFT or $PC_{70}BM$/Ca/Al, were also examined. ITO-coated glass slides with a sheet resistance of ~15 ohm/square were cleaned with a surfactant for 15 min. Next, the substrates were placed under running deionized water for 15 min, followed by sonication in isopropanol and then in acetone and again in isopropanol for 5 min for each step. A ~40 nm PEDOT:PSS layer was spin coated on top of cleaned glass/ITO substrates [26]. The PEDOT:PSS was dried at 150°C for 20 min in ambient atmosphere before transferring the substrates into a glovebox. 3 vol.% diiodooctane (DIO) was added to the PBDTTT-EFT:$PC_{70}BM$ mixture and the blend was spin coated at 900 rpm in the glovebox. Next, 65 μL of methanol were spin coated on top of the active layer at 4000 rpm [1]. After loading the samples in a vacuum chamber, 20 nm Ca and 100 nm Al were thermally evaporated as the top electrode at a pressure < 1×10^{-6} Torr. The active area of the devices was 0.106 cm^2. The BHJ structures that were used for degradation studies showed optimized initial PCE = 8.7%. For mobility measurements, the structure ITO/PEDOT:PSS/PBDTTT-EFT/Au was used. The thickness of the PBDTTT-EFT layer measured with a profilometer was 160 nm.

4.2.3. Device characterization

Light *J–V* characteristics of the PSCs were obtained using a 100 mW/cm^2 ELH bulb for illumination. The light intensity was monitored with a calibrated Si photodiode. Transmittance measurements of PBDTTT-EFT films before and after photodegradation were obtained using a CARY 5000 spectrophotometer. Reflection measurements were obtained using a HR4000 spectrometer. For photodegradation studies samples were exposed to 100 mW/cm^2 (1 sun) full

solar simulator spectrum for 24 hours using a xenon source solar simulator with appropriate filters to simulate AM1.5 sunlight. The cells were kept in a nitrogen-filled glovebox during the course of the degradation measurements. Post-degradation *J-V* and defect density measurements were all performed in the glovebox without exposing the samples to air. Samples were cooled by a fan during irradiation. Cell attributes, i.e., the PCE, J_{sc}, V_{oc}, and *FF* were measured at different irradiation times. DOS measurements were obtained by measuring the capacitance as a function of frequency (in the range 1 Hz to 200 kHz) $C(f)$ and as a function of voltage $C(V)$ using a HIOKI LCR meter. Mobility measurements were performed in the glovebox with the sample connected to a Keithley source. During each measurement, the sample was kept in the dark and the current (using the current source) and corresponding voltage were recorded. The hole mobility measurements were performed 6 times and the error was determined by the standard deviation of each point multiplied to achieve 95% confidence [27].

4.3. Results and discussion

4.3.1. Effect of processing conditions

4.3.1.1. J-V, absorption, and EQE

Fig. 1 shows the molecular structure of PBDTTT-EFT and the energy levels of the materials within the PSCs.

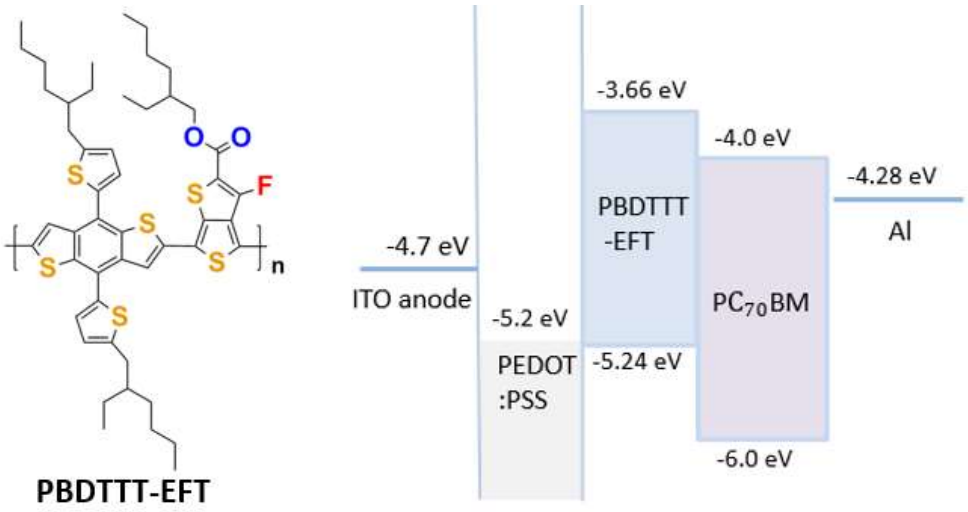

Fig. 1. *Molecular structure of PBDTTT-EFT, the HOMO and LUMO energy levels of the cells' materials, and the Fermi levels of the electrodes.*

PBDTTT-EFT:PCBM BHJ solar cells have a high efficiency when DIO is added to the PBDTTT-EFT and PCBM in 1, 2 DCB solution prior to spin-coating. In this work, we consistently got efficiencies higher than 8% when DIO was added less than 30 minutes prior to spin-coating followed by spin-coating methanol at 4000 rpm on top of the active layer (methanol washing). However without adding DIO, the J_{sc}, V_{oc}, FF and hence PCE was relatively very low. Fig. 2 below shows the *J-V* characteristics for various processing conditions.

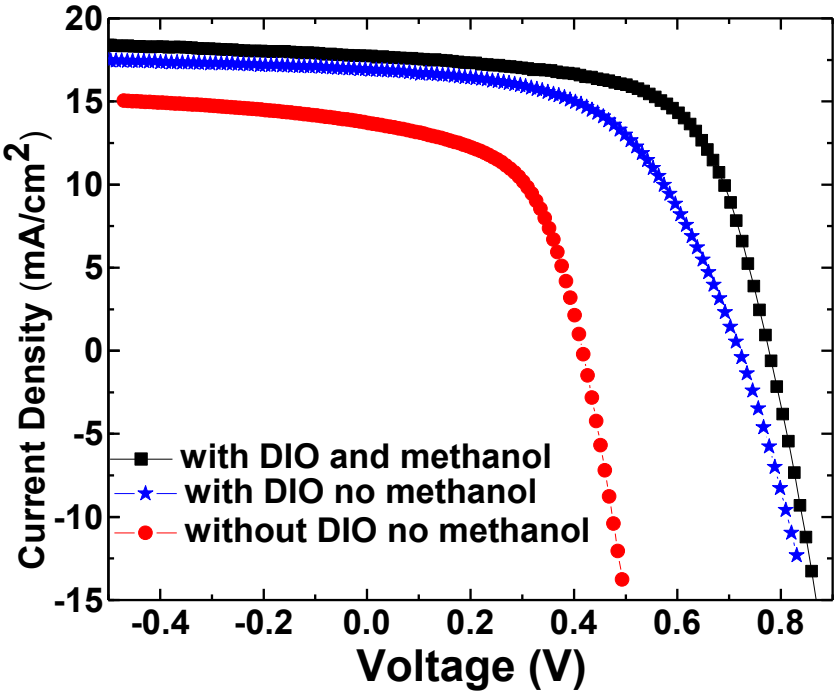

Fig. 2. *J-V characteristics of solar cells with DIO added 20 mins prior to spin-coating and washed with methanol (black squares), DIO added 20 mins prior to spin-coating without methanol washing (blue stars) and without both DIO and methanol washing (red circles)*

	Voc [V]	Jsc [mA/cm²]	FF [%]	PCE [%]
With both methanol and DIO	0.78	17.7	63	8.7
With DIO no methanol	0.72	17.0	53	6.5
Without DIO and no methanol	0.42	13.7	54	3.1

Table 1. *Attributes of PSCs with different processing conditions.*

Table 1 above shows the specific *J-V* characteristics of solar cells with different processing conditions as shown in Fig. 2. Additives affect the morphology of the active layer. DIO slows down the evaporation of the solvent of the active layer [28] since it has a higher boiling point (333 ˚C) than 1, 2 DCB (174˚C). This results in more crystalline polymers [29] that have higher hole conductivity and mobility and hence higher current and PCE. Also, PCBM has higher solubility in the additive than in 1, 2 DCB [28] and this leads to the suppression of the formation of large PCBM aggregates [29] during drying of the active layer which enhance charge transport

in the active layer. Fig. 3 below shows the EQE spectra of solar cells with different processing conditions and is in agreement with the *J-V* characteristics shown in Fig. 2.

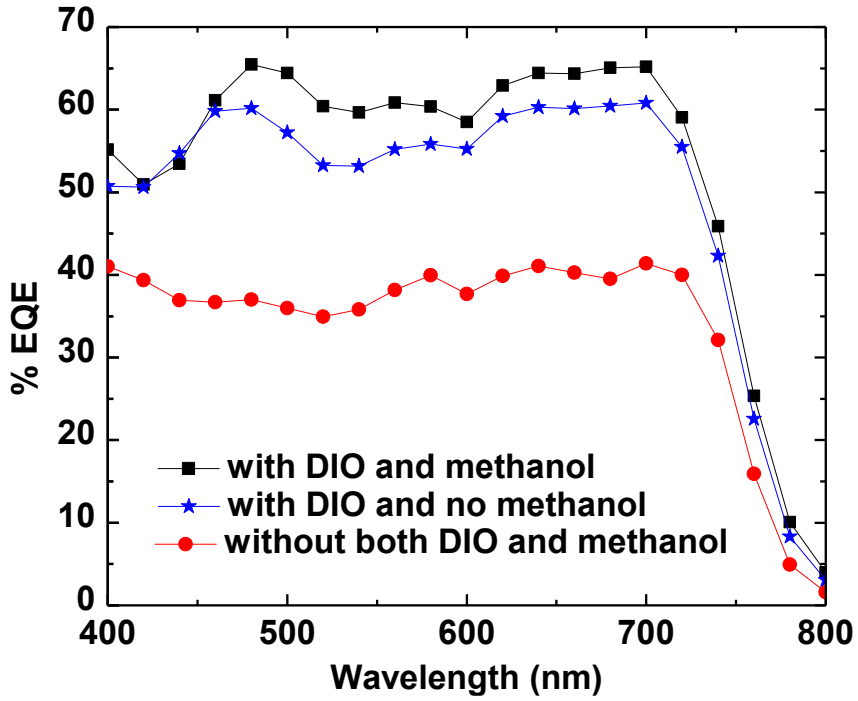

Fig. 3. *EQE spectra of solar cells with DIO added 20 mins prior to spin-coating and washed with methanol (black squares), DIO added 20 mins prior to spin-coating without methanol washing (blue stars) and DIO added 24 hours prior to spin-coating without methanol washing (red circles).*

Methanol washing enhances solar cells in a few ways. First it washes away residual DIO from the active layer [1,28,29]. Since DIO has a very high boiling point, the active layer dries too slowly and if contacts are deposited on an active layer that is not completely dry, the resulting solar cells have bad contacts and hence decreased charge carrier collection decreasing J_{sc} and PCE. Solar cells where DIO was not washed off were found to not be completely dry after one day [28]. Furthermore, methanol washing results in films that have an active layer gradient with a higher concentration of PCBM near the cathode and a higher concentration of the polymer towards the anode. This gradient increases both the charge carrier transport and

collection at the electrodes [28,29]. AFM images of the active layer washed with methanol (a) and without methanol washing (b) were taken. Fig. 4 below shows that methanol washing decreases the RMS roughness value of the films from 8.13 nm to 2.03 nm. This leads to better contact formation of the cathode for better collection of electrons enhancing the PCE.

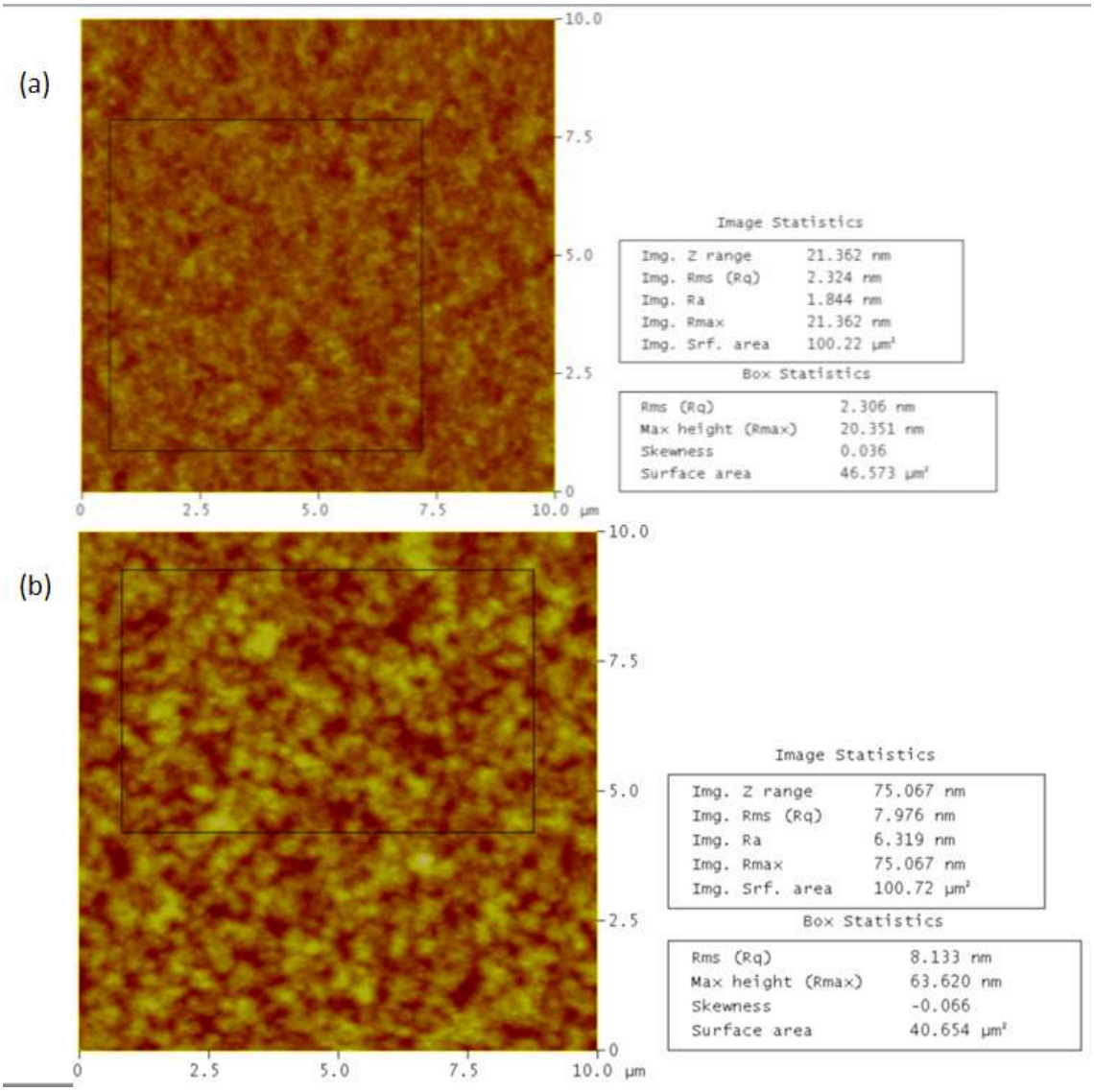

Fig. 4. *AFM images of ITO/PEDOT:PSS/PBDTTT-EFT:PCBM (a) after methanol washing and (b) without methanol washing.*

Methanol washing neither significantly changes the active layer thickness nor the absorption of light as shown in Fig. 5 below. Fig. 5 shows the absorption of light in ITO/PEDOT:

PSS/PBDTTT-EFT: PCBM film with and without methanol washing and the absorption properties do not change.

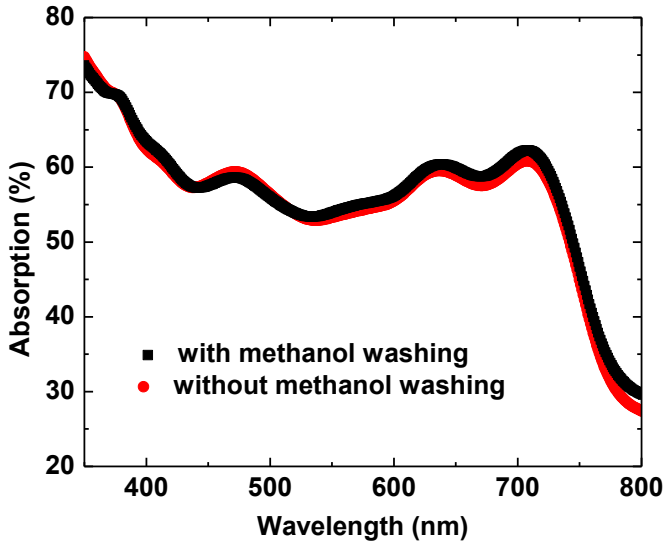

Fig. 5. *Absorption of ITO/PEDOT: PSS/PBDTTT-EFT: PCBM films with methanol washing and without methanol washing.*

4.3.2 Effect of photodegradation on PBDTTT-EFT polymer solar cells

4.3.2.1. J-V, absorption, and EQE

Typical *J-V* characteristics of a PSC before and following 24 h illumination in a nitrogen-filled glovebox are shown in Fig. 6 and the cell's-attributes are summarized in Table 2.

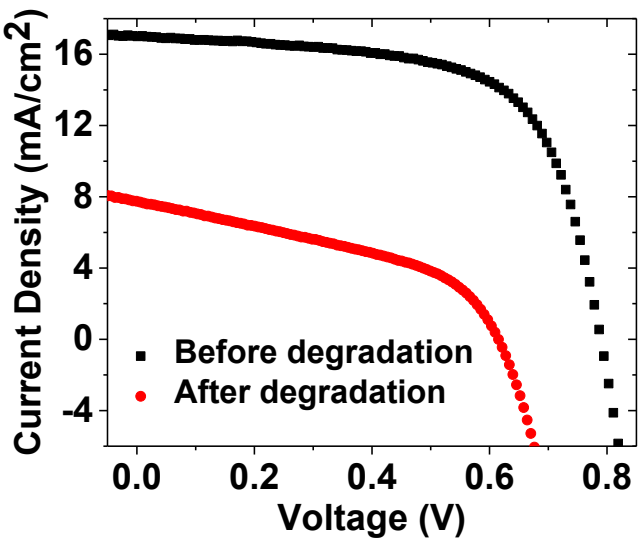

Fig. 6. *Light J-V characteristics of a PBDTTT-EFT solar cell before and after 24 h degradation by 1 sun intensity, 100 mW/cm², using a full solar spectrum simulator.*

Table 2. *Characteristics of a PBDTTT-EFT solar cell before and after 24 h of photodegradation. R_S is the series resistance.*

	V_{oc} [V]	J_{sc} [mA/cm²]	FF [%]	R_s (Ω)	R_{shunt} (kΩ)	PCE [%]
Before Degradation	0.79	17.0	65	54.6	9.9	8.7
After Degradation	0.61	7.7	42	150.3	3.0	2.0

Photodegradation resulted in an overall PCE decrease of ~77% from 8.7% to 2.0%. As shown in Table 2, the series resistance R_s increased and the shunt resistance R_{shunt} decreased significantly. Traps in the active layer can lead to an increase in R_s due to changes in the electric field in the active layer that result from accumulated charges. Defects can also create alternate current paths that lead to reduced R_{shunt} and reduced current flowing through the solar cell junction (hence lower J_{sc}) as well as reduced voltage, and thus reduced power output and PCE of the solar cell. Fig. 7 shows the normalized decrease of V_{oc}, FF, J_{sc}, and PCE during the 24 h

irradiation. The V_{oc} decreased to 77% of the initial value, *FF* to 65%, J_{sc} to 45%, and the PCE decreased to 23% of the initial value after 24 h.

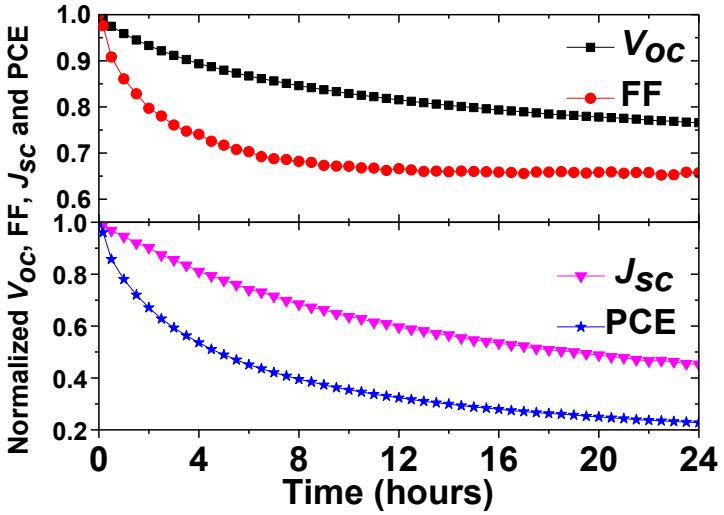

Fig. 7. *Normalized V_{oc}, FF, J_{sc}, and PCE of PBDTTT-EFT solar cells during photo-degradation at 1 sun intensity.*

The decrease in J_{sc} and PCE cannot be explained by a decrease in the absorption, which was not significant as shown in Fig. 8 (at any wavelength up to ~700 nm the decrease was less than 3.0%).

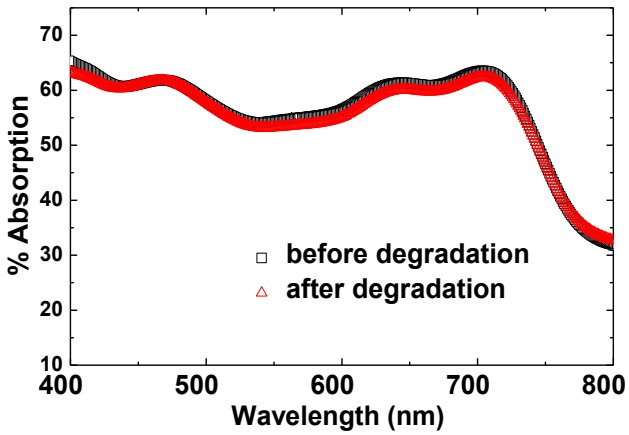

Fig. 8. *Absorption of ITO/PEDOT:PSS/ PBDTTT-EFT:$PC_{70}BM$ films before and after 24 h degradation under 100 mW/cm^2 1 sun irradiation.*

The degraded performance is not related to substantial morphological changes, as atomic force microscopy (AFM) of degraded and as-prepared films showed no difference in the surface structure, hence photodegradation did not lead to significant polymer aggregation. Indeed, the

respective root mean square surface roughness values before and after degradation were 1.12 and 1.17 nm, respectively. Dark *J-V* gives important information about the recombination in the device through analysis of ideality factors and saturation currents. Excluding the effects of series resistance, the dark J-V relationship of a PSC follows the equation [30]:

$$J = J_{01}\left[\exp\left(\frac{V}{n_1 kT}\right) - 1\right] + J_{02}\left[\exp\left(\frac{V}{n_2 kT}\right) - 1\right] + \frac{V}{AR_{SH}} \qquad (4.1)$$

Where J_{01} and J_{02} are saturation current densities, n_1 and n_2 are ideality factors, A is the pixel area, k is Boltzmann constant and T is the temperature in kelvin and V is the applied voltage. By fitting equation 4.1 to experimental data, the ideality factors and saturation currents can be obtained. Shunt current (J_{SH}) obscures the dark *J-V* characteristics and has to be subtracted before analysis. After subtracting J_{SH}, the exponential part of equation 4.1 is fitted to experimental data. Fig. 9(a) shows the dark *J-V* characteristics of PBDTTTT-EFT PSCs and Fig 9(b) shows the fitting of the exponential part of the forward dark *J-V* after subtracting J_{SH}.

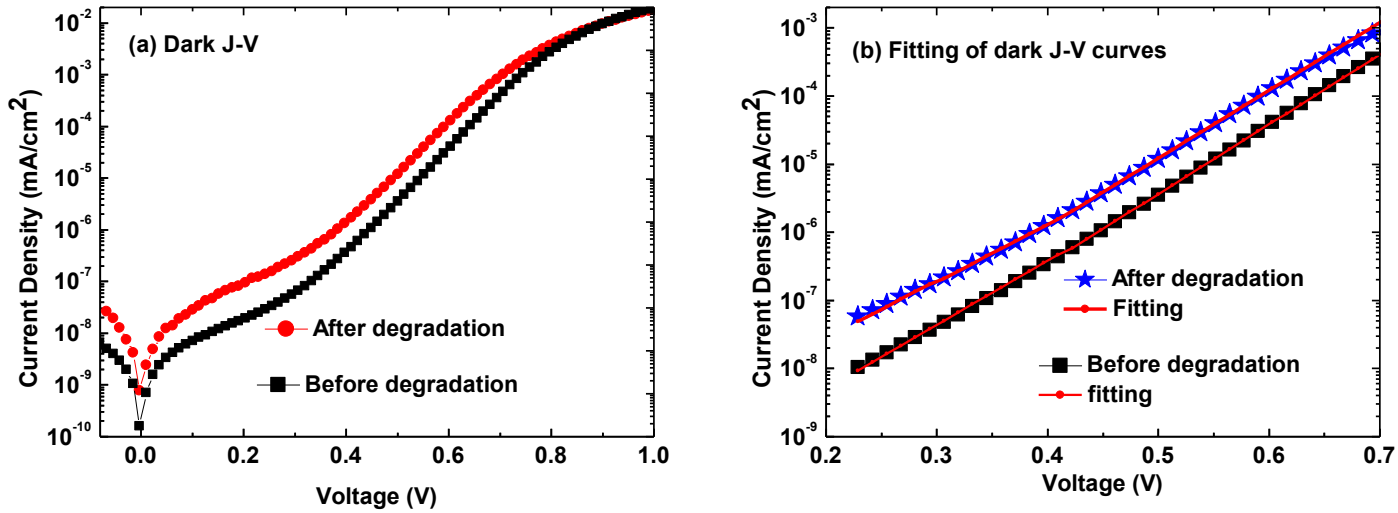

Fig. 9. *(a) Dark J-V characteristics of a PBDTTT-EFT solar cell and before and after 24 h degradation by 1 sun intensity. (b) Forward dark J-V characteristics after subtracting shunt and the respective fitting of the exponential part of Eq.4.1 to the experimental data.*

Fig. 9 (a) shows an increase in shunt resistance due to photodegradation and a change in the exponential characteristics of the PSCs. The best fit of the exponential region of the dark *J-V* curve from equation 4.1 of experimental data after subtracting shunt current is shown in Table 3.

Table 3. *Dark J-V characteristics of PBDTTT-EFT SCs before and after 24 h of photodegradation.*

	n_1	J_{01} ($\frac{mA}{cm^2}$)	n_2	J_{02} ($\frac{mA}{cm^2}$)
Before degradation	1.77	6.6×10^{-11}	1.63	2.8×10^{-11}
After degradation	1.97	5.3×10^{-10}	1.68	1.3×10^{-10}

n_1 increases from 1.77 to 1.97 which indicates an increase in recombination due to deep traps at the D/A interface [31]. An increase in J_{01} by a factor of 8 from 6.6×10^{-11} $\frac{mA}{cm^2}$ to 5.3×10^{-10} $\frac{mA}{cm^2}$ is due to an increase in recombination due to mid-gap trap density at the D/A interface [20], which in turn leads to the observed reduction in V_{oc} according to equation 4.2 [20];

$$V_{oc} = (\frac{nkT}{q})\ln(\frac{I_{sc}}{I_{01}}) \qquad (4.2)$$

The increase in n_2 is not significant. The high value of n_2 indicates that recombination is highly due to mid-gap trap density at the D/A interface though there would be contributions from recombination due to tail states in the polymer. An increase by a factor of 4.6 in J_{02} from 2.8×10^{-11} $\frac{mA}{cm^2}$ to 1.3×10^{-10} $\frac{mA}{cm^2}$ indicates an increase recombination which may be partially due to an increase in polymer tail states in the PSCs [32]. The increase in recombination leads to a decrease in charge carrier collection of PSCs, supported by the fact that there is a stronger decrease in J_{sc} in comparison to the decrease in the absorption. Fig. 10 shows the EQE spectra before and after degradation.

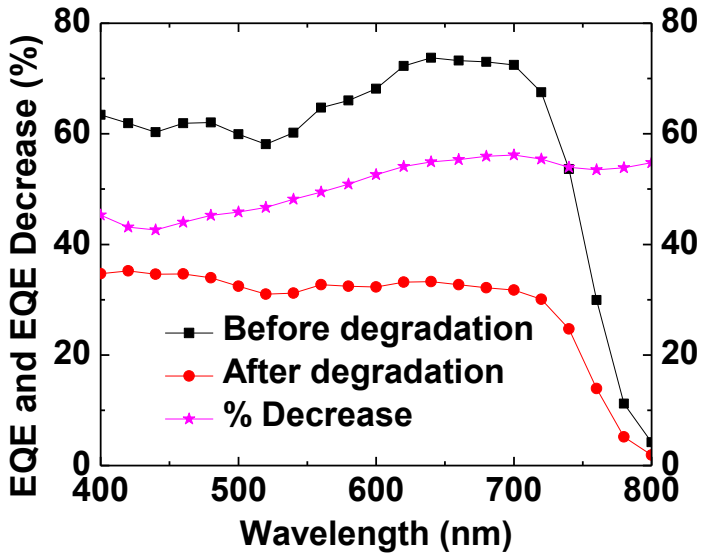

Fig. 10. *EQE characteristics of a PBDTTT-EFT solar cell before and after degradation under 100 mW/cm² 1 sun irradiation for 24 h.*

As expected, the EQE decreased after degradation; the decrease was ~45% to 56% across the measured wavelength range, indicating a significant contribution of decreased charge collection to the decreased cell performance. To further investigate charge extraction in the PSCs, EQE measurements with and without bias for as-prepared and photodegraded devices were compared in Fig. 11.

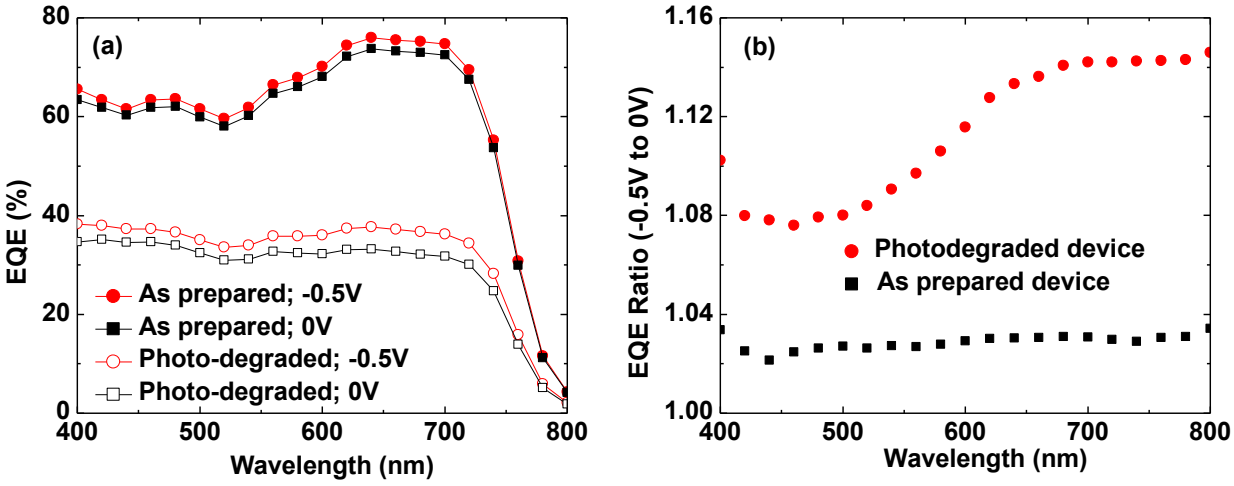

Fig. 11. *(a) EQE characteristics of as-prepared and degraded PSCs at 0 V and -0.5 V bias. (b) The EQE ratios of these solar cells.*

As seen, biasing increases the EQE and the ratio between biased (-0.5 V) and unbiased EQE, in particular in the degraded device, which indicates that charge extraction is reduced in the degraded cells [33]. Charge collection is affected by charge mobility, hence, hole mobility in PBDTTT-EFT films was measured as a function of degradation time.

4.3.2.2. Space-charge limited current (SCLC) hole mobility measurements

We investigated the hole mobility in hole-only devices with the structure ITO/PEDOT:PSS/ PBDTTT:EFT/Au. Fig. 12 shows the change in hole mobility due to light degradation.

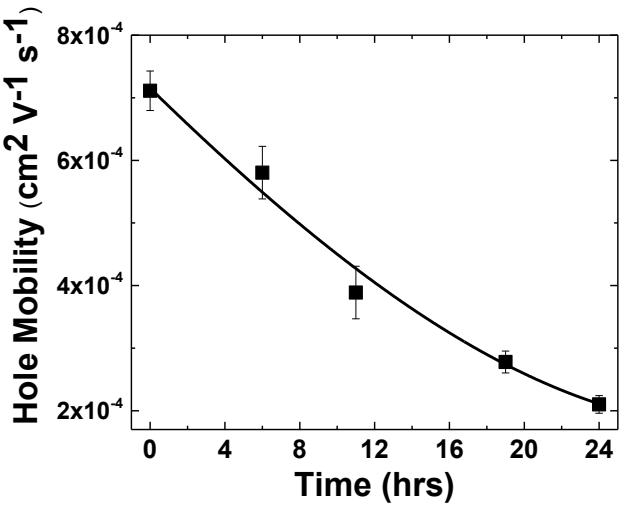

Fig. 12. *Change in hole mobility in PBDTTT-EFT over 24 hours of light exposure. The line is to guide the eye.*

In semiconductors and insulators, SCLC occurs when the number of injected carriers exceeds the number of traps in the sample. Beyond the trap-filled limit voltage, injected charges are free to move and the current density is given by [34]

$$J = \frac{9}{8}\varepsilon_0\varepsilon_r\mu\frac{V^2}{t^3} \qquad (4.3)$$

Where ε_0 is the vacuum permittivity, ε_r is the dielectric constant of the film, t is the thickness of the active layer, μ is the mobility, J is the applied current density, and V is the measured voltage. From Eq. (4.2), the mobility can be calculated from the slope of a J vs V^2 plot. The values used were $\varepsilon_r = 3$ [25], t = 160 nm as measured, and $\varepsilon_0 = 8.854 \times 10^{-12}$ F/m [34]. The hole mobility degraded from 7.2×10^{-4} to 2.2×10^{-4} cm²/Vs, which is 30% of the initial value over 24 hours, as shown in Fig. 11. We note that the initial hole mobility is comparable to values reported for other PBDTTT polymers with a film of polymer/acceptor blend showing a reduced mobility of 3.5×10^{-4} cm²/Vs [2,23]. The decrease in the mobility following light exposure is likely related to a reduction in charge collection associated with increased trap density. To investigate deep

defects, a capacitance-frequency C(*f*) technique to obtain the density of states (DOS) and a subgap QE measurement [20,35-38] were employed, as described next.

4.3.2.3. Density of States

DOS measurements were performed to analyze defect states in the solar cells. Fig. 13(a) shows the gap defect densities in the BHJ cell before and after photodegradation as a function of energy with respect to the HOMO level of PBDTTT-EFT, $E - E_{HOMO}$. Figs. 13(b) and 13(c) show the DOS of devices with one component only, whether the polymer or the acceptor, to identify the site of the increased defect density in the solar cells. The figures were obtained from C(*V*) and C(*f*) measurements described in detail by Boix et al [37]. The initial defects in the PSC may be due to chemical impurities introduced during material synthesis and device fabrication, as well as exposure to the very small amounts of oxygen and moisture in the glovebox. After exposure to light, the defect density increased by a factor >5 for $E - E_{HOMO} > 0.4$ eV. The largest increase (a factor of 13) was in the range of 0.6 to 0.65 eV above the HOMO of PBDTTT-EFT, which is energetically in the middle of the interface between PBDTTT-EFT and PCBM. The DOS of the donor- and acceptor-only devices in the energy range shown (Figs 13(b) and 13(c)) was largely unchanged, indicating that these defects states are located at the donor/acceptor (D/A) interface. Based on the unchanged absorption spectrum (Fig. 8) and AFM images following irradiation, the DOS increase is not related to a significant change in the materials' bulk properties following irradiation. Hydrogen-related defects, e.g., C-H bond straining/rearrangement in the polymer [21,31,39,40], possibly at the D/A interface, may

contribute to this DOS increase, though the increase was irreversible, as heating further degraded the devices.

Fig. 13. *Density of states (DOS) of gap defects in (a) PBDTTT-EFT:PCBM solar cells and (b) PBDTTT-EFT only device as a function of energy with respect to the PBDTTT-EFT HOMO level. (c) DOS of a PCBM only device as a function of energy with respect to the PCBM HOMO level.*

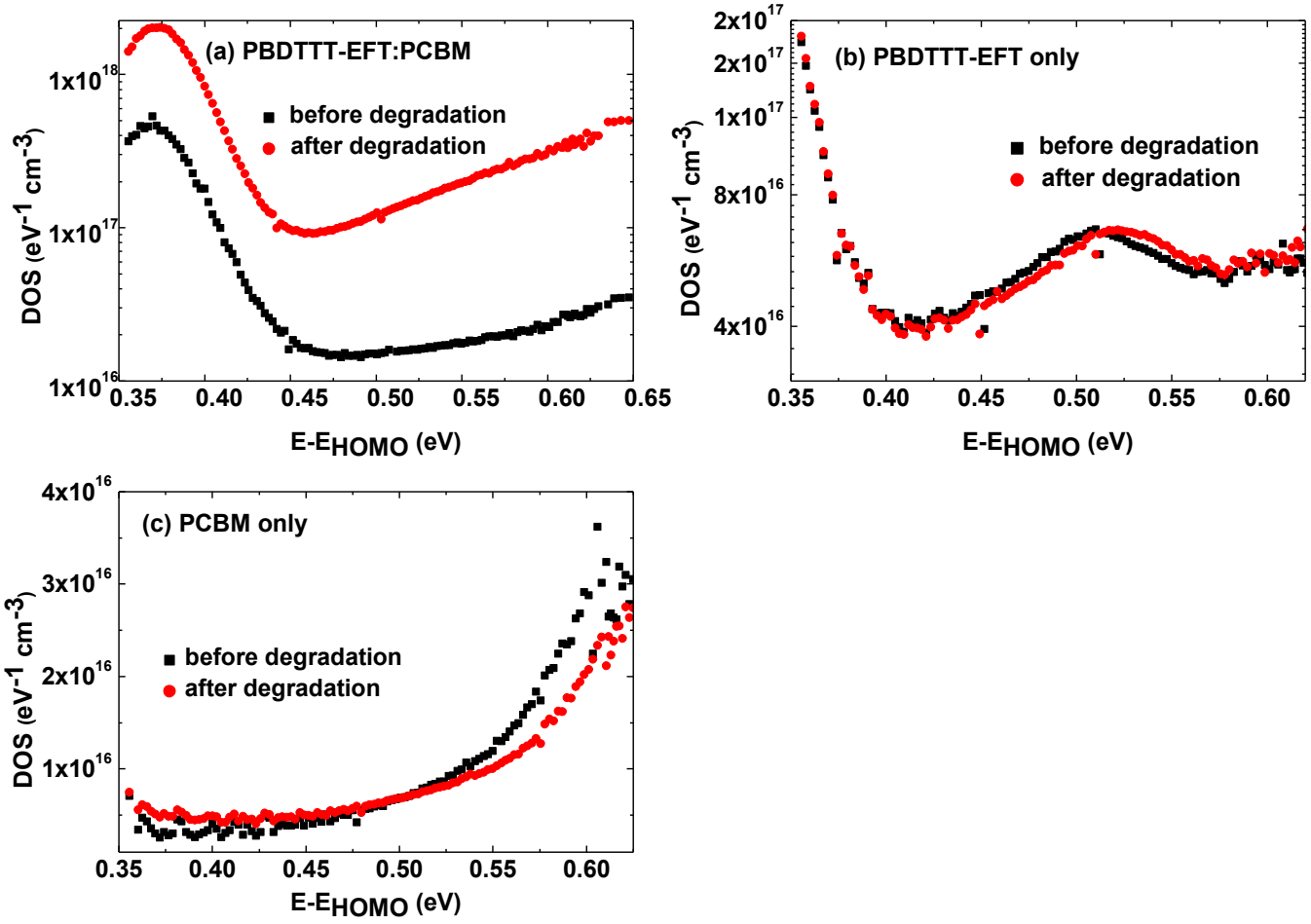

4.3.2.4. Subgap Quantum Efficiency

Fig. 14(a) shows the subgap QE of the solar cell and of a polymer-only device, i.e., without the fullerene. As seen, the measurements show an increase in the defect state density in the PBDTTT-EFT polymer close to its midgap at an incident energy in the range of ~0.83 to 1.1 eV, following photodegradation. For the BHJ cell, at 1.1 eV the increase is 2×; it is 6× at 0.87 eV.

For the polymer only device, the increase is 1.3× and 3× at 1.1 eV and 0.87 eV respectively. Fig. 14(b) shows the energy levels of the D/A BHJ cell with the various possible optical transitions, labeled (*a*)–(*d*). The energy region higher than 1.6 eV, i.e., higher than the bandgap of PBDTTT-EFT, corresponds to transition (*a*), which is the bulk absorption by the polymer [41]. At an energy < 1.6 eV there is a rapid decrease in the QE with a small increase in the slope in the range ~1.2 to ~1.4 eV in the BHJ structure, but a reduced slope in the device with the polymer only. Arrow (*b*), representing the

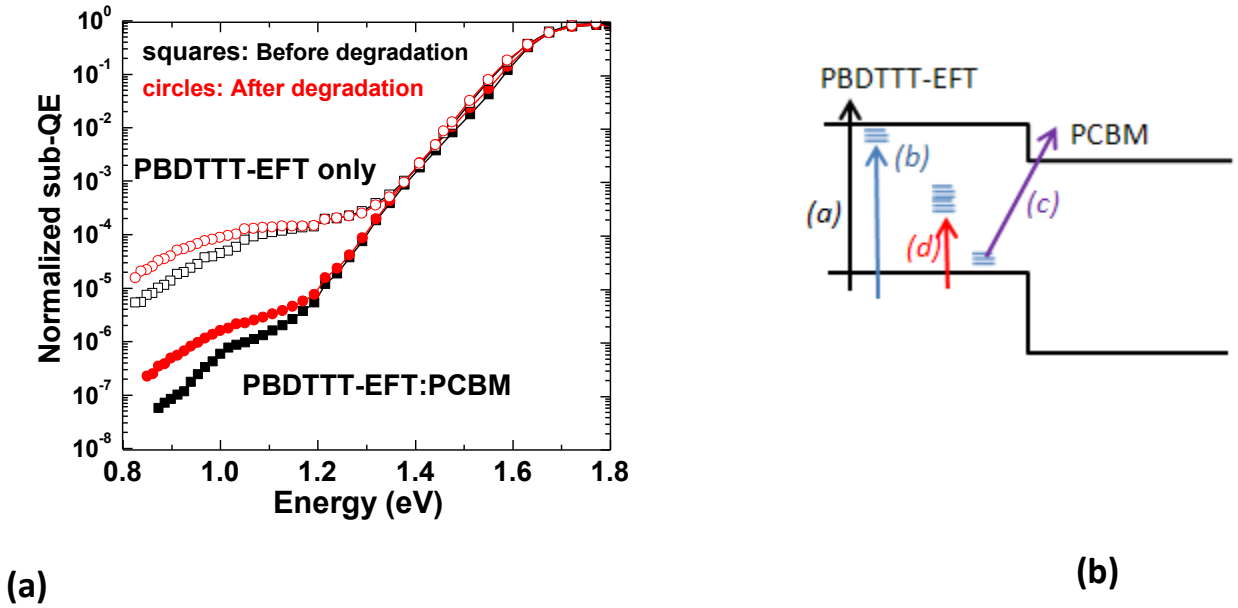

Fig. 14. *(a) Normalized subgap QE before and after light degradation of the BHJ solar cell and the polymer-only device. (b) Schematic energy diagram showing optical transitions in the solar cell.*

energy range from >1.4 eV to 1.6 eV, corresponds to excitations from the HOMO and HOMO tail states of PBDTTT-EFT to empty tail states near its LUMO level [38]. Transition (*c*) corresponds to the energy range ~ 1.2 to 1.4 eV; it represents transitions from the tail states near the HOMO of PBDTTT-EFT to the LUMO level of $PC_{70}BM$ [38,41]; this transition is not seen

in the polymer-only device (Fig. 14(a)). At energies < 1.2 eV the transitions are from the polymer's HOMO to deep traps in PBDTTT-EFT [38] as shown by arrow (*d*). Structural disorder in heterojunction donor-acceptor solar cells for both polymers [38,41 ,42] and small molecule-based devices [43] results in Urbach tail states within the bandgap. The calculated Urbach energies from the subgap QE measurements for tail states near the LUMO and HOMO levels of PBDTTT-EFT are ~43 and ~35 meV, respectively. Fig. 15 shows the non-normalized subgap QE of the BHJ SC and polymer-only device.

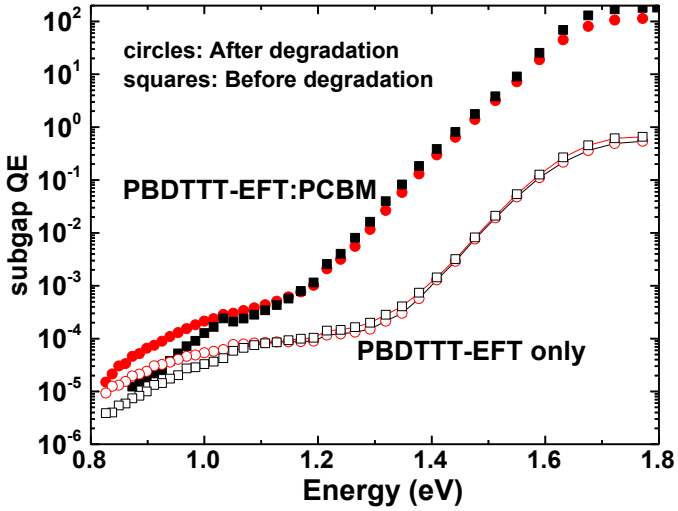

Fig. 15. *(a) Subgap QE before and after light degradation of the BHJ solar cell and the polymer-only device (without normalization).*

The initial low subgap QE in the polymer-only devices is due to the very low level (~2%) of singlet exciton (SE) dissociation [44] in such films, as compared to the massive dissociation of such SEs in the BHJ SCs. The presence of deep traps in PBDTTT-EFT allows transitions of electrons and holes from these trap states to conducting states leading to an increase in subgap QE after photodegradation [31].

4.3.2.5 Effect of UV and blue light

To better understand the origin of the photodegradation, we also used 495 and 455 nm long pass filter to assess the effect of high energy photons on the PSCs' degradation. The light intensity, measured with a reference, was kept constant in all measurements. Figs. 16(a) and (b) show the *J-V* characteristics of typical PSCs with 495 and 455 nm long pass filters, respectively, before and following 24 h irradiation in a nitrogen-filled glovebox. The cells' attributes are summarized in Table 4. Figs. 16(c) and (d) show normalized V_{oc}, *FF*, J_{sc}, and PCE of PBDTTT-EFT solar cells during degradation at 1 sun intensity with 495 and 455 nm long pass filters. As seen in Fig 16 and Table 4, the decreases in all attributes when using these optical filters are very small. Photodegradation with the use of the 495 nm long-pass filter resulted in an overall PCE decrease of only ~3.6%, from 8.3% to 8.0 %. Hence, light of > 495 nm does not contribute strongly to the observed degradation due to 24 h irradiation. To investigate whether 495 – 455 nm light causes significant degradation, a 455 nm long-pass filter was also used and the degradation of the PSCs was monitored. Photodegradation with the 455 nm long-pass filter resulted in an overall PCE decrease of ~ 6.0 % from 8.7% to 8.2. Overall, filtering out light below 455 nm significantly reduces the short-term instability of the PSCs.

Fig. 16. *J-V characteristics of PBDTTT-EFT solar cells before and after 24 h degradation by 1 sun intensity with (a) 495 nm and (b) 455 nm long pass filters, and normalized Voc, FF, Jsc, and PCE of PBDTTT-EFT solar cells during degradation at 1 sun intensity with (c) a 495 nm filter and (d) a 455 nm long pass filter.*

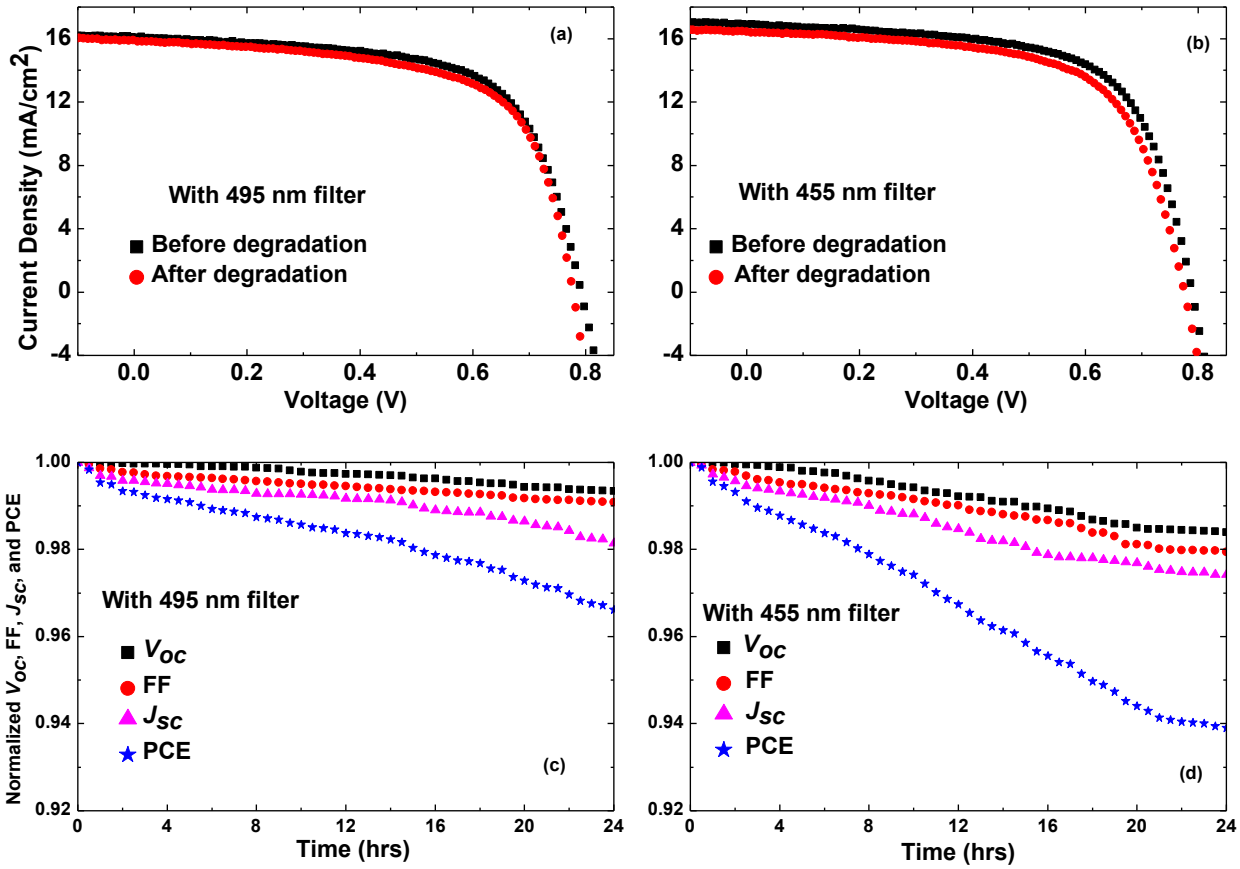

Table 4. *Characteristics of PBDTTT-EFT:$PC_{70}BM$ solar cells before and after 24 h of photodegradation with 495 nm and 455 nm long pass filters.*

		V_{oc} [V]	J_{sc} [mA/cm²]	FF [%]	PCE [%]
495 nm filter	Before Degradation	0.79	16.1	65.1	8.3
	After Degradation	0.78	15.9	64.5	8.0
455 nm filter	Before Degradation	0.79	16.9	65.3	8.7
	After Degradation	0.78	16.4	64.1	8.2

4.4. Conclusions

Our results demonstrate that UV and blue light at wavelengths < 455 nm are largely responsible for the short-term photodegradation of PBDTTT-EFT:$PC_{70}BM$ solar cells. The electronic measurements provided the density of trapping states throughout the gap. Exposure of PBDTTT-EFT:PCBM solar cells to light results in a change in the fundamental properties of the PSCs: Density-of-states (DOS) measurements showed a significant increase in midgap states at the interface between PBDTTT-EFT and PCBM (~0.55–0.65 eV above the polymer's HOMO level). This increased DOS leads to increased charge trapping and recombination, reducing carrier collection efficiency at the electrodes, and hence resulting in a decrease in J_{sc}, *FF*, hole mobility, and the PCE. Moreover, an increase in recombination at the D/A interface results in the reduction of the $V_{oc.}$ An increase in deep defect states in the polymer (at incident energies in the range of 0.83 to 1.1 eV) was observed in subgap QE measurements. Using optical filters to cut the UV and deep blue light < 455 nm greatly improves the short-term stability of the solar cells. Thus, the results demonstrate that this short wavelength light is the main source of the observed degradation in PBDTTT-EFT PSCs.

References

[1] Z. Shaoqing, Y. Long, Z. Wenchao, L. Delong, Y. Huifeng, H. Jianhui, Macromolecules 47 (2014) 4653.

[2] H. Y. Chen, J. Hou, S. Zhang, Y. Liang, G. Yang, Y. Yang, L. Yu, Y. Wu, G. Li,. Nat. Photon. 3 (2009) 649.

[3] X. Fan, G. Fang, F. Cheng, P. Qin, H. Huang Y. Li, J. Phys. D: Appl. Phys. 46 (2013) 305106.

[4] D. Wang, F. Zhang, L. Li, J. Yu, J. Wang, Q. An, W. Tang, RSC Adv. 4 (2014) 48724.

[5] T. Y. Chu, J. Lu, S. Beaupré, Y. Zhang, J. R. Pouliot, S. Wakim, J. Zhou, M. Leclerc, Z. Li, J. Ding, Y. Tao, J. Am. Chem. Soc. 133 (2011) 4250.

[6] L. Dou, J. You, J. Yang, C. C. Chen, Y. He, S. Murase, T. Moriarty, K. Emery, G. Li, Y. Yang, Nat. Photon. 6 (2012) 180.

[7] J. Peet, J. Y. Kim, N. E. Coates, W. L. Ma, D. Moses, A. J. Heeger, G. C. Bazan, Nat. Mater. 6 (2007) 497.

[8] Y. Liang, Z. Xu, J. Xia, S. T. Tsai, Y. Wu, G. Li, C. Ray, L. Yu, Adv. Mater. 22 (2010) E135.

[9] Z. He, C. Zhong, S. Su, M. Xu, H. Wu, Y. Cao, Nat. Photon. 6 (2012) 591.

[10] Z. He, C. Zhong, X. Huang, W. Y. Wong, H. Wu, L. Chen, S. Su, Y. Cao, Adv. Mater. 23 (2011) 4636.

[11] G. Li, V. Shrotriya, Y. Yao, Y. Yang, J. Appl. Phys. 98 (2005) 043704.

[12] G. Li, V. Shrotriya, J. Huang, Y. Yao, T. Moriarty, K. Emery, Y. Yang, Nat. Mater. 4 (2005) 864.

[13] F. Zhang, K. G. Jespersen, C. Bjorstrom, M. Svensson, M. R. Andersson, V. Sundstrom, K. Magnusson, E. Moons, A. Yartsev, O. Inganas, Adv. Funct. Mater. 16 (2006) 667.

[14] F. C. Krebs, K. Norrman, Prog. Photovolt: Res. Appl. 15 (2007) 697.

[15] A. Rivaton, S. Chambon, M. Manceau, J.-L. Gardette, N. Lemaitre, S. Guillerez,. Polym. Degrad. Stab. 95 (2010) 278.

[16] M. O. Reese, A. J. Morfa, M. S. White, N. Kopidakis, S. E. Shaheen, G. Rumbles, D. S. Ginley, Sol. Energy Mater. Sol. Cells 92 (2008) 746.

[17] K. Kawano, R. Pacios, D. Poplavskyy, J. Nelson, D. D. C. Bradley, J. R. Durrant, Sol. Energy Mater. Sol. Cells. 90 (2006) 3520.

[18] M. Jørgensen, K. Norrman, F. C. Krebs, Sol. Energy Mater. Sol. Cells 92 (2008) 686.

[19] K. Kawano, C. Adachi, Appl. Phys. Lett. 96 (2010) 053307.

[20] J. Bhattacharya, R. W. Mayer, M. Samiee, V. L. Dalal, Appl. Phys. Lett. 100 (2012) 193501.

[21] R. A. Street, D. M. Davies, Appl. Phys. Lett. 102 (2013) 043305.

[22] T. Endale, E. Sovernigo, A. Radivo, S. D. Zilio, A. Pozzato, T. Yohannes, L. Vaccari, M. Tormen, Sol. Energy Mater. Sol. Cells 123 (2014) 150.

[23] D. Mori, H. Benten, I. Okada, H. Ohkita, S. Ito, Energy Environ. Sci. 7 (2014) 2939.

[24] P. Adhikary, S. Venkatesan, N. Adhikari, P. P. Maharjan, O. Adebanjo, J. Chenb, Q. Qiao, Nanoscale 5 (2013) 10007.

[25] E-P. Yao, Y-J. Tsai, W-C. Hsu, Int. J. Photoenergy 2014 (2014) 952528.

[26] T. Xiao, W. Cui, J. Anderegg, J. Shinar, R. Shinar, Org. Electron. 12 (2011) 257.

[27] G. Cumming, F. Fidler, D. L Vaux, JCB. 177 (2007) 7.

[28] Z. Xiao, Y. Yuan, B. Yang, J. VanDerslice, J. Chen, O. Dyck, G. Duscher, J. Huang, Adv. Mater. 26 (2014) 3068.

[29] W. Huang, E. Gann, L. Thomsen, C. Dong, Y-B. Cheng, C. R. McNeill, Adv. Energy Mater. 5 (2015) 1401259.

[30] O. Breitenstein, J. Bauer, P. P. Altermatt, K. Ramspeck, Solid State Phenomena Vols. 156-158 (2010) 1.

[31] R. A. Street, J. E. Northrup, B. S. Krusor, Phys. Rev. B 85 (2012) 205211.

[32] S. A. Hawks, G. Li, Y. Yang, R. A. Street, J. Appl. Phys. 116 (2014) 074503.

[33] T. Xiao, F. Fungura, M. Cai, J. W. Anderegg, J. Shinar, R. Shinar, Org. Electron. 14 (2013) 2555.

[34] T. Endale, E. Sovernigo, A. Radivo, S. D. Zilio, A. Pozzato, T. Yohannes, L. Vaccari, M. Tormen, Sol. Energy Mater. Sol. Cells 123 (2014) 150.

[35] M. Samiee, B. Modtland, D. Aidarkhanov, V. L. Dalal, Appl. Phys. Lett. 104 (2014) 213909.

[36] G. Garcia-Belmonte, P. P. Boix, J. Bisquert, M. Lenes, H. J. Bolink, A. L. Rosa, S. Filippone, N. Martin, J. Phys. Chem. Lett. 1 (2010) 2566.

[37] P. P. Boix, G. Garcia-Belmonte, U. Munecas, M. Neophytou, C. Waldauf, R. Pacios, Appl. Phys. Lett. 95 (2009) 233302.

[38] M. Samiee, P. Joshi, D. Aidarkhanov, V. Dalal, Appl. Phys. Lett. 105 (2014) 133511.

[39] S. Shah, R. Biswas, J. Phys. Chem. C 119 (2015) 20265.

[40] R. A. Street, J. E. Northrup, B. S. Krusor, Phys. Rev. B 85 (2012) 205211.

[41] R. A. Street, A. Krakaris, S. R. Cowan, Adv. Funct. Mater. 22 (2012) 4608.

[42] R. A. Street, K. W. Song, J. E. Northrup, S Cowan, Phys. Rev. B 83 (2011) 165207.

[43] B. Song, C. Rolin, J. D. Zimmerman, S. R. Forrest, Adv. Mater. 26 (2014) 2914-2918.

[44] J. Partee, E. L. Frankevich, B. Uhlhorn, J. Shinar, Y. Ding, T. J. Barton, Phys. Rev. Lett. 82 (1999) 3673.

Chapter 5: Electron Paramagnetic Resonance evidence of carbon dangling bonds in photodegraded polymer:fullerene solar cells

Fadzai Fungura, William R. Lindemann, Joseph Shinar*, and Ruth Shinar*

Abstract

Intrinsic photodegradation of organic solar cells, theoretically attributed to C-H bond rearrangement/breaking, remains a key commercialization barrier. This work presents, via dark electron paramagnetic resonance (EPR), the first experimental evidence for metastable C dangling bonds (DBs) (g=2.0029±0.0004) formed by blue/UV irradiation of polymer:fullerene blend films in nitrogen. The DB density increased with irradiation and decreased ~4 fold after 2 weeks in the dark. The dark EPR also showed increased densities of other spin-active sites in photodegraded polymer, fullerene, and polymer:fullerene blend films, consistent with broad electronic measurements of fundamental properties, including defect/gap state densities. The EPR enabled identification of defect states, whether in the polymer, fullerene, or at the donor/acceptor (D/A) interface. Importantly, the EPR results indicate that the DBs are at the D/A interface, as they were present only in the blend films. The role of polarons in interface DB formation is also discussed.

5.1 Introduction

Polymer solar cells (PSCs) consisting of semiconducting polymer as an electron donor and fullerenes as electron acceptors are drawing a lot of attention because of their potential as a low cost, light weight and flexible source of energy. Significant improvement in power conversion efficiency (PCE) has been achieved [1-13] up to PCEs greater than 10% due to the use of low band-gap polymers [14-16]. PSC degradation is the main commercialization obstacle. Hence, extensive efforts are directed at understanding PSC degradation [17-28] when exposed to moisture and oxygen [17-20] as well as light [21-25]. The microscopic nature of the generated defects has not been revealed. This work demonstrates, for the first time, UV/blue photogeneration of metastable carbon dangling bonds (DBs, i.e., 3-fold coordinated C atoms) akin to the well-known Si DBs that pervade hydrogenated amorphous Si (a-Si:H) [29]. The C DBs are revealed via the electron paramagnetic resonance (EPR) of their unpaired spin 1/2 electron after observing the signature EPR of C DBs at $g = 2.0029 \pm 0.0004$ [30-34] in polymer:fullerene films. Importantly, at room temperature the DBs decay slowly in the dark, in sharp contrast to their stability in a-Si:H [29]. However, since the performance of the solar cells does not recover, it is suspected that the C DBs are passivated by, e.g., O- or OH-related groups, rather than the polymer recovering its original configuration. The study focuses on a low-bandgap polymer poly[4,8-bis(5-(2-ethylhexyl)thiophen-2-yl)benzo[1,2-b;4,5-b']dithiophene-2,6-diyl-alt-(4-(2-ethylhexyl)-3-fluorothieno[3,4-b]thiophene-)-2-carboxylate-2-6-diyl)] (PBDTTT-EFT) shown in Fig. 1. Electronic measurements of PBDTTT-EFT: $PC_{70}BM$ ((phenyl-C_{70}-butyric-acid-methyl ester) bulk heterojunction (BHJ) PSCs were done (Chapter 4). They demonstrated that UV and blue light at wavelengths < 455 nm are largely responsible for the short-term photodegradation of PBDTTT-EFT: $PC_{70}BM$ solar cells. Exposure of PBDTTT-

EFT:PCBM solar cells to light resulted in a change in the fundamental properties of the PSCs: Density-of-states (DOS) measurements showed a significant increase in midgap states at the interface between PBDTTT-EFT and PCBM (~0.55–0.65 eV above the polymer's HOMO level). An increase in deep defect states in the polymer (at incident energies in the range of 0.87 to 1.1 eV) was observed in subgap QE measurements. Use of optical filters to cut the UV and deep blue light < 455 nm greatly improved the short-term stability of the solar cells demonstrating that this short wavelength light is the main source of the observed photodegradation. The increase in defect states was accompanied by a decrease in PSCs' J_{sc}, V_{oc} *FF*, hole mobility, and PCE. In previous work, photodegradation was attributed to C-H bond straining and/or breaking [24,35-37]. Formation of dangling bonds, however, has so far not been demonstrated experimentally.

It is difficult to see how visible or near UV photons would have sufficient energy (>4 eV) to cause C-H bond breaking [24,35]; however, such bond breaking or rearrangement becomes much more plausible when induced by hot polarons. The latter may be energized by (i) direct blue/UV photon absorption, e.g., from the fullerene LUMO, or by (ii) annihilating an exciton by absorbing its energy [24,35]. Since the polaron density is much higher in the polymer:fullerene blends than in polymer-only films, the C DBs are observed only in the former, as demonstrated next by EPR, which shows, *for the first time*, the likely presence of C DBs in photodegraded polymer:fullerene blends but not in polymer-only films.

Hot polaron formation via exciton annihilation [38-40] is unlikely. Although triplet-polaron annihilation was previously invoked to explain degradation of blue phosphorescent OLEDs [41], in BHJ PSCs fast exciton dissociation and/or thermalization to the fullerene's LUMO likely exclude this scenario.

Continuous wave (CW) dark and light-induced electron paramagnetic resonance (EPR) measurements were performed on PBDTTT-EFT, $PC_{70}BM$, and PBDTTT-EFT:$PC_{70}BM$ films to analyze defect formation at the atomic scale, charge generation, and trapping in the films, and to identify the role of each component and the donor/acceptor (D/A) interface in the photo-induced defect generation process. The dark EPR results indicate irradiation-induced formation of C dangling bonds in blend films, reminiscent of the formation of Si dangling bonds in hydrogenated amorphous Si due to the Staebler-Wronski Effect [29], and are compared to the electronic measurements. These defects, in agreement with the electronic measurements, are formed at the D/A interface, as they are not observed in polymer only films.

5.2. Experimental

5.2.1. Materials and solutions

PBDTTT-EFT was obtained from Solarmer Materials (Beijing) Inc. and $PC_{70}BM$ from Solaris Chem Inc. Both materials were used with no further purification. A solution of 1:1.5 weight ratio of PBDTTT-EFT:$PC_{70}BM$ in 1,2- dichlorobenzene (DCB) purchased from Sigma Aldrich, with a concentration ratio of 10:15 mg/mL was used. The PBDTTT-EFT solution was filtered using a 0.22 μm Millex PTFE filter before mixing with $PC_{70}BM$. The mixture was stirred for 24 h on a hot plate at a temperature of 70°C before spin-coating. 1,8 diiodooctane (DIO) additive was purchased from sigma Aldrich.

5.2.2. Device fabrication

PBDTTT-EFT, PCBM and PBDTTT-EFT:PCBM blend films were fabricated by spin-coating the respective solutions on polyethylene terephthalate (PET) films. 1 inch × 1 inch PET films were cleaned with a surfactant for 15 min. Next, the substrates were placed under running deionized water for 15 min, followed by sonication in isopropanol and then in acetone and again

in isopropanol for 5 min for each step. 3 % vol diiodooctane (DIO) was added to PBDTTT-EFT and PBDTTT-EFT:$PC_{70}BM$ mixtures and the solutions were spin-coated at 500 rpm in the glovebox. Next, 65 μL of methanol were spin-coated on top of the active layer at 4000 rpm [1]. The films were dried under a petri dish. For packing the films in EPR quartz tubes, they were first cut into small strips and packed into the tubes.

5.2.3. Device characterization

For photodegradation studies, films were exposed to 100 mW/cm^2 (1 sun) full solar simulator spectrum for various (0, 8, 16 and 24) hours using a xenon source solar simulator with appropriate filters to simulate AM1.5 sunlight. The films were kept in a nitrogen-filled glovebox during the course of the degradation measurements and they were cooled by a fan during irradiation. CW EPR experiments were performed on films of PBDTTT-EFT, $PC_{70}BM$, and PBDTTT-EFT:$PC_{70}BM$ blends, all fabricated in a N_2-filled glovebox. The films were placed in a sealed N_2 filled quartz tube within the resonator without exposure to air. X-band (9.9 GHz) EPR experiments were carried out with a Bruker ELEXSYS E580 EPR spectrometer before and after sample photodegradation. Experiments were conducted in the dark and under illumination with an incident ELH light intensity of 70 mW; illumination lasted for about 8 min. When using the lamp, a water filter (20 cm path-length) was used to avoid unwanted sample heating. A lens was used for focusing the light into an optical fiber, which was hooked to the resonator. The EPR was lock-in detected by modulating the DC field at a frequency of 100 kHz. Hence the resonance observed was the first derivative of the resonant absorption spectrum [42]. The field and *g* factor values were determined from a DPPH standard [42]. All experiments were performed multiple times to ensure the validity of the conclusions.

To obtain the spin counts we used two calculation approaches: Matlab, when double integrating the derivative EPR data, and Origin and Matlab, when using the integrated EPR to perform Lorentzian fittings, which provided the *g* factors. While the absolute values of the spin counts obtained by these approaches vary by ~10-50% (with an average variation of ~25%) they are in semi-quantitative agreement. More specifically, the dark EPR spin counts were comparable when double integrating the derivative EPR data or using the integrated EPR with the Lorentzian fittings. This was not the situation for the light induced EPR with the narrow Lorentzian lines. We attribute the discrepancies to potential small deviations from Lorentzian lineshapes and to the sensitivity of the integrals to the baseline. The spin counts reported are therefore from the double integration of the derivative, unless otherwise specified.

The EPR measurements were generally performed multiple times. Specifically, the dark EPR and LEPR of the 0- and 24 h-light-soaked blends were measured 3 times; those of the 8- and 16 h-soaked samples were measured twice. The dark EPR of the $PC_{70}BM$ - and PBDTTT-EFT-only films, pristine and light-soaked, was measured 4 times.

5.3. Results and discussion

5.3.1. CW EPR measurements

Fig. 1 shows the molecular structure of PBDTTT-EFT and $PC_{70}BM$.

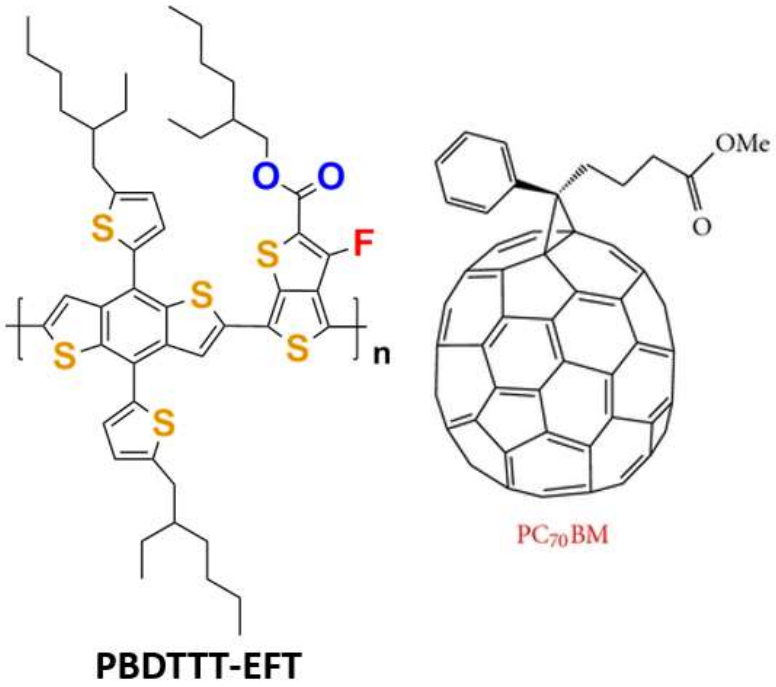

Fig. 1. *Molecular structure of PBDTTT-EFT and $PC_{70}BM$.*

EPR has been used for microscopic characterization of polymer:fullerene BHJ films and solar cells [43-47] including for studying charge accumulation sites in polymer [43] and small molecule [44] solar cells. The advantage of this method is the ability to directly observe spin 1/2 charge carriers and other spin active sites. Since in our EPR measurements the modulation frequency of the external magnetic field was 100 kHz, only carriers with lifetimes comparable to or longer than 10 μs were observable [42].

In a magnetic field B_0, the energy splitting ΔE between the parallel +1/2 and antiparallel -1/2 spin states is given by [48]

$$\Delta E = g\mu_B B_0 \tag{2}$$

where $\mu_B = e\hbar/(2m_e) = 9.27401\times10^{-24}$ J/T = 5.78838×10^{-5} eV/T is the Bohr magneton and g is a factor that depends on the spin's environment [48]; for free electrons $g = 2.0023$. From D-band (130 GHz) EPR the g-tensor components of the LUMO electrons in $PC_{70}BM$ were reported to be

2.0060, 2.0028 and 2.0021 for g_x, g_y and g_z, respectively [45,47], and for the HOMO holes in P3HT they are 2.0038, 2.0023, 2.0011 [45,47]. The *g*-factor for $PC_{60}BM$ obtained from X-band EPR was reported to be 1.9995 [46], i.e., significantly lower than that of $PC_{70}BM$ [45].

5.3.2. Dark CW EPR of Polymer-only and Fullerene-only Films.

Figs. 2(a) and 2(b) show the room temperature dark EPR of neat PBDTTT-EFT and $PC_{70}BM$ films, respectively, before and after 24 h of photodegradation, i.e., light soaking by exposure to 100 mW/cm^2 of light from a solar simulator in a nitrogen atmosphere, with no exposure to ambient air. As seen, there is an overlap in the dark EPR of the polymer- and fullerene-only films (see also Tables 2 and 3). However, the lineshapes are different, indicating that distinct spin-active defects are generated in both.

Figs. 2(c) – 2(f) show the simulations of the dark EPR absorption spectra (i.e., integrals of the spectra shown in Figs. 2(a) and 2(b), which are the derivatives of the absorption spectra) of the polymer- and fullerene-only films by the sum of two Lorentzians [48]. We note that the experiments were conducted so that the amplitudes shown in the figures can be compared. Tables 1 and 2 summarize the *g* values, full width at half maximum (FWHM), amplitudes, and spin densities of these Lorentzians for the polymer- and fullerene-only films, respectively. We note the following:

(a) Spin counts based on Lorentzian fits are subject to significant errors (see below), as the area under a Lorentzian diverges as the limits of integration are extended to [-∞,+∞] [42]. They are also obviously very sensitive to the choice of background or offset level. Thus, spin counts from Lorentzian simulations are less reliable than those obtained by double integration of the derivative spectra, as only truncated Lorentzians are integrable [42].

(b) The EPR intensity also depends on the spin-lattice relaxation time T_1 of the spins [42]. Hence, deducing relative spin counts by comparing the same EPR before and after degradation assumes that T_1 has not changed significantly during degradation. In particular, deducing absolute spin counts by comparing to reference samples such as DPPH assumes that T_1 in both is comparable.

(c) Light-soaking does not generate any new type of spin-active defect, neither in the polymer-only nor the fullerene-only films.

(d) Finally, most importantly*, the hallmark EPR of C dangling bonds at g = 2.0029 ± 0.0002 [30-34] is clearly missing from both the polymer- and fullerene-only films*.

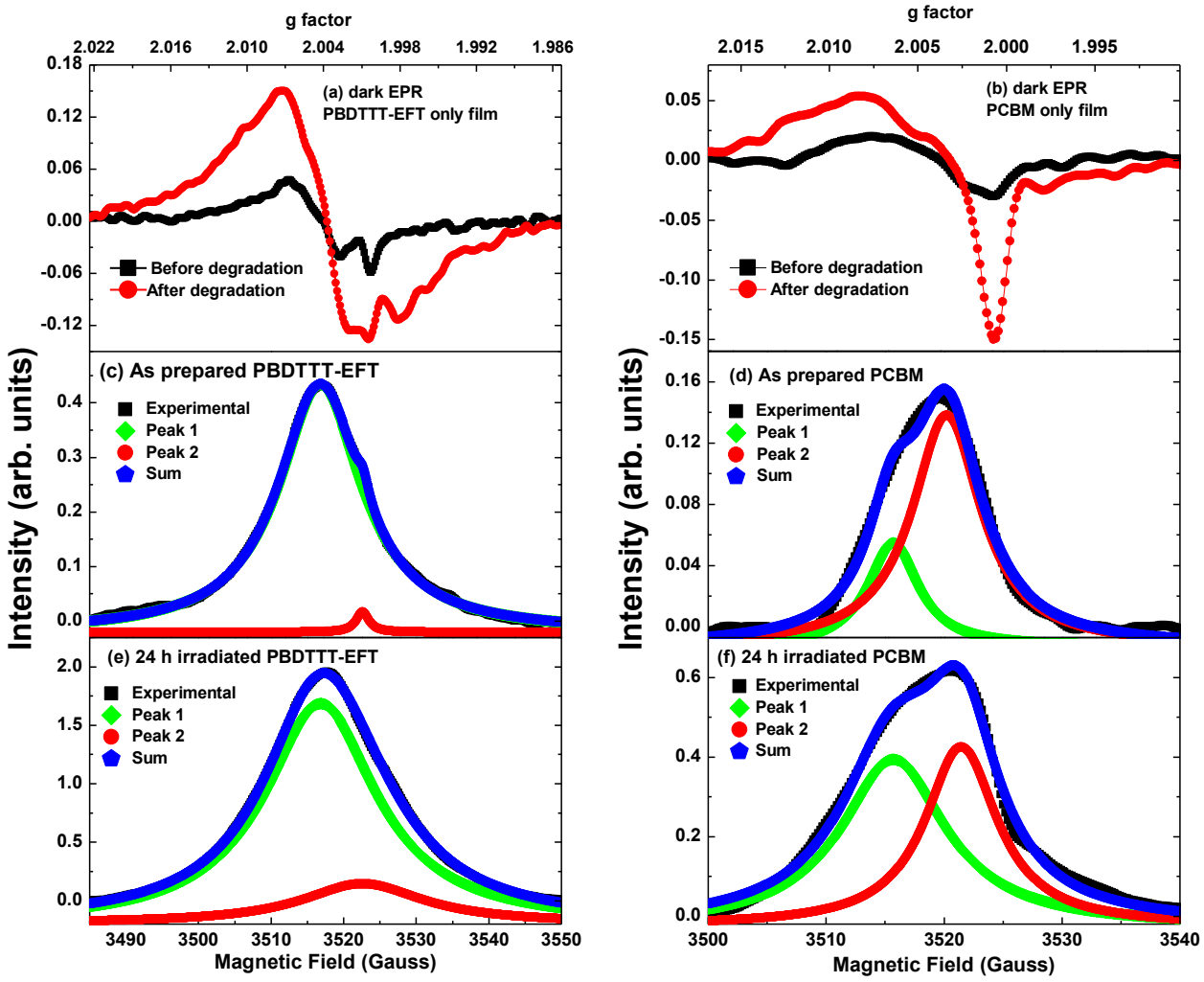

Fig. 2. (*a) and (b): The dark EPR of PBDTTT-EFT and PCBM films, respectively, before and following 24 h irradiation. (c) –(f): Lorentzian best fits of the dark EPR for as prepared and 24 h photodegraded PBDTTT-EFT- (c & e) and $PC_{70}BM$- only films (d & f)*

As seen from Figs. 2(c) and 2(e), and Table 1, following irradiation, the resonance lines of the polymer-only films strengthened significantly, with an overall increased spin count of ~ 5.5 fold and ~88 fold for lines 1 and 2, respectively. From double integration of the EPR spectra, the total spin density of polymer-only films increases ~6 fold from 4.4×10^{18} to 2.6×10^{19} spins/cm^3.

We note that the increase in the near mid gap defect states (at an energy of 0.87 eV) observed in the sub QE measurements of BHJ SCs was also 6 fold.

Table 1. *Lorentzian fits and total spin densities of the dark EPR for as-prepared and irradiated polymer, fullerene, and polymer:fullerene films.*

Photo-degradation period (h)	Lorentzian line #	*g* factor	FWHM (Gauss)	Amplitude	Spin density (cm^{-3})	Total spin density from double integration/ cm^3 (2 weeks in the dark after degradation)
Polymer						
0	1	2.0041	14.0	0.45	3.3×10^{18}	4.4×10^{18}
0	2	2.0007	2.1	0.04	4.1×10^{16}	
24	1	2.0041	18.7	1.88	1.8×10^{19}	2.6×10^{19}
24	2	2.0007	20.5	0.34	3.6×10^{18}	
Fullerene						
0	1	2.0047	5.18	0.07	3.0×10^{17}	1.1×10^{18}
0	2	2.0021	7.1	0.15	9.3×10^{17}	
24	1	2.0047	10.8	0.42	3.9×10^{18}	6.5×10^{18}
24	2	2.0014	7.5	0.45	2.9×10^{18}	
Polymer: Fullerene						
0	1	2.0042	5.67	0.094	2.15×10^{18}	4.47×10^{18} (4.53×10^{18})
0	2	2.0018	5.04	0.132	2.08×10^{18}	
0	3	1.9999	3.72	0.033	1.94×10^{17}	
8	1	2.0054	13.15	0.416	1.51×10^{19}	2.74×10^{19}
8	2	2.0024	7.59	0.43	9.04×10^{18}	
8	3	1.9985	4.61	0.053	6.73×10^{17}	
16	1	2.0062	15.37	0.795	3.38×10^{19}	4.92×10^{19} (9.34×10^{18})
16	2	**2.0027**	8.79	1.088	2.65×10^{19}	
16	3	1.9985	6.87	0.186	3.54×10^{18}	
24	1	2.0065	19.6	0.931	5.04×10^{19}	6.07×10^{19} (9.64×10^{18})
24	2	**2.0027**	9.22	1.11	2.82×10^{19}	
24	3	1.9985	5.37	0.226	3.36×10^{18}	

As seen from Figs. 2(d) and 2(f), and Table 1, following irradiation, the dark EPR of the fullerene-only films also strengthened significantly, with an overall ~6- and ~4.1-fold increase in the spin count of lines 1 and 2, respectively. From the double integration of the EPR spectra, the total spin density of fullerene-only films increased from 1.1×10^{18} to 6.5×10^{18} spins/cm^3, a ~6 fold increase.

5.3.3. Dark CW EPR of the Polymer:Fullerene Blend Films.

Fig. 3(a) shows the dark room-temperature CW EPR of PBDTTT-EFT:$PC_{70}BM$ blend films before and following 8, 16, and 24 h of light soaking; Fig. 3(b) shows the respective spin densities. Figs. 3(c)-(f) show the simulations of the blends' dark EPR spectra by a sum of three Lorentzians, and Table 4 summarizes the *g* values, linewidths, amplitudes, and spin counts of these Lorentzians. As Fig. 3 and Table 1 show clearly, the line at $g = 2.0027$ rises rapidly during light-soaking. Indeed, in the pristine film (0 h of light-soaking) $g = 2.0017$, which is significantly lower than 2.0027, and even after light soaking for 8 h, $g = 2.0024$. We suspect that the spins responsible for the line at 2.0017 are significantly different from carbon dangling bonds, although they may be related to them.

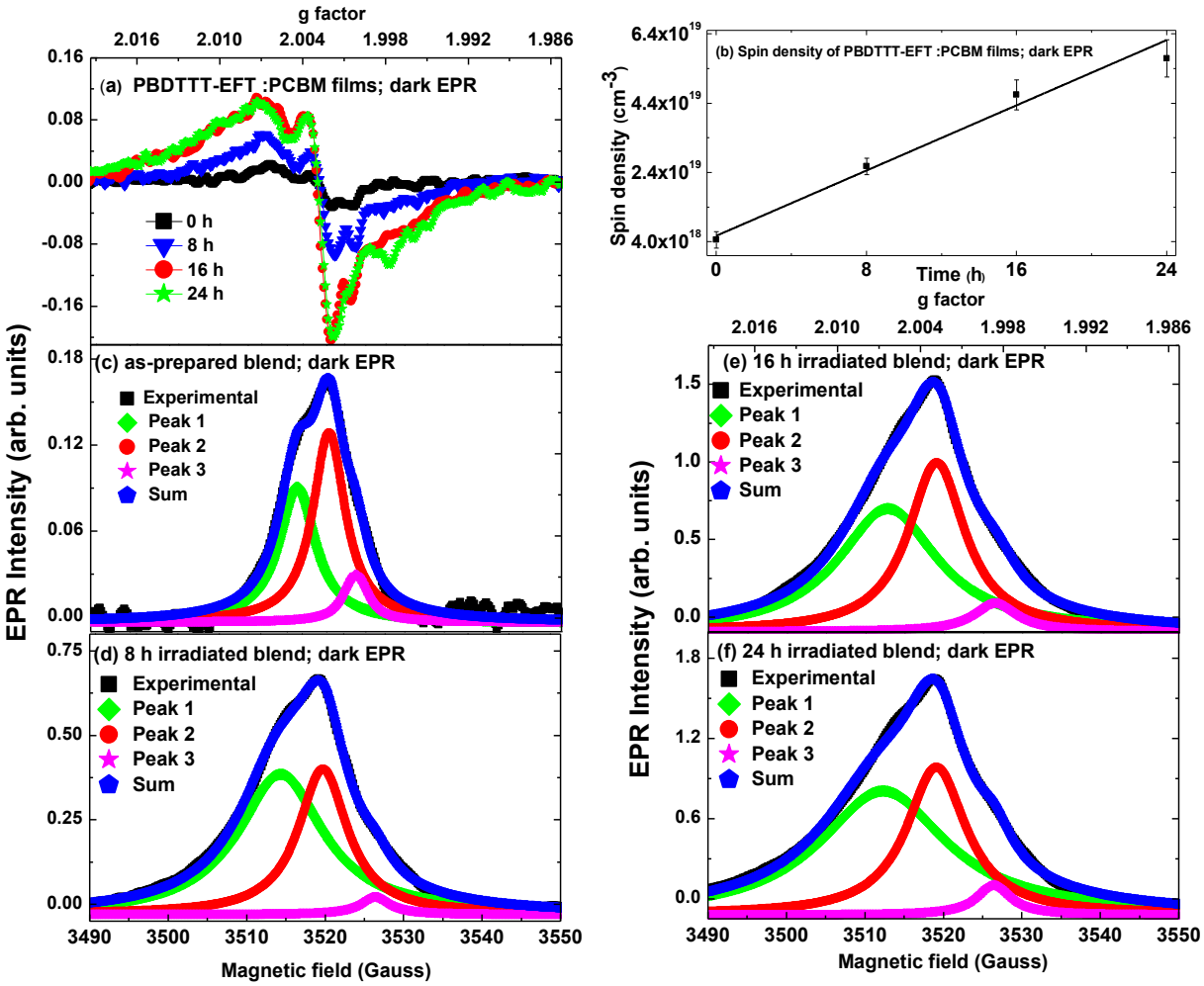

Fig. 3. *(a) The dark CW-EPR of PBDTTT-EFT:PCBM films after light soaking for various periods at 290K and (b) the respective spin counts. (c) –(e) Lorentzian best fits of the dark EPR following 0, 8, 16, and 24 h of light soaking of PBDTTT-EFT:PC$_{70}$BM blend films.*

After light soaking for 8 h, the total increase in the spin count was 6.1 fold, and their nature becomes very similar to a carbon dangling bond, and after light soaking for 16 h they are, from the X-band EPR standpoint, indistinguishable from such dangling bonds.

It is important to note that the location of the C dangling bonds is not yet fully established and may depend on the particular polymer. Theoretical and computational studies on other polymer: fullerene systems [24,36] suggest that they are located at the first carbon atom of the

alkyl group that is bonded to the polymer backbone (the α carbon). A recent study on PTB7:PCBM [37] suggest that it is the first carbon of the alkyl group that is bonded to a bridging O atom. However, this latter case is not relevant to the PBDTTT-ETF system as evident from the polymer structure (Fig. 1). The C dangling bonds are likely the traps near the D/A interface observed in the DOS measurements. We note that the DOS measurements indicated a 13 fold increase in the defect state density at the D/A interface; the increase in the spin count from the dark EPR of peak 2 was ×13.5 with the overall ×18.5(from the sum of the Lorentzians) increased spin count for 24 h irradiated blend film. We note that this increase is essentially identical to that of the total spin density obtained from double integrals of the EPR (Table 4), which is ×13.6.

Note that Line 1 evolves significantly during irradiation, with *g* changing from 2.0042 to 2.0065. Importantly, though, the origin of this peak, whose spin count increased ~23-fold following 24 h photodegradation, to 5.0×10^{19}, is currently unknown. The irradiation effect on Line 3 (g~1.999) is much smaller, as that *g* only evolves from 1.9999 to 1.9985.

It is interesting to note that the C dangling bond EPR weakens with time when the blend is kept in the dark. As Fig. 4 and Table 1 show, *the EPR of the as-prepared film did not change, while the EPR of the 16- and 24-h light-soaked films weakened 5.3- and 6.3-fold, to* 9.34×10^{18} *and* 9.64×10^{18} */cm^3 respectively, after 2 weeks based on the double integral data.*

The change in the defects responsible for the Lorentzian at $g \sim 1.999$ is much smaller, as that *g* value only evolves from 1.9999 to 1.9985. We also do not rule out the formation of new spin active defects below the 10^{11} spins/Gauss limit of detection (LOD) of our X band EPR**.** Hence, higher frequency EPR is highly desirable to enhance the LOD and provide more detailed information on the *g* tensors that will enable evaluation of models of the nature of the spin-active defects. Moreover, trace oxygen related spin-active defects are not ruled out.

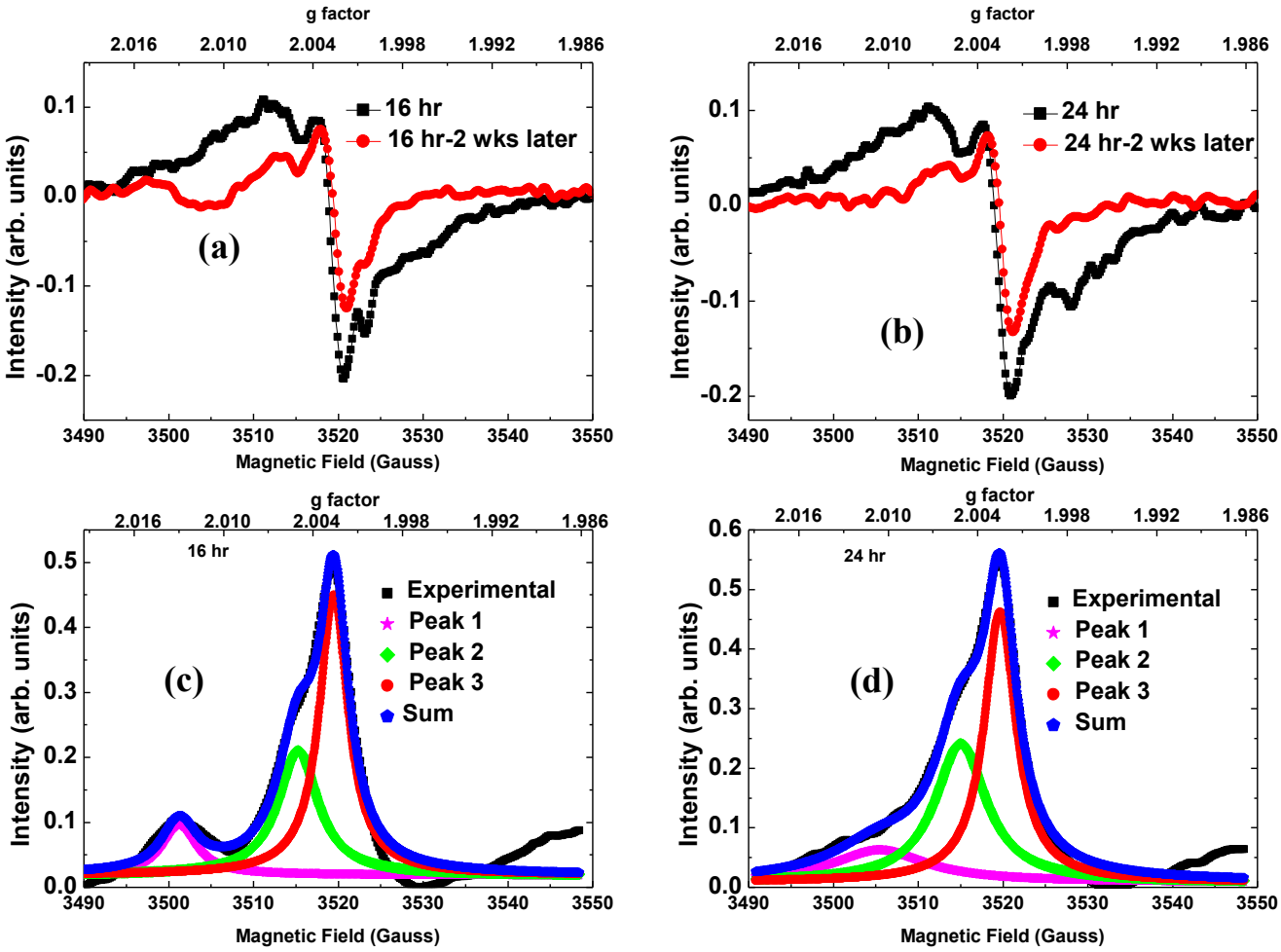

Fig. 4. *The dark EPR of the (a) 16- and (b) 24-hour light-soaked films immediately after light soaking (black lines) and after 2 weeks in the dark (red lines). (c) and (d) The Lorentzian simulations of these EPRs.*

Table 2. *The intensities of the Lorentzian components of the dark EPR of the 16- and 24-h light-soaked blend films after 2 week storage in the dark.*

Photo-degradation period (h)	Lorentzian Line #	*g* factor	FWHM (Gauss)	Amplitude	Spin density after 2 weeks
16	1	2.0129	4.99	0.078	1.06×10^{18}
16	2	2.0049	5.74	0.19	3.06×10^{18}
16	3	2.0025	4.13	0.43	4.87×10^{18}
24	1	2.0105	13.5	0.054	1.99×10^{18}
24	2	2.0050	7.33	0.23	4.87×10^{18}
24	3	2.0025	4.54	0.45	7.97×10^{18}

5.3.4. CW Light-Induced EPR of Polymer:Fullerene Blend Films.

Fig. 5(a) shows the light induced EPR (LEPR, i.e., the difference between the EPR spectrum measured under illumination and the dark EPR) of the pristine and light-soaked PBDTTT-EFT:$PC_{70}BM$ blend films. We note that the LEPR of the polymer- and fullerene-only films was unobservable at room temperature. This behavior is clearly due to the very low level (~2%) of SE dissociation [49] in such films, in sharp contrast to the massive dissociation of such SEs in the polymer:fullerene blends.

As seen in Fig. 5(a), the amplitude of the LEPR of the blend generally increases with light soaking, however, as shown in Fig. 5(b), the LEPR spin counts decrease due to the general narrowing of the EPR lines. The reference film was not subjected to light degradation, except when the EPR was measured under illumination for 8 min.

Figs. 5(c) – 5(f) show the Lorentzian best fits for the LEPR following 0, 8, 16, and 24 h of light soaking for PBDTTT-EFT:$PC_{70}BM$ blend films. Table 3 summarizes the fitting results. The LEPR displays the holes generated by illumination on the polymer ($g \sim 2.0071$) and the electrons on the $PC_{70}BM$ ($g \sim 2.0028$).

The observed decrease of the LEPR intensity I_{LEPR} with light soaking is likely due to a decreasing steady-state photocarrier density n_c. This is probably due to an increasing density of light-generated carrier traps n_{tr}: These traps are recombination centers, whose increased density decreases the PCE of the solar cells. Since $I_{LEPR} \propto n_c = G_c\tau_c$, where G_c and τ_c are the carrier generation rate and lifetime, respectively, as n_{tr} increases, τ_c decreases.

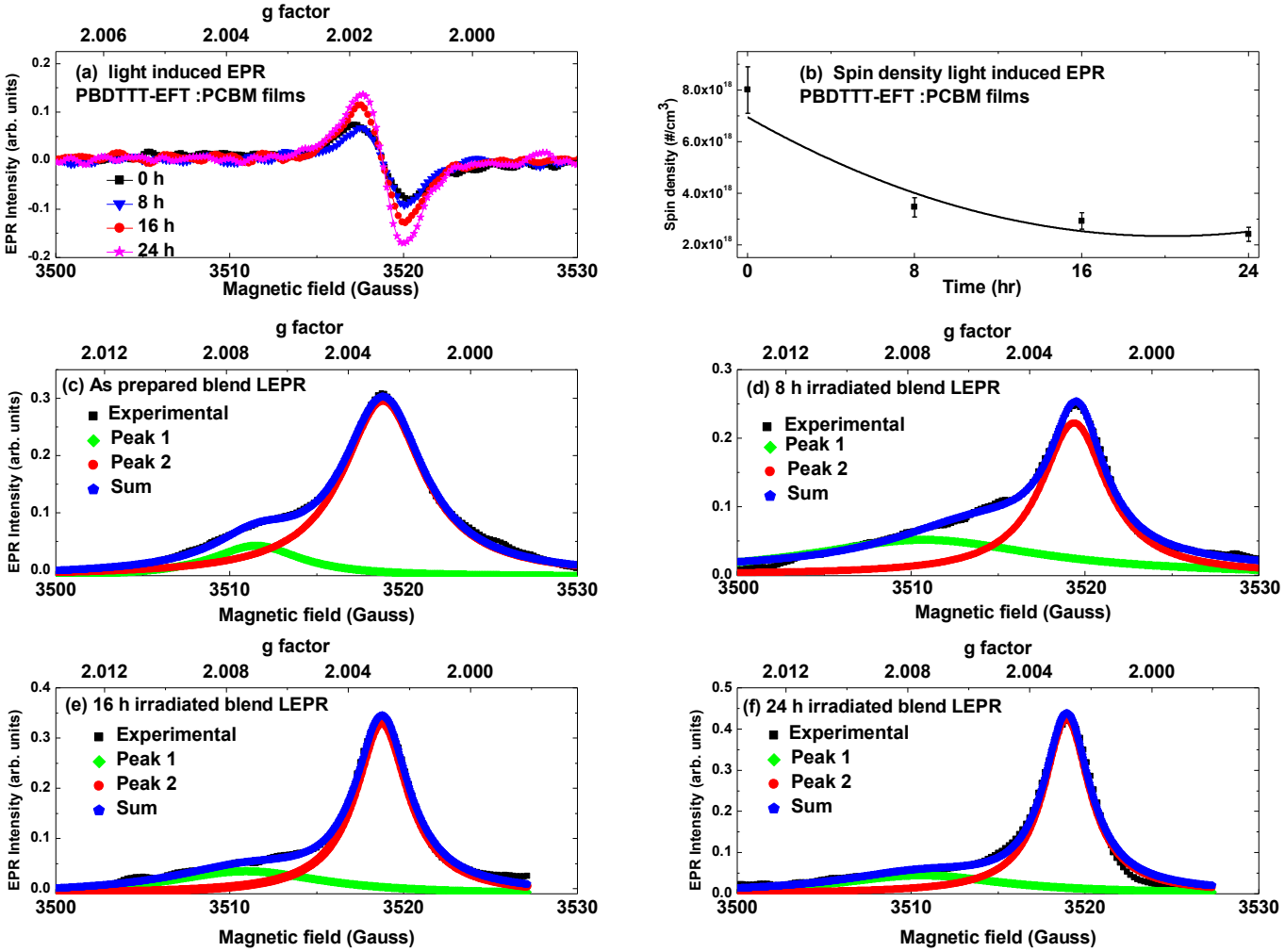

Fig. 5. *(a) The LEPR of PBDTTT-EFT:PCBM films after light soaking for various periods at 290K and (b) the respective spincounts. (c)-(f): Lorentzian best fits of the LEPR following 0, 8, 16, and 24 h of light soaking for PBDTTT-EFT:$PC_{70}BM$ blend films.*

Table 3. *Lorentzian fitting results of the LEPR for the as prepared and photodegraded polymer:fullerene blend films and the total spincount from double integrals.*

Photo-degradation period (h)	Lorentzian Number	*g* factor	FWHM (Gauss)	Amplitude	Spin density /cm^3	Total spin density from double integration/cm^3
0	1	2.0070	6.28	0.054	9.39×10^{17}	8.02×10^{18}
0	2	2.0028	5.64	0.306	4.78×10^{18}	
8	1	2.0075	16.37	0.052	2.34×10^{18}	3.46×10^{18}
8	2	2.0025	4.60	0.222	2.82×10^{18}	
16	1	2.0073	10.97	0.047	1.42×10^{18}	2.93×10^{18}
16	2	2.0029	3.72	0.342	3.51×10^{18}	
24	1	2.0075	11.81	0.045	1.48×10^{18}	2.41×10^{18}
24	2	2.0028	3.21	0.424	3.76×10^{18}	

5.3.5. Effect of UV and blue light.

Electronic measurements showed increased stability when filters were used. The transmittance range of the filters is shown in Fig. 6 below.

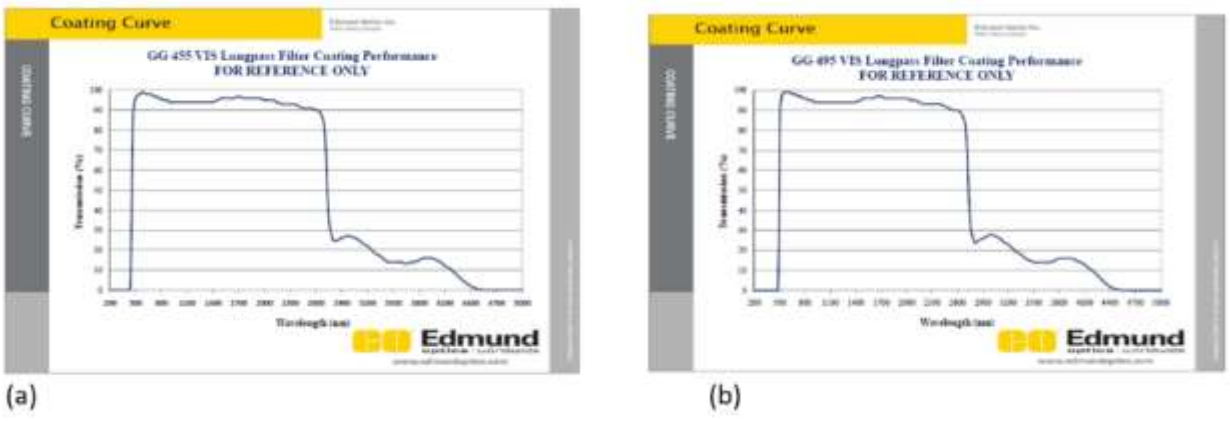

Fig. 6. *The transmittance for (a) 455nm filter and (b) 495 nm filter.*

Fig. 7 shows the dark EPR of PBDTTT-EFT:PCBM films after 24 hours of photodegradation with a 455 nm and 495 nm filter.

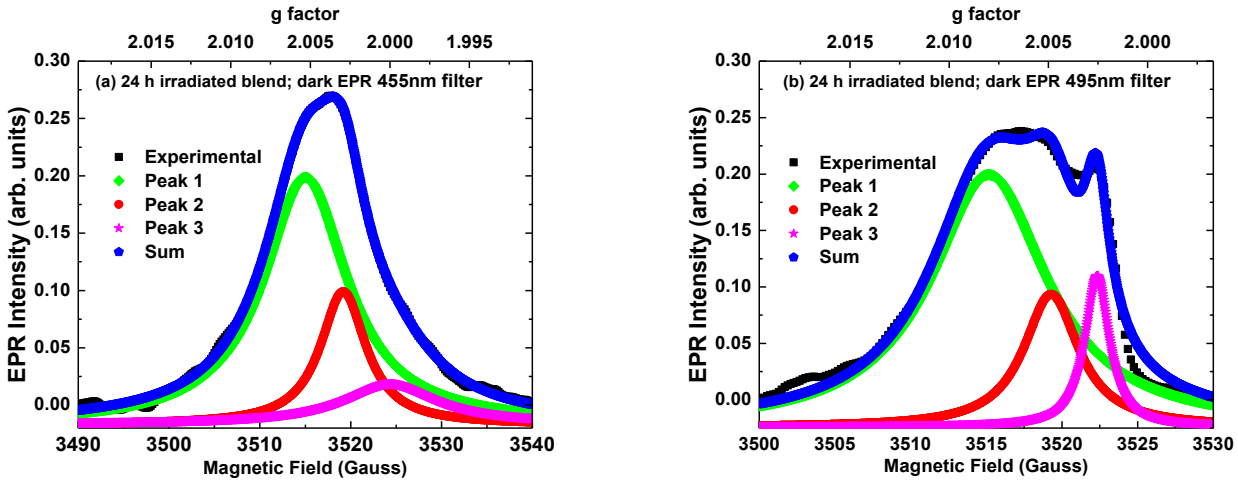

Fig. 7 *The dark CW-EPR of PBDTTT-EFT:PCBM films after light soaking for 24hr at 290K with (a)455 nm and (b) 495 nm filter.*

Photo-degradation period (h)	Lorentzian Number	*g* factor	FWHM (Gauss)	Amplitude	Spin density /cm^3
24 hr 455 nm filter	1	2.0050	11.2	0.216	5.8×10^{18}
24 hr 455 nm filter	2	2.0027	6.11	0.116	1.7×10^{18}
24 hr 455 nm filter	3	1.9997	12.8	0.035	1.1×10^{18}
24 hr 495 nm filter	1	2.0051	9.27	0.224	5.0×10^{18}
24 hr 495 nm filter	2	2.0028	4.43	0.118	1.3×10^{18}
24 hr 495 nm filter	3	2.0010	1.99	0.134	6.5×10^{17}

Table 4. *Lorentzian fitting results of the dark EPR for 24 h irradiated blend films with a 455 nm and 495 nm filter.*

Without the filters, the carbon dangling bond intensity after 24 hours was 2.82×10^{19} spins/cm^3. Consistent with the electronic measurements, the dark EPR showed that the DB spin density

decreased ~16.6 -fold with the 455 nm filters, and even slightly more (~21.7 –fold) with the 495 nm filter as shown in table 4. Overall, filtering out light below 455 nm significantly reduces the short-term instability of the PSCs.

5.3.6. C DB generation mechanism.

It is well-known that breaking an isolated C-H bond requires >4.0 eV [24,35]. Yet this study indicates that even 495-455 nm photons, with energy 2.51-2.73 eV, have a finite probability of breaking such bonds. We therefore consider two mechanisms for such bond-breaking: (i) Exciton annihilation by polarons, which absorb the exciton energy to become highly energized hot polarons with energy sufficient to break the C-H bond. This mechanism was invoked to account for the severe degradation of blue OLEDs [41]. As the energy of an electron in the $PC_{70}BM$ LUMO is ~1.3 eV above the PBDTTT-EFT HOMO, that electron would need to annihilate the 2.5-2.73 eV SE before that exciton dissociates by electron transfer to $PC_{70}BM$. Yet this dissociation is extremely fast (<1 ps) [50]. Hence we rule out this mechanism. (ii) Direct photon absorption by a LUMO electron in $PC_{70}BM$ (or a HOMO hole in PBDTTT-EFT), i.e., a photoinduced absorption process by polarons in the polymer:fullerene blend. Polaron bands in photoinduced absorption spectra are well documented [51], and such a process would create a hot polaron with energy >1.3 + 2.51 = 3.81 eV, i.e., sufficiently close to the 4.0 eV threshold for a finite probability to break a C-H bond, and more than sufficient for C-H bonds within an organic molecule or polymer [24,35,36].

5.4. Conclusions

Via dark EPR and broad electronic measurements we present strong evidence for largely blue/UV (<495 nm) photogeneration of metastable C DBs (g=2.0029±0.0004) in PBDTTT-EFT: $PC_{70}BM$ blends, most likely at the D/A interface, which strongly contribute to degradation of

BHJ PSCs without their exposure to the ambient. This observation is consistent with theoretical studies that suggest light-induced degradation of such cells due to C-H bond straining/rearrangement/breaking. Since C-H bond breaking requires >4 eV, processes other than blue/UV light absorption by the polymer are required for DB formation. Hot polarons generated by photon absorption at <495 nm by the fullerene LUMO or polymer HOMO polarons present a significant probability of breaking such bonds. The electronic and EPR measurements provided, respectively, the density of trapping states throughout the gap and spin counts of defects and generated charges. While the spin count in dark EPR increased with irradiation, the LEPR spin density decreased due to the increased trap sites that act as recombination centers, leading to shorter polaron lifetimes and consequently lower steady-state densities under illumination.

In agreement with the dark EPR results, DOS measurements showed a significant increase in midgap states at the D/A interface which resulted in increased charge trapping and recombination, reduced carrier collection efficiency at the electrodes, and hence decreased J_{sc}, V_{oc}, FF, hole mobility, and PCE of PSCs. An increase in deep defect states observed in subgap QE measurements was consistent with an increase in spin-active defects in the polymer-only films observed in the dark EPR, which indicated also such an increase in fullerene-only films. We note that the 13-fold increase in the D/A DOS is very similar to the increase in the C DB spin density (13.5-fold) following 24 h of irradiation. Similarly, the 6-fold increase in the sub QE defect states in the polymer is similar to the related increased spin density. Using optical filters to cut the UV and blue light <495 nm greatly improves the short-term stability of the solar cells and reduces the DB spin density. Importantly, a decrease in the DB density was observed by keeping the degraded films in N_2 in the dark. Minor structural rearrangements and oxygen

impurities that generate defect states, though at a level that is insufficient to affect the measured absorption and morphology, cannot be ruled out.

References

[1] Z. Shaoqing, Y. Long, Z. Wenchao, L. Delong, Y. Huifeng, H. Jianhui, Macromolecules 47 (2014) 4653.

[2] H.-Y. Chen, J. Hou, S. Zhang, Y. Liang, G. Yang, Y. Yang, L. Yu, Y. Wu, G. Li, Nat. Photon. 3 (2009) 649.

[3] X. Fan, G. Fang, F. Cheng, P. Qin, H. Huang Y. Li, J. Phys. D: Appl. Phys. 46 (2013) 305106.

[4] D. Wang, F. Zhang, L. Li, J. Yu, J. Wang, Q. An, W. Tang, RSC Adv. 4 (2014) 48724.

[5] T. Y. Chu, J. Lu, S. Beaupré, Y. Zhang, J. R. Pouliot, S. Wakim, J. Zhou, M. Leclerc, Z. Li, J. Ding, Y. Tao, J. Am. Chem. Soc. 133 (2011) 4250.

[6] L. Dou, J. You, J. Yang, C. C. Chen, Y. He, S. Murase, T. Moriarty, K. Emery, G. Li, Y. Yang, Nat. Photon. 6 (2012) 180.

[7] J. Peet, J. Y. Kim, N. E. Coates, W. L. Ma, D. Moses, A. J. Heeger, G. C. Bazan, Nat. Mater. 6 (2007) 497.

[8] Y. Liang, Z. Xu, J. Xia, S. T. Tsai, Y. Wu, G. Li, C. Ray, L. Yu, Adv. Mater. 22 (2010) E135.

[9] Z. He, C. Zhong, S. Su, M. Xu, H. Wu, Y. Cao, Nat. Photon. 6 (2012) 591.

[10] Z. He, C. Zhong, X. Huang, W. Y. Wong, H. Wu, L. Chen, S. Su, Y. Cao, Adv. Mater. 23 (2011) 4636.

[11] G. Li, V. Shrotriya, Y. Yao, Y. Yang, J. Appl. Phys. 98 (2005) 043704.

[12] G. Li, V. Shrotriya, J. Huang, Y. Yao, T. Moriarty, K. Emery, Y. Yang, Nat. Mater. 4 (2005) 864.

[13] F. Zhang, K. G. Jespersen, C. Bjorstrom, M. Svensson, M. R. Andersson, V. Sundstrom, K. Magnusson, E. Moons, A. Yartsev, O. Inganas, Adv. Funct. Mater. 16 (2006) 667.

[14] K. Kawashima, Y. Tamai, H. Ohkita, I. Osaka, K. Takimiya, Nat. Comm. 6 (2015) 10085.

[15] Y. Liu, J. Zhao, Z. Li, C. Mu, W. Ma, H. Hu, K. Jiang, H. Lin, H. Ade, H. Yan, Nat. Comm. 5 (2014) 5293.

[16] S.-H. Liao, H.-J. Jhuo, P.-N. Yeh, Y.-S. Cheng, Y.-L. Li, Y.-H. Lee, S. Sharma, S.-A. Chen, Scientific Reports 4 (2014) 6813.

[17] F. C. Krebs, K. Norrman, Prog. Photovolt: Res. Appl. 15 (2007) 697.

[18] A. Rivaton, S. Chambon, M. Manceau, J.-L. Gardette, N. Lemaitre, S. Guillerez, Polym. Degrad. Stab. 95 (2010) 278.

[19] M. O. Reese, A. J. Morfa, M. S. White, N. Kopidakis, S. E. Shaheen, G. Rumbles, D. S. Ginley, Sol. Energy Mater. Sol. Cells 92 (2008) 746.

[20] K. Kawano, R. Pacios, D. Poplavskyy, J. Nelson, D. D. C. Bradley, J. R. Durrant, Sol. Energy Mater. Sol. Cells. 90 (2006) 3520.

[21] M. Jørgensen, K. Norrman, F. C. Krebs, Sol. Energy Mater. Sol. Cells 92 (2008) 686.

[22] K. Kawano, C. Adachi, Appl. Phys. Lett. 96 (2010) 053307.

[23] J. Bhattacharya, R. W. Mayer, M. Samiee, V. L. Dalal, Appl. Phys. Lett. 100 (2012) 193501.

[24] R. A. Street, D. M. Davies, Appl. Phys. Lett. 102 (2013) 043305.

[25] T. Endale, E. Sovernigo, A. Radivo, S. D. Zilio, A. Pozzato, T. Yohannes, L. Vaccari, M. Tormen, Sol. Energy Mater. Sol. Cells 123 (2014) 150.

[26] D. Mori, H. Benten, I. Okada, H. Ohkita, S. Ito, Energy Environ. Sci. 7 (2014) 2939.

[27] P. Adhikary, S. Venkatesan, N. Adhikari, P. P. Maharjan, O. Adebanjo, J. Chenb, Q. Qiao, Nanoscale 5 (2013) 10007.

[28] E-P. Yao, Y-J. Tsai, W-C. Hsu, Int. J. Photoenergy 2014 (2014) 952528.

[29] R. A. Street, Hydrogenated Amorphous Silicon. (Cambridge Univ. Press, Cambridge, 1991).

[30] A. Abragam, Principles of Nuclear Magnetism (Clarendon Press, Oxford, UK 1985).

[31] A. Manivannan, M. Chirila, N.C. Giles, M.S. Seehra, Carbon 37 (1999) 1741.

[32] J. L. Cantin, H. J. von Bardeleben, Y. Shishkin, Y. Ke, R. P. Devaty, W. J. Choyke, Phys. Rev. Lett. 92 (2004) 015502.

[33] A. I. Shames, A. M. Panich, S. Porro, M. Rovere, S. Musso, A. Tagliaferro, M. V. Baidakova, V. Y. Osipov, A. Y. Vul, T. Enoki, M. Takahashi, E. Osawa, O. A. Williams, P. Bruno, D. M. Gruen, Diamond & Related Materials 16 (2007) 1806.

[34] A. I. Shames, A. M. Panich, E. Mogilko, J. Grinblat, E. W. Prilutskiy, E. A. Katz, Diamond & Related Materials 16 (2007) 2039.

[35] R. A. Street, J. E. Northrup, B. S. Krusor, Phys. Rev. B 85 (2012) 205211.

[36] J. E. Northrup, Appl. Phys. Express 6 (2013) 121601.

[37] S. Shah, R. Biswas, J. Phys. Chem. C 119 (2015) 20265.

[38] M. Segal, M. A. Baldo, M. K. Lee, J. Shinar, Z. G. Soos, Phys. Rev. B 71 (2005) 245201.

[39] J. Shinar, Laser Photonics Rev. (invited review) 6 (2012) 767.

[40] Y. Chen, M. Cai, E. Hellerich, R. Shinar, J. Shinar, Phys. Rev. B 92 (2015) 115203.

[41] Y. Zhang, J. Lee, S. R. Forrest, Nat. Comm. 5 (2014) 5008.

[42] C. P. Jr. Poole, Electron Spin Resonance: A Comprehensive Treatise on Experimental Techniques, (John Wiley & Sons Inc., New York, 1983).

[43] T. Nagamori, K. Marumoto, Adv. Mater. 25 (2013) 2362.

[44] K. Marumoto, T. Fujimori, M. Ito, T. Mori, Adv. Energy Mater. 2 (2012) 591.

[45] O. G. Poluektov, S. Filippone, N. Martín, A. Sperlich, C. Deibel, V. Dyakonov, J. Phys. Chem. B 114 (2010) 14426.

[46] T. J. Savenije, A. Sperlich, H. Kraus, O. Poluektov, M. Heeney, V. Dyakonov, Phys. Chem. Chem. Phys. 13 (2011) 16579.

[47] J. Niklas, K. L. Mardis, B. P. Banks, G. M. Grooms, A. Sperlich, V. Dyakonov, S. Beaupré, M. Leclerc, T. Xu, L. Yu, O. G. Poluektov, Chem. Chem. Phys. 15 (2013) 9562.

[48] A. J. Weil, J. R. Bolton, J. E. Wertz, Electron Paramagnetic Resonance: Elementary Theory and Practical Applications (Wiley-Interscience, New York, 1994).

[49] J. Partee, E. L. Frankevich, B. Uhlhorn, J. Shinar, Y. Ding, T. J. Barton, Phys. Rev. Lett. 82 (1999) 3673.

[50] C. J. Brabec, G. Zerza, G. Cerullo, S. D. Silvestri, S. Luzzati, J. C. Hummelen, S. Sariciftci, Chem. Phys. Lett. 340 (2001) 232.

[51] R. Tautz, E. D. Como, T. Limmer, J. Feldmann, H.-J. Egelhaaf, E. Hauff, V. Lemaur, D. Beljonne, S. Yilmaz, I. Dumsch, S. Allard, U. Scherf, Nat. Commun. 3 (2012) 970.

Chapter 6: Summary

Chapter 1 provides an introduction to organic solar cells (OSCs) and discusses their potential as flexible, lightweight and low cost energy sources. Additionally, a brief introduction to degradation processes in OSCs is given. Chapter 2 covers the experimental setup and characterization techniques of the OSCs. Chapters 3 to 5 provide our results and discussion. In chapter 3, it is shown that using Bphen (4,7-di(phenyl)-1,10-phenanthroline) as an electron transport layer in inverted OSCs with cesium salts enhances both the power conversion efficiency (PCE) and stability. Devices with the structure of ITO/CsCl or CsI/Bphen/P3HT:PCBM/MoO_3/Al exhibit superior performance to those without Bphen and to those with Bphen, but without the cesium halide (P3HT is poly 3-hexylthiophene, PCBM is [6,6]-phenyl-C_{60}-butyric acid methyl ester and MoO_3 is Molybdenum(IV) oxide). Addition of a Bphen layer on the Cs halide layer in ITO/CsCl/P3HT:PCBM/MoO_3/Al resulted in a 46% improvement in the PCE, increasing it from 2.5 % to 3.7%. The PCE of unencapsulated cells with the structure ITO/CsCl/BPhen/P3HT:PCBM/MoO_3/Al decreased by less than 2% in over 3 weeks, whereas for cells with the structure ITO/CsCl//P3HT:PCBM/MoO_3/Al, the PCE decreased by over 50% in the same time period. Bphen acts as an exciton and hole blocking layer and enhances the PCE of OSCs by blocking excitons that would be otherwise quenched at the organic/ITO cathode. Blocking holes reduces recombination at the ITO electrode leading to photocurrent enhancement. Moreover, the blocked excitons can dissociate and contribute to photocurrent improving the short circuit current (J_{sc}) and hence the PCE. Also, the cesium from the cesium halide dopes Bphen and enhances its electron transport property. Charge extraction was enhanced in the presence of Bphen. Bphen may also enhance the stability of the OSCs by separating the P3HT:PCBM from the oxygen that was shown to be present in such inverted cells

at the Cs halide layer. Another possibility is reducing degradation induced by the energy released by electron-hole recombination. Adding a polystyrene beads (PSB) layer on the blank light incident side of an OSC substrate enhances the performance of deteriorated cells; for example without a PSB film, solar cells deteriorated by an average of 36.8% in a period of 2 weeks, but addition of the PSB improved its PCE to within 10% of the original value. This enhancement is due to an increase in light absorption, which resulted in an enhancement in J_{sc} and PCE. This behavior was attributed to light direction and scattering by the beads that enhance the absorption in the active OSC layer.

Chapters 4 and 5 explore degradation processes in poly[4,8-bis(5-(2-ethylhexyl)thiophen-2-yl)benzo[1,2-b;4,5-b']dithiophene-2,6-diyl-alt-(4-(2-ethylhexyl)-3-fluorothieno[3,4-b]thiophene-)-2-carboxylate-2-6-diyl)] (PBDTTT-EFT) films and SCs. PBDTTT-EFT is a low band gap, highly efficient polymer with PCEs up to 9% for OSCs with a standard structure and 10% for OSCs with an inverted structure. However, it has been shown that PBDTTT-EFT-based OSCs degrade under heat and in chapters 4 and 5, an investigation of the cells short-term photodegradation (with up to 24 hours of light irradiation) is reported. Results of electronic measurements are discussed in chapter 4. It is shown that a change in the fundamental properties of the PSCs occurs upon irradiation. There was a 77% decrease in the PCE from 8.7% to 2%; J_{sc} decreased by 55% of the initial value, V_{oc} by 23%, and FF by 35% following 24 h of light exposure. EQE measurements showed a decrease in charge extraction, which may have been partially due to the observed, via space charge current limited mobility measurements, reduction in hole mobility. Density-of-states (DOS) measurements showed a significant increase in midgap states at the interface between PBDTTT-EFT and PCBM (~0.55–0.65 eV above the polymer's HOMO level). The observed midgap states lead to increased charge trapping and recombination,

reducing carrier collection efficiency at the electrodes, and resulting in a decrease in J_{sc}, FF, hole mobility, and the PCE. Furthermore, an increase in recombination at the D/A interface results in the reduction of the $V_{oc.}$ Subgap QE measurements showed an increase in deep defect states in the polymer (at incident energies in the range of 0.87 to 1.1 eV). The use of UV (< 455 nm) and blue (< 495 nm) filters showed a great improvement in the short-term OSC stability demonstrating that blue and UV light were largely responsible for the observed OSC photodegradation.

Dark continuous wave (CW) electron paramagnetic resonance (EPR) measurements shown in chapter 5 provide for the first time experimental evidence for the formation of metastable C dangling bonds (DBs) (g=2.0029±0.0004) by blue/UV irradiation of polymer:fullerene blend films in nitrogen. The DB density decreased ~ 4 fold after being kept in the dark for two weeks. The dark EPR results indicate that the DBs were at the bulk heterojunction donor-acceptor interface, as they were not present in neat polymer and fullerene films. The spin density of the blend films decreased with light exposure most likely due to a decreasing steady-state photocarrier density caused by an increasing density of light-generated carrier traps, in agreement with electronic measurements. Consistent with the electronic measurements, the dark EPR showed that the DB spin density decreased 16.6 -fold with the 455 nm filter, and even slightly more (~21.7 –fold) with the 495 nm filter. Overall, filtering out light below 455 nm significantly reduces the short-term instability of the PSCs. Most likely, the C DBs were created by direct photon absorption by a lowest unoccupied molecular orbital (LUMO) electron in $PC_{70}BM$ (or a highest occupied molecular orbital (HOMO) hole in PBDTTT-EFT). Such a process would create a hot polaron with energy >1.3 + 2.51 = 3.81 eV that is sufficiently close to the 4.0 eV threshold for a finite probability to break a C-H bond. The

results were consistent with theoretical studies that suggested light-induced degradation of organic solar cells due to C-H bond straining/rearrangement/breaking.

Future work will continue in making new polymers with both a higher efficiency and stability in sunlight and in ambient atmosphere. Furthermore, work is being done to develop new OSC architectures and optical approaches that enhance the efficiency and stability of the existing polymers.

Acknowledgements

I am deeply grateful to my advisors Dr Joseph Shinar and Dr Ruth Shinar for their guidance, encouragement and help throughout my graduate research. Their help and suggestions greatly contributed to my success. I am also thankful to Dr Dalal for his support, encouragement and help.

My gratitude also goes to my colleagues and friends whom I worked and collaborated with. I would like to thank Eeshita Manna, William R Lindeman, Dusan Danilovic, Teng Xiao, Min Cai, Rui Liu, Emily Hellerich, Weipan Cui, Chamika Hippola, Joong-Mok Park and Rajiv Kaudal. I am thankful to Mehran Samiee, Pranav Joshi, Joydeep Bhattacharya and Moneim Ismail for in-depth discussions. Also, for helping me at the microelectronic research center, I thank Max Noack and Dr Wai Leung. I also thank my committee members Dr Rana Biswas, Dr Thomas Koschny and Sanjeevi Sivasankar.

I am thankful to the Department of Physics at Iowa State. **This work was supported by the U.S. Department of Energy (DOE), Department of Materials and Science Engineering at the Ames Laboratory under contract number DE-AC02-07CH11358. The Ames Laboratory is operated for the DOE by Iowa State University. The document number assigned to this thesis/dissertation is IS-T3197.**